DEVELOPMENT OF AN AUTOMATED ROBOTIC EDGE DEBURRING SYSTEM

by

Gary M. Bone, B. Sc. Hons. (App. Sc.), M. Eng.

A Thesis

Submitted to the School of Graduate Studies

in Partial Fulfillment of the Requirements

for the Degree

Doctorate of Philosophy

McMaster University

DEVELOPMENT OF AN AUTOMATED ROBOTIC EDGE DEBURRING SYSTEM

DOCTORATE OF PHILOSOPHY

(Mechanical Engineering)

McMASTER UNIVERSITY

Hamilton, Ontario

TITLE: Development of an Automated Robotic Edge Deburring System

AUTHOR: Gary M. Bone, B. Sc. Hons. (App.Sc.) (Queen's University), M. Eng. (McMaster University)

SUPERVISOR: Dr. M. A. Elbestawi

NUMBER OF PAGES: xvi, 163

ABSTRACT

This thesis describes the development of a system for automated robotic edge deburring. The main emphasis is on accurate sensing and control of the chamfer depth. The depth is controlled through a custom built active end effector mounted to a PUMA-762 robot. The end effector's design objectives are obtained from an analysis of the combined robot arm, end effector, and deburring process dynamics. The completed unit has a bandwidth of 65 Hz, and an accuracy of 0.01 mm.

The depth is first controlled indirectly, by minimizing the variance of the normal deburring force. Several non-adaptive control algorithms based on a time series process model are investigated. Following computer simulations, experiments are performed on 1018 steel, straight edged parts. The extended horizon design is found to achieve the lowest force variance (0.11 N^2), and the smoothest chamfer, with a roughness of 9.5 μm (ISO Ra).

Simulations are performed to access the potential benefits of parameter adaptive force control for robotic deburring's time varying process dynamics. An adaptive version of the Smith predictor is found to be more robust, and have a faster response time than a non-adaptive version. A model reference adaptive control algorithm is also investigated.

A vision sensor is then developed to more directly measure the chamfer depth. The sensor has a measurement rate of 105 Hz, with an accuracy of ± 13 μm over a 1 mm range. An automated inspection system is developed using the same hardware with modified software. The information from the vision and force sensors is combined using a sensor fusion scheme. This results in a more accurate and reliable

measurement than possible using each sensor alone.

Based on the force control results, adaptive generalized predictive control is chosen to control the depth. Separate process models are used for the contact and non-contact dynamics. To adapt to changes in dynamics the contact model parameters are estimated on-line. The control algorithm is then modified to include learning control. This new algorithm is shown, both theoretically and experimentally, to improve the regulation performance of the original algorithm, without affecting its stability, for processes with a partially repeatable disturbance.

Depth controlled experiments are performed on straight edged and planar parts made of 1018 steel, and 304 stainless steel. Feedrates of 25 and 50 mm/s, and depth setpoints of 0.3 and 0.4 mm are used. In comparison to non-adaptive control, the regulation is improved with adaptive control, and further improved with the adaptive learning algorithm. The part material, depth setpoint, and feedrate are found to have little effect on the deburring performance. The system's accuracy is found to be dependent on the part geometry. For straight edged parts the accuracy is ±0.03 mm, for the most complex planar part tested it is ±0.06 mm.

ACKNOWLEDGEMENTS

The author would like to thank his research supervisor, Dr. M. A. Elbestawi, for his guidance and support throughout the course of this research.

Gratitude is also expressed to the members of my supervisory committee: Drs. D. W. Capson, R. L. Judd, N. K. Sinha, and M. Sklad.

The financial support provided by McMaster University, and a scholarship from the Natural Sciences and Engineering Research Council is also gratefully acknowledged.

Finally, I would like to thank my family, friends, and colleagues. Without your friendship and support none of this would have been possible.

TABLE OF CONTENTS

	Page
ABSTRACT	iii
ACKNOWLEDGEMENTS	v
TABLE OF CONTENTS	vi
LIST OF FIGURES	x
LIST OF TABLES	xvi
CHAPTER 1 INTRODUCTION	1
CHAPTER 2 LITERATURE SURVEY	
2.1 INTRODUCTION	10
2.2 BURR FORMATION MODELLING	10
2.3 DEBURRING PROCESS MODELLING	14
2.4 SENSORS FOR CONTROL AND INSPECTION	17
2.5 ACTIVE END EFFECTOR DESIGNS	18
2.6 CONTROL SYSTEMS	23
CHAPTER 3 ACTIVE END EFFECTOR DESIGN	
3.1 INTRODUCTION	33
3.2 DYNAMIC ANALYSIS	33
3.3 DESIGN	40
3.4 PERFORMANCE TESTING	43
3.5 CONCLUSIONS	47
CHAPTER 4 FORCE CONTROL	
4.1 INTRODUCTION	48

4.2 PROCESS MODELLING 48

4.3 NON-ADAPTIVE CONTROL: DESIGN AND SIMULATION

4.3.1 Introduction 50

4.3.2 Linear-Quadratic-Gaussian Control 51

4.3.3 Generalized Minimum-Variance Control 53

4.3.4 Extended Horizon Control 54

4.3.5 Extended PID Control 55

4.4 EXPERIMENTAL VERIFICATION 56

4.5 ADAPTIVE CONTROL: DESIGN AND SIMULATION

4.5.1 Introduction 59

4.5.2 Parameter Estimation 60

4.5.3 Adaptive Smith Predictor 61

4.5.4 Model Reference Adaptive Controller 62

4.5.5 Simulation 63

4.6 CONCLUSIONS

4.6.1 Non-Adaptive Control 66

4.6.2 Adaptive Control 66

CHAPTER 5 SENSOR DEVELOPMENTS

5.1 INTRODUCTION 68

5.2 VISION SENSOR DEVELOPMENT

5.2.1 Introduction 69

5.2.2 Optical Design 69

5.2.3 Hardware Pre-processing 72

5.2.4 Image Analysis 75

5.3 FUSION OF FORCE AND VISION SENSORY INFORMATION 81

5.4 INSPECTION SYSTEM DEVELOPMENT 84

CHAPTER 6 CHAMFER DEPTH CONTROL

6.1 INTRODUCTION 89

6.2 ADAPTIVE PREDICTIVE CONTROL: DESIGN AND SIMULATION

6.2.1 Introduction 89

6.2.2 Process Modelling 90

6.2.3 Generalized Predictive Control 93

6.3 LEARNING CONTROL: DESIGN AND VERIFICATION

6.3.1 Introduction 97

6.3.2 Development of the New Learning Algorithm 97

6.3.3 Application Example 101

6.3.4 Learning Algorithm for Robotic Deburring 104

6.4 CONCLUSIONS

6.4.1 Adaptive Predictive Control 106

6.4.2 Learning Control 107

CHAPTER 7 DEPTH CONTROL EXPERIMENTS

7.1 INTRODUCTION 108

7.2 EXPERIMENTAL SETUP

7.2.1 System Structure 108

7.2.2 Hardware Description 109

7.2.3 System Supervisor 110

7.2.4 Test Part Design and Manufacture 111

7.2.5 Robot Trajectory Generator 113

7.3 DEBURRING TEST RESULTS AND DISCUSSION 116

7.4 INSPECTION TEST RESULTS AND DISCUSSION 131

7.5 CONCLUSIONS

7.5.1 Deburring Tests 134

7.5.2 Inspection Tests 135

CHAPTER 8 CONCLUSIONS AND RECOMMENDATIONS

8.1 INTRODUCTION 136

8.2 CONCLUSIONS 137

8.3 RECOMMENDATIONS FOR FUTURE WORK 141

REFERENCES 143

APPENDIX A: FORCE SENSOR CALIBRATION 152

APPENDIX B: VISION SENSOR CALIBRATION 155

APPENDIX C: INSPECTION SYSTEM CALIBRATION 158

APPENDIX D: DERIVATION OF GPCL IN TRANSFER FUNCTION FORM 161

LIST OF FIGURES

Figure		Page
1.1	Structure of an automated robotic deburring system.	3
1.2	Geometry for chamfering a burred edge.	5
1.3	Block diagram for deburring using a position controlled robot.	5
1.4	Active end effector approach to deburring control.	7
2.1	Formation of machining burrs (after Gillespie [3]). (a) Poisson burr. (b) Entrance burr. (c) Rollover burr.	11
2.2	Method for burr dimensioning (after Gillespie [3]).	12
2.3	Normal forces from open-loop robotic deburring (reported by Bone [11]). (a) Without burrs. (b) With burrs.	15
2.4	Active triangulation method for part location measurement, based on a laser line projector and video camera.	19
2.5	Cornering with an AEE. (a) Physical rotation is required with a single-axis AEE. (b) With a two-axis AEE the controlled direction may be rotated electronically (if a conical cutter is used).	21
2.6	Strategy of Kramer and Shim [37] for orienting the end effector when performing simultaneous edge following and force control. (a) Determination of initial orientation with tool off. (b) Re-orientation of tool and start of deburring. (c) Orientation update.	25
2.7	Required compliances (inverse of impedance) in the normal and tangential directions for deburring under impedance control (after Kazerooni *et al.* [10]).	29

2.8 Block diagrams for: (a) non-adaptive force control, (b) parameter adaptive force control. 30

3.1 Structure of the model used for the dynamic analysis. 34

3.2a Effect of the AEE design parameters on the normalized frequency response of the dynamic model. (a) Bandwidth, ω_b. (b) Masses m_3, and m_4. 38

3.2b Effect of the AEE design parameters on the normalized frequency response of the dynamic model. (c) Stiffness k_3, and damping c_3. (d) Acceleration force component. 39

3.3 The new AEE design. (a) Side view. (b) Front view. 42

3.4 AEE step input responses for 0.1 mm and 0.2 mm position commands. 44

3.5 AEE frequency response for a position command amplitude of 0.05 mm. 44

3.6 Direct transfer function for the AEE without the vision sensor. (a) Real part. (b) Imaginary Part. (c) Coherence. 46

3.7 Direct transfer function for the AEE with the vision sensor. (a) Real part. (b) Imaginary Part. (c) Coherence. 47

4.1 Structure of the force control system. 49

4.2 Force and command variance for LQG control as a function of λ. 52

4.3 Simulated force response for LQG control. 52

4.4 Simulated force response for GMV control. 53

4.5 Simulated force response for EH control. 55

4.6 Simulated force response for EPID control. 56

4.7 Comparison of the force control algorithms investigated. (a) Force variance. (b) Position command variance. (c) Chamfer surface roughness. 58

4.8 Experimental force response for LQG control. 59

4.9 Experimental force response for EH control. 59

4.10 Structure of the Adaptive Smith Predictor. 61

4.11 Structure of the Model Reference Adaptive Controller. 62

4.12 Simulated force response for a non-adaptive Smith predictor. 64

4.13a Simulated force response for the ASP. 64

4.13b Simulated model gain for the ASP. 65

4.14 Simulated force response for the MRAC algorithm. 65

5.1 The vision sensor shown mounted on the AEE. (a) Side view. (b) Front view. 73

5.2 (a) Sectional view of the vision sensor's triangulation geometry (section A-A in Figure 5.1(a)). (b) Detail. 74

5.3 Image analysis of the light stripe for the deburring case. 77

5.4 Image analysis results for the deburring case. (a) Stripe centre vs. line number. (b) Curvature index vs. line number. 80

5.5 Scenario for sensor fusion during a deburring pass. 84

5.6 Image analysis of the light stripe for the inspection case. 85

5.7 Image analysis results for the inspection case. (a) Stripe centre vs. line number. (b) Curvature index vs. line number. 88

6.1 Comparison of the prediction error, mean error, and mean absolute error when subjected to model mismatch. 93

6.2 Simulated deburring pass under adaptive GPC. (a) Chamfer depth. (b) Mean absolute error. (c) Model gain. 96

6.3a Experimental and computed output variances over 11 trials for the edge following application under GPCL. 103

6.3b Experimental and computed input variances over 11 trials for the edge following application under GPCL. 104

6.4 Sample edge following response under GPCL. 104

6.5 Simulated chamfer depth response for adaptive GPCL. 106

7.1 Structure of the robotic deburring system. 109

7.2 Planar test part designs and their associated tool paths for deburring. (a) Designs 1 and 2. (b) Design 3. 113

7.3 Special tool orientation for circular edge segments. 115

7.4 Tool path and orientation for inspection of an edge with linear and circular segments. 116

7.5 Depth response for a straight edged part deburred under non-adaptive GPC. 118

7.6 Depth response for a straight edged part deburred under adaptive GPC. 118

7.7a Test results for a straight edged part deburred under adaptive GPCL. (a) Depth, d. (b) Model gain, $B(1)/A(1)$. (c) Mean absolute prediction error, $\bar{e}$. 119

7.7b Test results for a straight edged part deburred under adaptive GPCL. (d) Gain k_f. (e) Average tool position from learning passes, $d^*(t)$. 120

7.8 Test results for a 304 stainless steel straight edged part deburred under adaptive GPCL. (a) Depth, d. (b) Model gain, $B(1)/A(1)$. 121

7.9 Depth response for a design 1 part deburred under non-adaptive GPC. 123

7.10 Depth response for a design 1 part deburred under adaptive GPCL. 123

7.11 Depth response for a design 2 part deburred under adaptive GPCL. 125

7.12 Depth response for a design 2 part deburred under adaptive GPCL with a feedrate of 50 mm/s. 125

7.13 Depth response for a 304 stainless steel design 2 part deburred under adaptive GPCL. 126

7.14a Test results for a design 3 part deburred under adaptive GPCL. (a) Depth, *d*. 126

7.14b Test results for a design 3 part deburred under adaptive GPCL. (b) Model gain, *B(1)/A(1)*. (c) Average tool position from learning passes, d^*. 127

7.15 Depth response for a design 3 part deburred under adaptive GPCL, with a depth setpoint of 0.3 mm. 129

7.16a Test results for a design 3 part deburred under adaptive GPCL at a feedrate of 50 mm/s. (a) Depth, *d*. 129

7.16b Test results for a design 3 part deburred under adaptive GPCL at a feedrate of 50 mm/s. (b) Model gain, *B(1)/A(1)*. (c) Average tool position from learning passes, d^*. 130

7.17 Comparison of the frequency distributions of the depth measurements obtained by the inspection system and by microscope for a straight edged part (whose control results were shown in Figure 7.7). 133

7.18 Comparison of the frequency distributions of the depth measurements obtained by the inspection system and by microscope for a design 3 part (whose control results were shown in Figure 7.16). 133

A.1 Calibration data and calibration lines for the force sensor. (a) Normal direction. (b) Tangential direction. 154

B.1 Calibration data and calibration line for the vision sensor. 157

C.1 Sectional view of a chamfered edge, showing definitions of depth, and angles. 159

C.2 Calibration data and lines for the inspection system. (a) Depth. (b) Top Angle. (c) Side Angle. 160

LIST OF TABLES

Table		Page
3.1	Test case parameters used for the dynamic analysis.	40
6.1	Effect of the tuning parameters ($N2$, NU, t_1) on GPCL's variance gains for the edge following application.	103
7.1	List of errors detected, method of detection, and troubleshooting advice provided by the system supervisor.	112
8.1	Potential applications for the theoretical and technological developments.	142

CHAPTER 1

INTRODUCTION

To be competitive in today's marketplace manufacturers must be able to change quickly in response to customer demands. This flexibility must be attained without sacrificing quality or productivity. Computer Integrated Manufacturing Systems (CIMS) seek to achieve this goal by integrating Computer-Aided Design (CAD) with Computer-Aided Manufacturing (CAM). CAM involves multi-level planning and control, from factory-wide to the single machine level. At the machine level, for CAM to be successful, productivity and quality must be maintained throughout. In many cases, current Computer Numerically Controlled (CNC) machines are able to achieve this. However, some operations require further developments in sensors and control systems to realize successful automation. Of these deburring is of prime importance, for reasons which will now be discussed.

In machining, burrs are formed at part edges by the plastic flow of material. The burrs must be removed for a variety of reasons: to guarantee component fit, prevent injury to workers, enhance part appearance, and to improve the effectiveness of further finishing operations. Because deburring is often performed at the final stage of manufacturing, where parts have their highest added value, quality control is an absolute necessity. Despite this requirement, even in today's most fully automated factories it is still a common sight to see dozens of workers manually

deburring parts produced by CNC machines. The manual operation is costly and inefficient; and is also plagued by varying operator skill, a poor working environment (dirty, noisy and dangerous), and a high job turnover rate. Automated robotic deburring systems have been investigated for a number of years as a solution to these problems.

A structure for an automated deburring system is shown in Figure 1.1. The system involves three main stages. The first stage involves high-level task planning for selection of the appropriate deburring tools, and planning of the robot's movements. Low-level control is then used to correct for planning errors during the deburring pass. In the third stage the part is automatically inspected. Based on the inspection results it may be necessary to return to the task planning stage for rework. If the part has been successfully deburred, task completion is reached. This thesis will be concerned with the second and third phases, and with control of the deburring pass in particular.

Low-level control is used to correct on-line for the inevitable errors in the planned motion. Successful low-level control requires sensor(s) which accurately measure the controlled variable, suitable hardware, and an appropriate control strategy.

Machining burrs are typically removed from part edges by chamfering. Carbide cutters are commonly used because they are capable of high material removal rates with a variety of materials. They also have the advantage that they blunt rather than undergo significant geometrical wear [1, 2]. The geometry for chamfering a burred edge is shown in Figure 1.2. A typical chamfer is 0.25-0.4 mm $\times$ 45° [3]. Note that even if the edge is burr free the chamfering operation is still

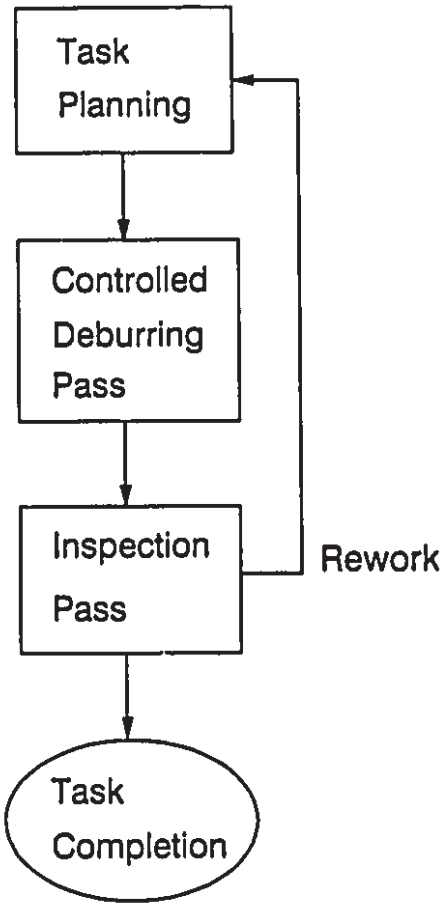

Figure 1.1 Structure of an automated robotic deburring system.

necessary, for the reasons previously mentioned. The chamfer depth must often be within specific tolerances. While the large workspace and high mobility of robots make them well suited to deburring, these attributes also result in a structure with low stiffness and low positioning accuracy. The low stiffness causes significant deflections to result from the deburring forces. These deflections along with the robot's inaccuracy, make it difficult to control the depth using a standard position controlled robot. A block diagram for such a system is shown in Figure 1.3. Note that part fixturing errors and burrs are other potential disturbances. To obtain more accurate control it is necessary to obtain sensor feedback related to the chamfer depth. For chamfering with carbide cutters the cutting process is often modelled as a gain between the material removal rate and the force. This gain is dependant on the part material. For a given material, if the burrs are small relative to the depth, and the feedrate is constant, the depth will be proportional to the force. When there are material hardness or feedrate variations, or the burrs are large relative to the depth, the force is no longer an accurate measure of the depth. Force control is also prone to overshoot or even instability at the time of initial tool/part contact. Despite these facts, few alternate or additional sensors have been investigated for robotic deburring.

Given an accurate sensor measurement, the depth can be controlled by performing corrections to the robot's path. These corrections are typically performed in the direction normal to the chamfer surface (shown in Figure 1.2). The corrections may be performed using either passive or active control.

With passive control, a passive compliant device, consisting of springs and dampers, is added between the robot's wrist and the deburring tool. This method is

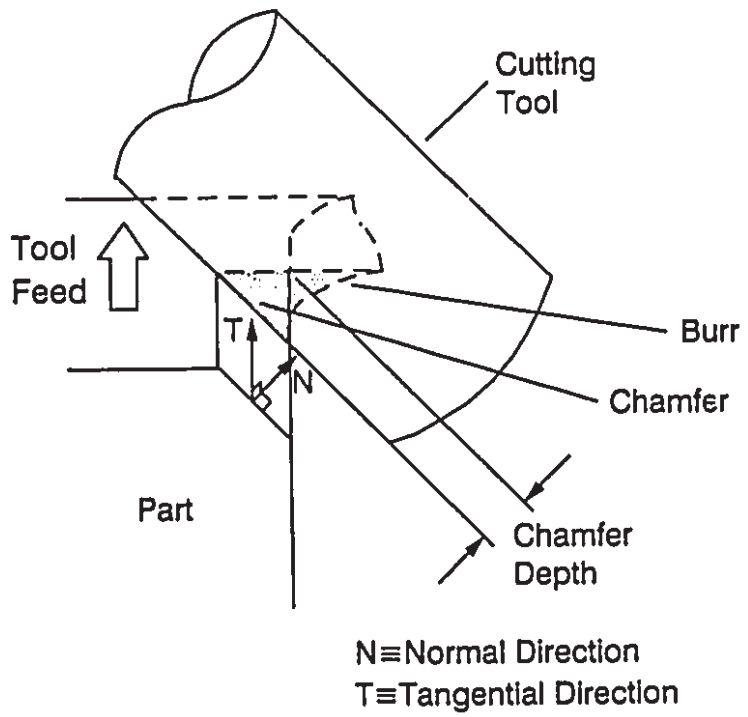

Figure 1.2 Geometry for chamfering a burred edge.

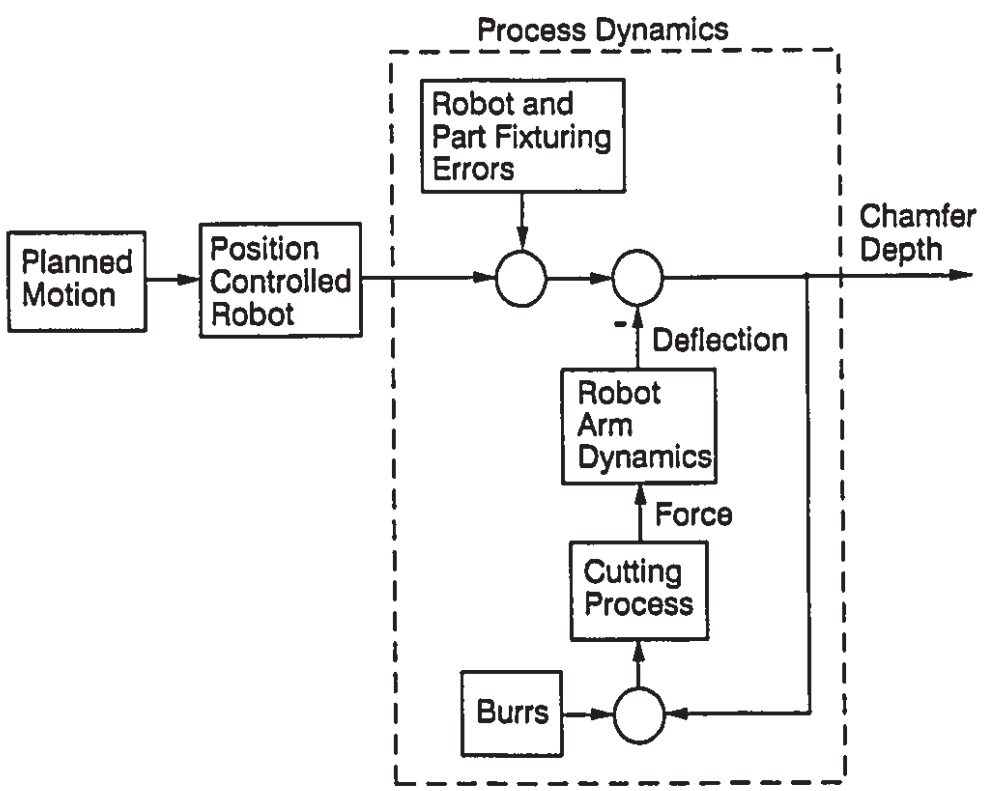

Figure 1.3 Block diagram for deburring using a position controlled robot.

simple to implement, but is limited in its ability to correct for the robot's inaccuracy, and other disturbances. Improved results may be obtained using active control.

In terms of hardware, with active control the corrections can be performed either through the robot's position control system, or by a completely external active end effector system. While the first approach requires minimal external hardware, the low bandwidth and accuracy of most industrial robots limits performance. With the second approach, the robot performs the gross motion of the tool around the part, while the fine motion corrections are performed by an active end effector. This approach is illustrated in Figure 1.4. An active end effector consists of an actuator (electric, pneumatic, or hydraulic) mounted between the robot's wrist and the tool. Since only the small end effector (and not the entire arm) is controlled, greater position control bandwidth and accuracy can be achieved. Because the end effector is actively controlled its dynamic behaviour is not limited to the 2nd order response of a passive device. If computer control is used almost any control algorithm may be implemented. When the research reported in this thesis began in 1988, only simple fixed parameter control algorithms had been used. For good performance these schemes require the process dynamics to be relatively time invariant. In practice however, the arm's stiffness varies with its configuration, and the cutting process is affected by changes in cutting conditions and part material. Parameter adaptive control, where the controller parameters are based on a process model estimated on-line, has the potential for improved performance over the non-adaptive schemes.

Iterative learning control may be used as an alternative to, or an addition to, adaptive control. Whereas adaptive control adapts during a single repetition of a task, iterative learning control's aim is to improve the performance of a task over a

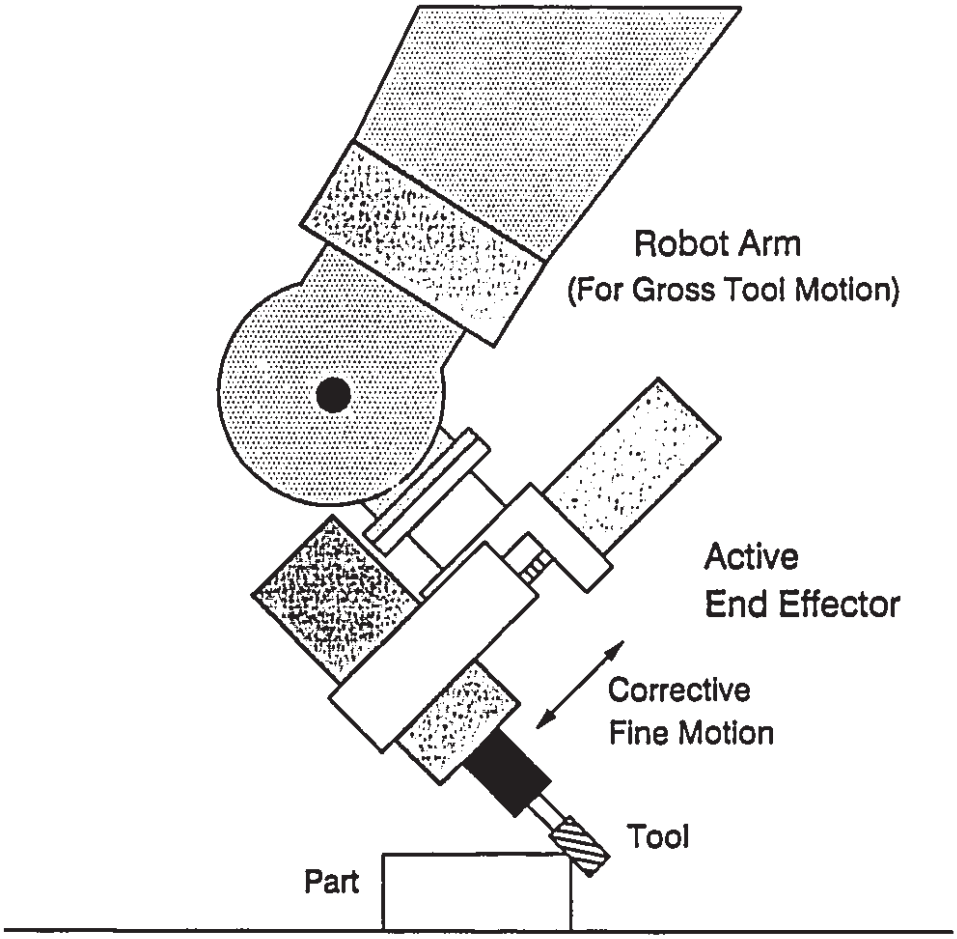

Figure 1.4 Active end effector approach to deburring control.

series of repetitions. In many industrial applications, including deburring, a robot's motions are repeated over and over, making robotics an ideal candidate for learning control. In comparison to conventional feedback control, learning control has the advantages that it may be computed off-line, and is inherently more stable since it involves only a feedforward term. At the start of this research there were no published reports on the application of learning control to robotic deburring.

A further area which has received little attention in deburring research is automated inspection. The improvement in production rate achieved by an automated deburring system may be negated if the parts are manually inspected. The solution to this problem is to develop a deburring system with 100% reliability (a seemingly impossible task), or to automate the inspection process.

This thesis describes the development of an automated robotic edge deburring system based on an industrial robot equipped with a custom built active end effector. A carbide rotary file, driven by a pneumatic grinder, will be used as the cutting tool. The system is concerned with controlling the chamfer depth during the deburring pass, and with verifying the deburring performance in a secondary inspection pass. The state of current research in the area is reviewed in Chapter 2. The active end effector is designed in Chapter 3, based on a dynamic analysis of the combined robot arm, end effector, and deburring process dynamics. The completed unit is then performance tested. In Chapter 4 the deburring system is tested using several parameter adaptive and non-adaptive force control algorithms. The algorithms' performance are compared based on the results of computer simulations and deburring experiments. To overcome the limitations of force sensing, in Chapter 5, a new vision sensor is developed to provide a more direct measurement of the depth.

The information from the force and vision sensors is combined using a sensor fusion approach, to obtain a more accurate and reliable depth measurement than possible using each sensor alone. The development of the automated inspection system is then described. The system uses the vision sensor hardware with software modified for the inspection case. In Chapter 6 adaptive predictive control is applied to the depth control problem. The control algorithm is then modified to include learning control. The performance of this new algorithm is examined both theoretically, and experimentally in non-contact edge following tests. Depth controlled deburring experiments are then performed using these algorithms in Chapter 7. The experiments are performed on straight edged and planar parts. Details of the experimental setup are first described, followed by discussions on the results of the deburring and inspection system tests. In Chapter 8 the conclusions of the research, and recommendations for future research, are presented.

CHAPTER 2

LITERATURE REVIEW

2.1 INTRODUCTION

In this chapter the current literature related to robotic edge deburring is reviewed. This has been broken down into five areas: burr formation modelling, deburring process modelling, sensors for control and inspection, active end effector designs, and control systems.

2.2 BURR FORMATION MODELLING

Models for the prediction of burr formation are desirable for two reasons: first, they may be used to help alter production methods in order to minimize burr formation, and second, they may be used to predict burr size and location in order to help plan the deburring operation. Several researchers have studied and modelled the formation of machining burrs.

Gillespie [3-6] has written extensively on the formation, classification, and removal of machining burrs. He classified burrs into four types: Poisson burrs, entrance burrs, rollover burrs, and tear burrs. A Poisson burr is the most common type, and is formed whenever a cutting edge extends past the edge of the workpiece, as shown in Figure 2.1(a). An entrance burr may be formed when a cutting edge first enters the workpiece, as shown in Figure 2.1(b). A rollover burr is formed when the

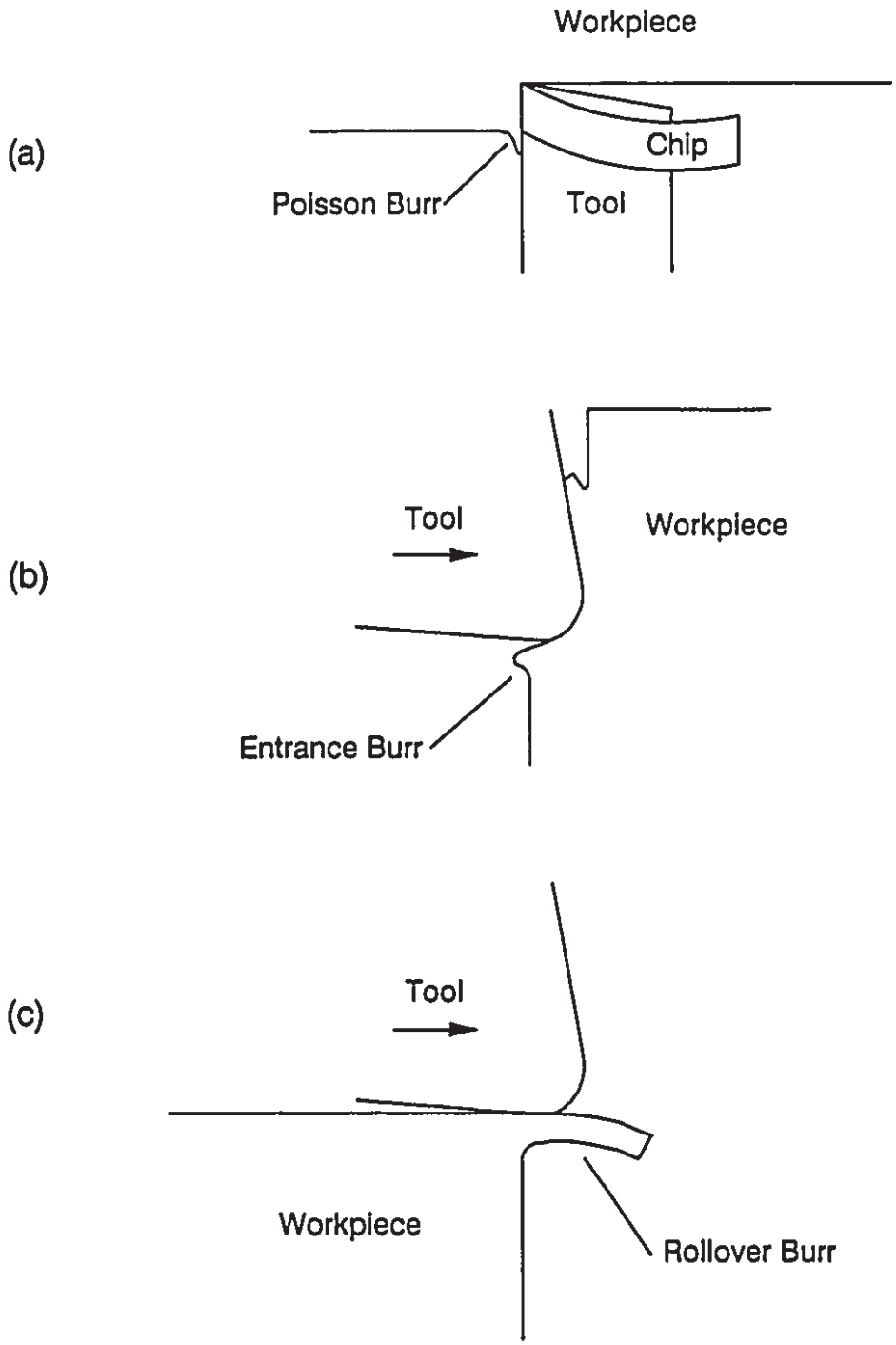

Figure 2.1 Formation of machining burrs (after Gillespie [3]). (a) Poisson burr. (b) Entrance burr. (c) Rollover burr.

cutting edge exits the workpiece and the chip is bent over rather than cut. This situation is illustrated in Figure 2.1(c). When chips are torn instead of being sheared from a workpiece, tear burrs are formed. Since Poisson, rollover, and tear burrs have common physical characteristics, they can all be dimensioned according to their base radius, height, and thickness, as shown in Figure 2.2.

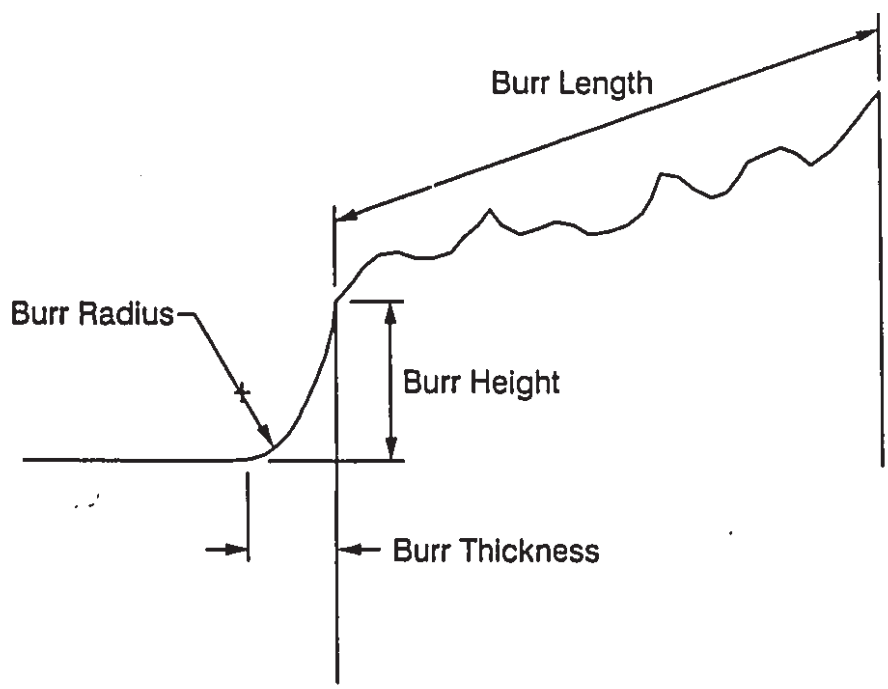

Figure 2.2 Method for burr dimensioning (after Gillespie [3]).

Gillespie has developed numerous qualitative and quantitative burr formation models [3, 4]. For turning operations which tend to produce a large Poisson type exit burr, he suggests that sharp tools with a large rake angle and shallow depths of cut be used to reduce burr formation. For drilling of plain carbon steel, he obtained the empirical relation:

$$T = C_1 H^{-1.72} P^{0.84} L^{-0.36} f^{0.86} \tag{2.1}$$

where T is the burr thickness, C_1 is a constant, H is the helix angle, P is the point

angle, and L is the lip clearance angle, and f is the feedrate. This shows that increasing the helix angle has the greatest effect in reducing the burr thickness. For a fixed drill geometry the thickness was given by:

$$T = C_2 N^{-0.783} B^{-0.998} K^{-0.007} \tag{2.2}$$

where C_2 is a constant, N is the spindle speed, B is the workpiece hardness, and K is the stiffness of the drilling system. This result shows that the workpiece hardness is the most significant parameter, and that a more ductile workpiece will produce a thicker burr. For milling operations he states that dull cutters significantly increase burr size, higher feedrates reduce burr height, and changes to the helix angle reduce some burr sizes while increasing others. For the general case of Poisson burrs he performed a theoretical analysis, which modelled the tool point as a half cylinder pushed into a perfectly plastic material, but found that it underestimated the burr size by an order of magnitude [5]. More recently he concluded that the field of burr formation modelling is still searching for a mathematical solution to the problem of plastic flow at a boundary [6].

Iwata *et al.* [7] studied burr formation by direct observation, using a micro machining device located inside a Scanning Electron Microscope (SEM). They determined the effect of the edge angle of the workpiece on the burr size. A very slow cutting speed of only 0.15 mm/min was used. They were also able to explain the occurrence of fracture during burr formation based on a finite element method analysis. Burr size was not predicted by the model.

Dornfeld and Ko [8] have developed a burr formation model for materials exhibiting both ductile and brittle behaviour. The initial negative shear angle is used to predict material fracture during burr formation. The values for the initial negative

shear angle predicted from their model corresponded well with values measured during micromachining of aluminum alloys inside a SEM. As with the work of Iwata *et al.* [7], the model does not predict the size of the burrs, and was only verified for a very slow cutting speed (0.1 inch/min).

Clearly more work is needed to accurately model burr formation under realistic cutting conditions. Even if accurate models were available the conditions necessary for minimizing burrs may not be economically viable. Frequent resharpening or replacement of cutting tools for example. The result is that burrs will be formed, and deburring will continue to be necessary.

2.3 DEBURRING PROCESS MODELLING

Machining burrs are typically removed from part edges by chamfering. Most robotic deburring systems control the chamfer depth indirectly by controlling the cutting force. To obtain the correct depth the relationship between the desired depth and appropriate force setpoint must be known. For carbide rotary files the cutting force has been taken to be proportional to the material removal rate by several researchers ([1, 9, 10] for example). Since the material removal rate is equal to the feedrate times the cross sectional areas of the chamfer and burr, and the burr size is highly variable, a control strategy based on constant force will result in an uneven chamfer. However, Kazerooni *et al.* [10] have shown that burr size variations have little effect on the total area (and hence the force) when projected in the direction normal to the edge. This conclusion is supported by results given by Bausch [9] and Bone [11], in which the presence or absence of burrs had no noticeable effect on the normal force. Sample force results are shown in Figure 2.3. A consistent chamfer can

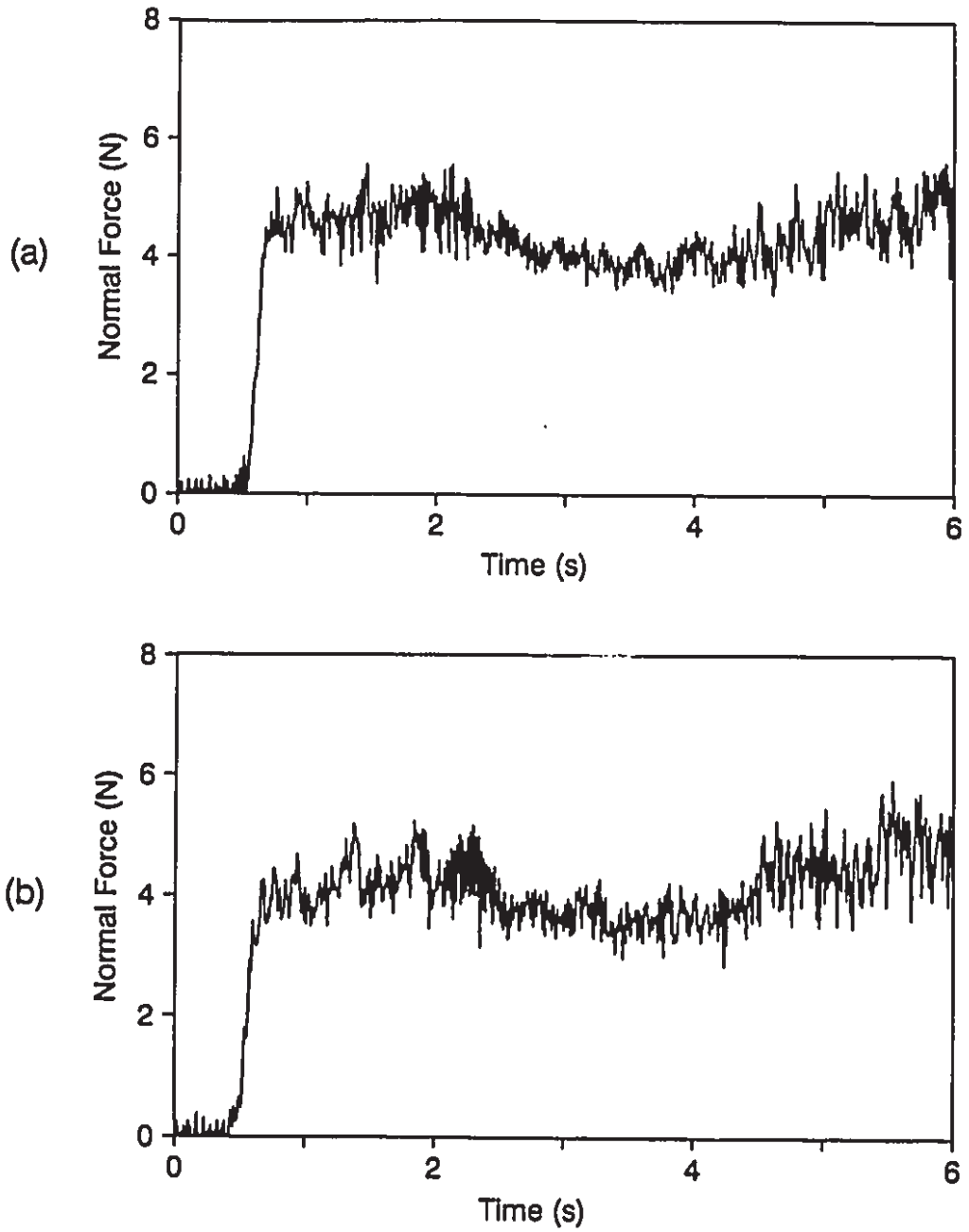

Figure 2.3 Normal forces from open-loop robotic deburring (reported by Bone [11]). (a) Without burrs. (b) With burrs.

therefore be obtained by controlling the normal force. This is the predominant control strategy in robotic deburring and will be discussed further in section 2.6. In equation form the model is:

$$F = K_c d^2 f \tag{2.3}$$

where F is the normal component of the cutting force, K_c is the cutting stiffness, d is the chamfer depth, and f is the feedrate.

A more general non-linear form:

$$F = K_c d^{n1} f^{n1} \tag{2.4}$$

where $n1$ is the depth exponent, and $n2$ is the feedrate exponent; and a linearized form:

$$F = K_c' df \tag{2.5}$$

were investigated by Bone [11]. When fit to force data for 1018 steel, 6061-T6 aluminum, and 304 stainless steel, the average R^2 (coefficient of determination) values were 0.86 and 0.80, for equations 2.2 and 2.3 respectively. Based on these values both models provided a good fit to the data, and the non-linear form provided the best fit. Interestingly, the average feedrate exponent was 0.7, which is consistent with those cited for the milling process [12].

Roberts and Engel [13] performed a similar analysis for chamfering of Inconel 718 (a high strength, heat resistant alloy used in aerospace components) using a small diameter (3 mm) carbide cutter. Tool wear was found to be significant, and was modelled by including a term proportional to the amount of material removed. Their complete model is:

$$F = k_1(1 + k_2 M) d^{k3} f^{k4} N^{k5} \tag{2.6}$$

where M is the amount of material removed, N is the spindle speed, and $k_{1\text{-}5}$ are model parameters. When this model was used to predict the depth, given values for F, M, f, and N, the standard deviation of the error was 0.03 mm.

From the models discussed it can be seen that the relationship between the depth and force is a complex function of the tool, part material, and cutting conditions. If the actual conditions are not consistent with those used to obtain the model, or the measurements used are inaccurate, the depth estimate from the model will be inaccurate. If there are material hardness variations, or the burrs are large relative to the chamfer size, this will be the case. Force control is also prone to overshoot or even instability at the time of initial tool/part contact [14, 15].

2.4 SENSORS FOR CONTROL AND INSPECTION

In robotic deburring, despite its limitations, force sensing is predominant and few additional or alternative sensors have been investigated.

Guvenc and Paul [16] proposed the use of acceleration feedback to obtain the tool position. However, since this involves double integration of the acceleration signal the method is very sensitive to noise (in particular a D.C. bias) in practice.

Dornfeld and co-workers [17-19] have investigated the use of Acoustic Emission (AE) as a feedback signal for controlling very shallow chamfers. AE was found to be sensitive to both the chamfer and burr size. They propose to combine the AE feedback with force feedback using a fuzzy logic-based controller. Their suggestion that the force is insensitive to chamfers less than 0.6 mm deep contradicts the results of Hollowell and Guile [20], and Starr and Loucks [21] who controlled smaller chamfers using force feedback.

Loucks *et al.* [14] used a vision sensor to determine the orientation of a part prior to deburring. The sensor obtained the orientation by measuring the location of a particular part feature using active triangulation. A laser line projector was used as the structured light source, and the image was measured by a video camera. This method is illustrated in Figure 2.4. The measurement was then used to correct the robot's motion program prior to deburring. The deburring was performed under force control. A similar sensor and two pass approach was used by Whitney *et al.* [22] for robotic grinding of weld beads. In a pre-grinding pass a laser triangulation sensor measured the cross sectional area of the bead at a rate of 1 Hz [23]. The vision processing was performed on an 8 Mhz Intel 80286-based microcomputer. The measurements were then used to plan a number of force controlled grinding passes. More recently, Seliger and Hsieh [24] used a laser sensor to track the base of the burrs in order to plan the robot's deburring path, and Dornfeld [19] used one to measure burr size and location prior to deburring.

For automated inspection, the only system mentioned in the literature is by Selleck and Loucks [25]. The system uses a laser range sensor to measure chamfer depth, and angles relative to the top and side surfaces of the part. The vision algorithms were programmed in C++ on VME-based vision processing boards controlled by a Motorola 68020-based computer. The measurement rate was 2 Hz.

2.5 ACTIVE END EFFECTOR DESIGNS

In Active End Effector (AEE) systems, an end effector which allows independent position adjustment is attached between the robot's wrist and the cutting tool. This is distinct from the use of an X-Y table to move the part while the tool is

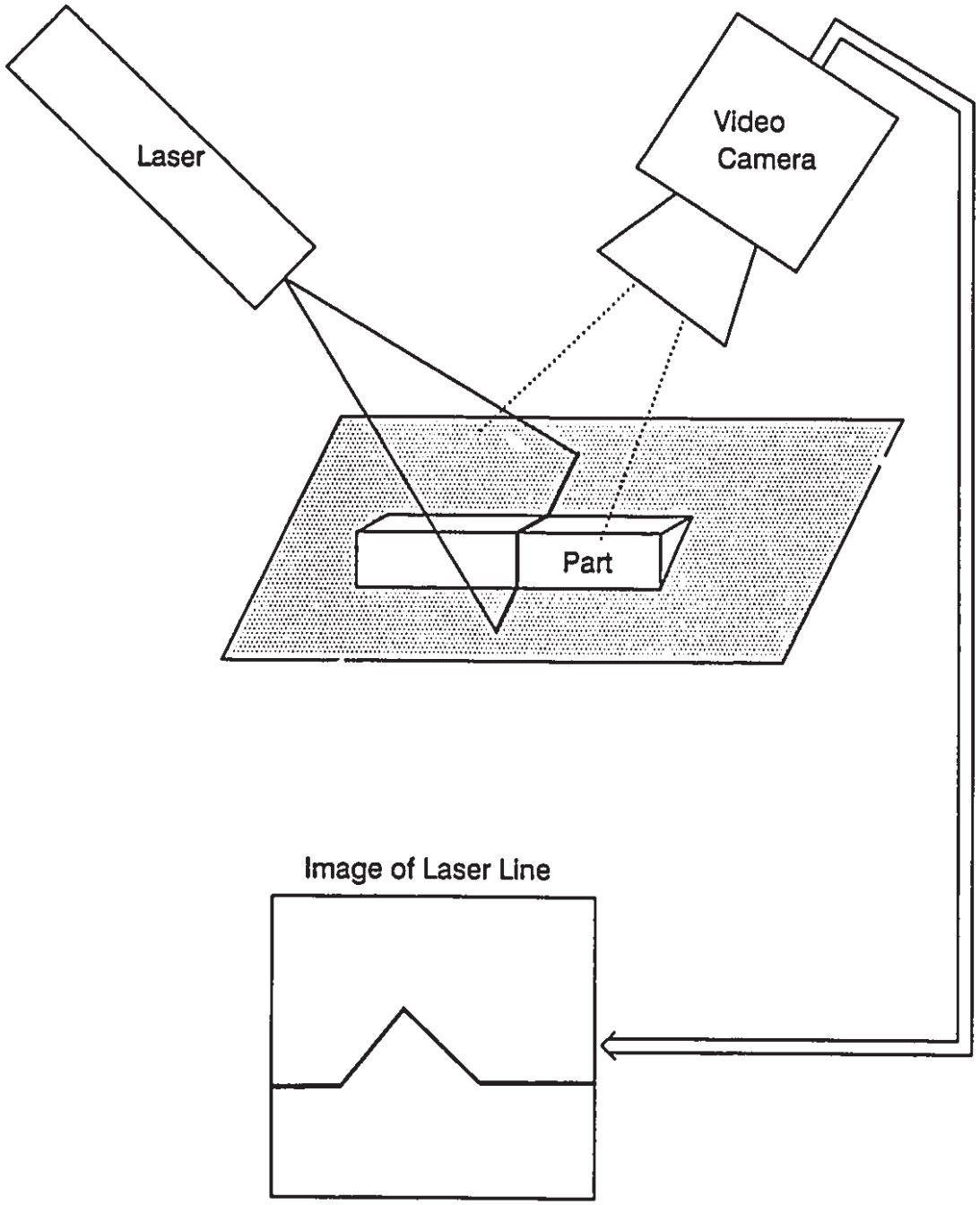

Figure 2.4 Active triangulation method for part location measurement, based on a laser line projector and video camera.

held by the robot. This method has been applied to deburring by Kramer *et al.* [2], and Dornfeld and Erickson [18]. Similarly, an X-Y table has been used with the tool rigidly mounted by Kazerooni [26], and by Starr and Loucks [21]. The table method has the advantage that X-Y tables are commercially available, but is limited in terms of part size, weight, and geometry.

The first AEEs were not developed for robotic deburring. Paul *et al.* [27] and Zalucky and Hardt [28] developed AEEs to reduce robot arm deflections. The performance of both systems was limited by the slow response of the hydraulic actuators used.

Hollis [29] has developed a two-axis AEE driven by linear electric motors combined with flexure springs for use mainly in electronic assembly and inspection operations. The absence of transmission elements, motor brushes, and sliding or rolling bearings makes the device free of wear. When combined with a robot, precision improvements of several orders of magnitude were achievable.

A system by Tlusty and Wegerif [30] improved the accuracy of a robotic routing operation by compensating for the deflections due to the cutting forces with a single-axis AEE. The AEE design was based on a cam follower driven by an electric servo motor. When applied with a Cincinnati Milacron T3-776, the arm deflections were reduced from 0.75 to 0.05 mm. The robot's positioning errors were not eliminated, however.

Single- and two-axis AEEs have been used for deburring. With a single-axis design the end effector must be rotated by the robot to keep the axis normal to the edge. The two-axis designs have the advantage that this rotation may be performed electronically if a conical cutter is used [31]. The two approaches are shown in Figure

2.5. The disadvantages of the later approach are that the cutter suffers from concentrated wear [32], plus the cost and difficulty involved in adding the second axis.

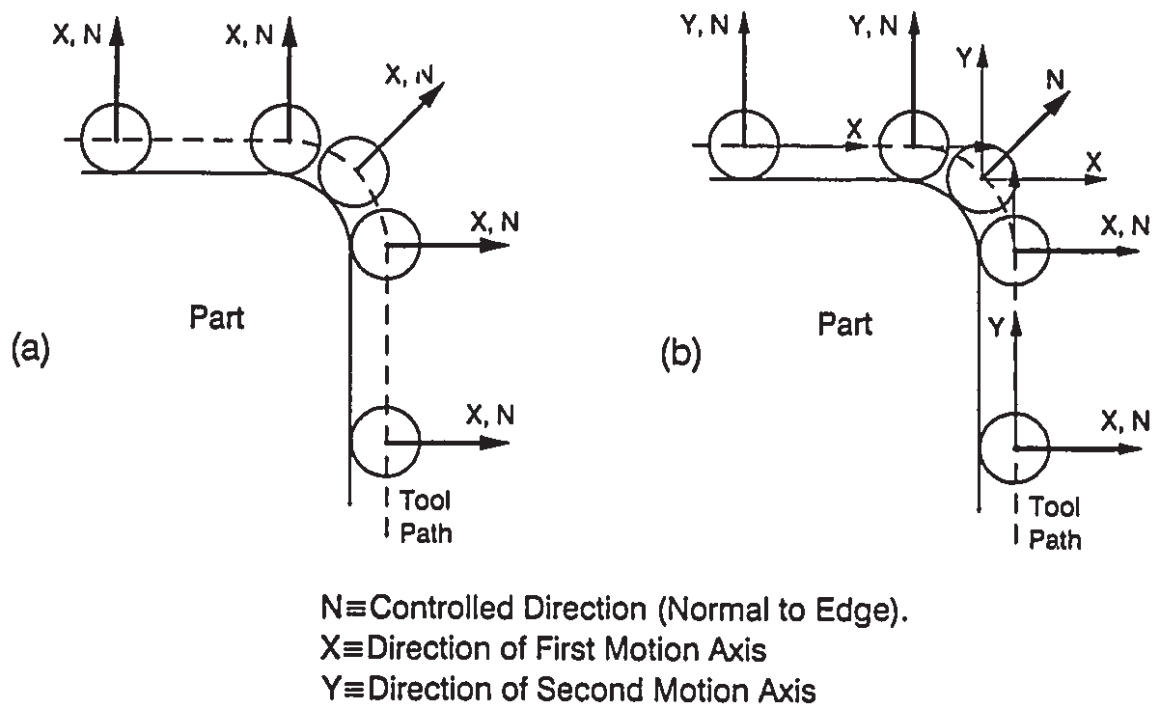

Figure 2.5 Cornering with an AEE. (a) Physical rotation is required with a single-axis AEE. (b) With a two-axis AEE the controlled direction may be rotated electronically (if a conical cutter is used).

An AEE design based on a five-bar linkage known as a Watts straight line mechanism has been developed by Kazerooni [33]. It allows approximate straight line motion in two orthogonal directions over a range of 4 mm. While the design is mechanically very stiff its actual impedance (force/deflection as a function of frequency) can be computer controlled. This control approach will be further discussed in the next section. While the unit was developed with the robotic

deburring application in mind, no deburring results have been published at present.

Two AEEs (single- and two-axis designs) were developed for robotic deburring by Hollowell and Guile [20]. Both designs pivot the tool so that the motion at the contact point is not linear, but along a slight arc. The single-axis design regulates the normal cutting force by controlling the magnetic flux of a solenoid. The two-axis design uses microstepping motors coupled to linear ball screws for its actuators. The deburring results using each device will be discussed in the next section.

A two-axis AEE with each axis consisting of a linear ball slide driven by a linear ball screw coupled to a D.C. servo motor was developed for deburring by Bone [11]. This design has the advantage that it provides decoupled linear motion, unlike the designs of Kazerooni [33], and Hollowell and Guile [20]. It has the disadvantage that the motor brushes, ball screws and ball slides are subject to slight wear. However, these devices have been, and are still for the most part, standardly used in commercial X-Y tables and industrial machine tools. Deburring results will be discussed in the next section.

Roberts *et al.* [32] have designed an AEE for deburring which extends the pivoted, solenoid driven, single-axis design of Hollowell and Guile [20] to two axes. Like Hollis's [29] design a flexure spring is used in place of a bearing to eliminate wear. Based on simulation results they conclude that a mechanically stiff actuator, such as one driven by a ball screw, would require a very high bandwidth in order to match the deburring performance of their mechanically flexible device. The necessary bandwidth was unspecified.

2.6 CONTROL SYSTEMS

The predominant approach in robotic deburring for controlling the chamfer depth has been to control the force normal to the edge and the feedrate tangential to the edge. This is in fact a particular case of the hybrid position/force control strategy developed by Raibert and Craig [34], in which the degrees-of-freedom are specified as either position or force controlled. Since feedrate control is straightforward, methods to control the normal force have been the main research interest.

Conventional Proportional-Integral-Derivative (PID) control has been applied to robotic deburring by several researchers. A discretized form of the algorithm is:

$$x(t) = [K_p + K_d(1 - q^{-1})/T + K_i T q^{-1}/(1 - q^{-1})]E(t) \tag{2.7}$$

where $x(t)$ is the commanded normal direction position correction, $E(t)$ is the force error, K_p is the proportional gain, K_d is the derivative gain, K_i is the integral gain, T is the sampling interval, t is the discrete time, and q^{-1} is the backward shift operator.

Stepien *et al.* [35] used PID control implemented through the control system of GE P-50 robot to maintain deburring forces of 1-15 N within 2 N, at feedrates of 10-90 mm/s, with a straight edged part. The force errors were found to be a function of the feedrate, but not the force setpoint. The controller was tuned by analyzing the root locus of the system. Haefner *et al.* [36] also used PID control and a GE P-50 robot. On a 304 stainless steel straight edge they maintained a deburring force of 3±1 N. They recommend that an AEE be used to obtain better performance.

Hollowell and Guile [20] compared the deburring performance of an ASEA IRb-6 robot equipped with single- and two-axis AEEs (whose designs were discussed

in section 2.3). A damping control law, which is equivalent to integral control, was used with the two-axis AEE, while the single-axis AEE controlled the force by controlling the flux of its solenoid actuator. Experiments were performed on straight edged Inconel parts. At 10 mm/s the chamfer depth was 0.22±0.04 mm. At 30 mm/s the depth was 0.14±0.02 mm for the single-axis AEE, and 0.14±0.05 mm for the two-axis AEE. They concluded that the single-axis design produced smoother chamfers because of its higher force control bandwidth.

Bone [11] used the following extended form of discrete PID:

$$x(t) = (r_0 + r_1 q^{-1} + \ldots + r_n q^{-n}) E(t) / (1 - q^{-1}) \tag{2.8}$$

where r_0 to r_n are parameters derived from a time series model of the process dynamics. The model was obtained off-line using least squares identification. The controller was tuned based on its root locus, and simulated step response. Using a two-axis AEE with a PUMA-560 robot, 1 N force errors were achieved for mild steel, straight edged parts deburred at 25 mm/s.

Acoustic emission feedback was used with a simple proportional controller by Dornfeld and Erickson [18]. The controller was manually tuned. An ASEA IRb6 robot provided the gross motion, while the fine motion was provided by an X-Y table. For a straight edged 6061-T6 aluminum part a depth of 0.25±0.06 mm was achieved at a feedrate of 8 mm/s.

A system for combined edge following and force control has been developed by Kramer and Shim [37]. An Adept One robot equipped with a passive end effector, and through the arm control, were used. The correct end effector orientation was maintained using the search strategy shown in Figure 2.6. The initial orientation is found by moving into the edge with the tool off. Assuming the friction in the tool's

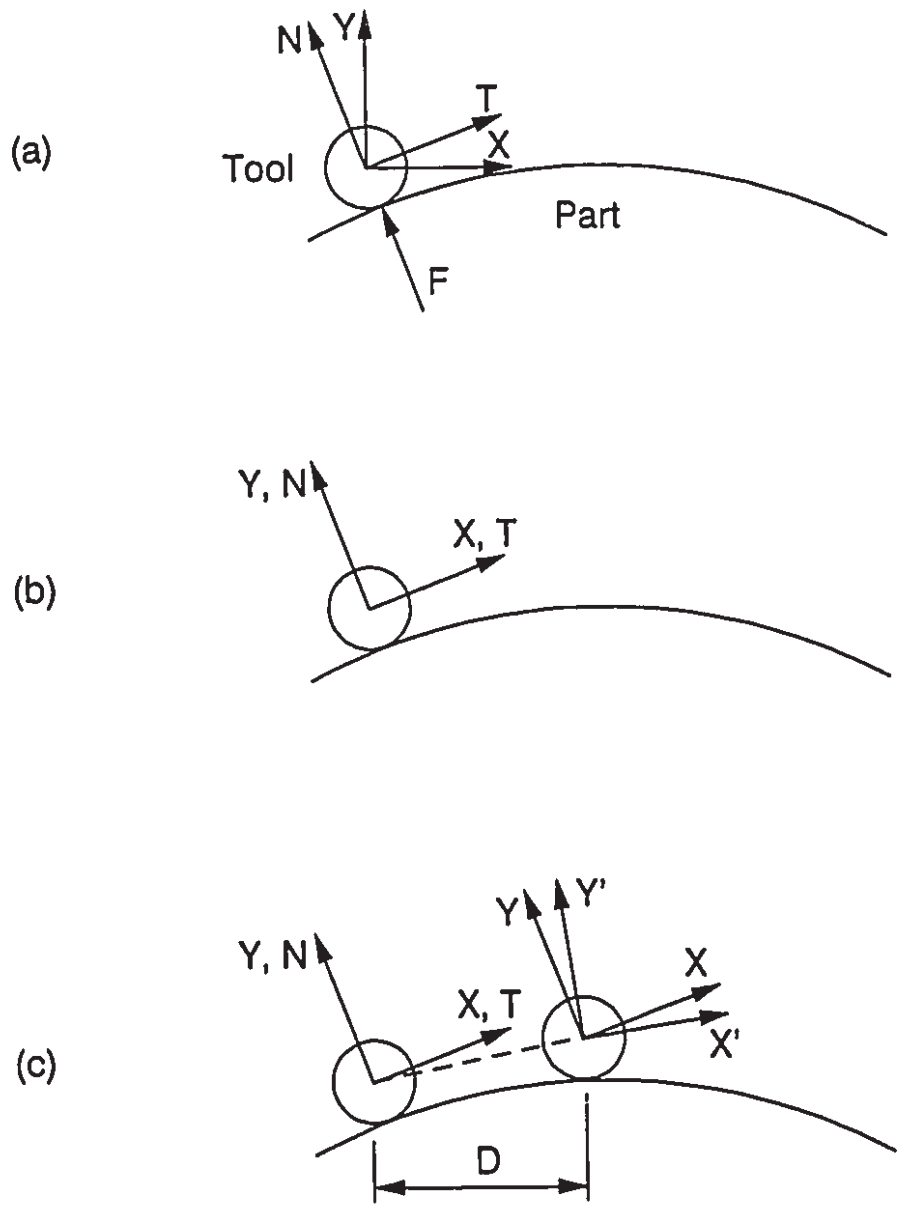

Figure 2.6 Strategy of Kramer and Shim [37] for orienting the end effector when performing simultaneous edge following and force control. (a) Determination of initial orientation with tool off. (b) Re-orientation of tool and start of deburring. (c) Orientation update.

spindle bearing is negligible, the only force will be normal to the edge, as shown (Figure 2.6 (a)). Based on the direction of this force the end effector is re-oriented (Figure 2.6(b)). Deburring is then begun under force control. The orientation is updated at discrete intervals by computing the angle between the current position and one *D* units back (Figure 2.6(c)). Experiments were performed at feedrates of 10-30 mm/s on 6061 aluminum workpieces with straight, concave, and convex edges. The force setpoint was 2.5 N. The radii of curvature ranged from 60 to 120 mm. Steady state errors of +32% (convex edge) and -24% (concave edge) were observed with the curved edges as a result of the limited bandwidth of the system. Similarly, the long delays required to obtain sensor data and execute the control update caused the force to become oscillatory at the higher feedrates. At 30 mm/s, ±1.5 N oscillations were observed.

Starr and Loucks [20] used a PD controller with their deburring system. Although omitting the integration term causes the system to be subject to a steady state error, they chose PD control in order to achieve a faster response than PID. The system is limited to planar parts since it positions the part with an X-Y table, and has the tool rigidly mounted. Prior to on-line control, the part contour is first learnt by stepping around the part and moving towards the edge (with the tool off) until a contact force is sensed. Using a setpoint of 7 N and a feedrate of 1.3 mm/s, one tree of a jet engine turbine hub was deburred to within its specification of 0.5±0.25 mm in 16 seconds. The tree contained several tight corners, with radii of about 1 mm. It was projected that the system can finish the entire hub in 45 minutes, which is over 30 times faster than the manual operation. Prior to this work, Loucks *et al.* [14] used through the arm control with an Adept One robot and a tool guide.

The guide was necessary to prevent gouging when the tool was first fed into the part. This approach was abandoned because a general purpose system would require a large number of different guides.

Impedance control [38] is an alternative to force control which has been applied to robotic deburring. Mechanical impedance is defined as the ratio of contact force to deflection as a function of frequency. With impedance control the robot is commanded so that it maintains a specified impedance. If the robot and environment are taken to be infinitely stiff, and the position servo has a unity transfer function over the frequency range of interest, the position command for impedance control is given by:

$$x = F/(m_e s^2 + c_e s + k_e) \tag{2.9}$$

where m_e is the effective mass, c_e is the effective damping, and k_e is the effective stiffness. In effect the system behaves like a passive end effector whose dynamic behaviour can be easily modified. This approach has the advantage that there is no need to switch from position control to force control at initial tool/part contact. The disadvantage of impedance control is that a force setpoint cannot be specified.

Kazerooni [10, 26, 33, 39] has researched the application of impedance control to robotic deburring for several years. His work extends the work of Kramer *et al.* [2] and Bausch [9] on passive end effectors. With passive designs the impedances in the normal and tangential directions are coupled by the tool mass. With active impedance control the impedances can be freely selected. The method for selecting the impedances is based on the expected frequency range of the burrs and robot oscillations, and is shown in Figure 2.7. In the normal direction the impedance is set so that it is low for the range of robot oscillations and high for the range of burr

frequencies. In this way the transmission of the oscillations to the chamfer surface is reduced, and also the effect of the burrs is filtered out. To prevent large cutting forces from developing if a large burr is encountered, the impedance is set low at the range of burr frequencies in the tangential direction. The impedances must also be selected so that stability is guaranteed. Experiments were performed with the part on an X-Y table and the tool rigidly mounted. On an aluminum straight edged part, with a step change in the chamfer depth to simulate a burr, an average normal force of 2 N, an average depth of 1.1 mm, and an average feedrate of 2.2 mm/s were achieved. This work was later extended by Her and Kazerooni [40] to provide simultaneous edge following and control of material removal for planar parts. The edge following was obtained by controlling the force on a roller bearing adjacent to the edge, while the material removal was controlled using impedance control as before.

A simulation study comparing stiffness type force control (equivalent to proportional control) with impedance control for the AEE approach to deburring was performed by Guvenc and Paul [16]. Impedance control was shown to filter out high frequency disturbances, while stiffness control amplified them. Neither controller reduced low frequency force errors.

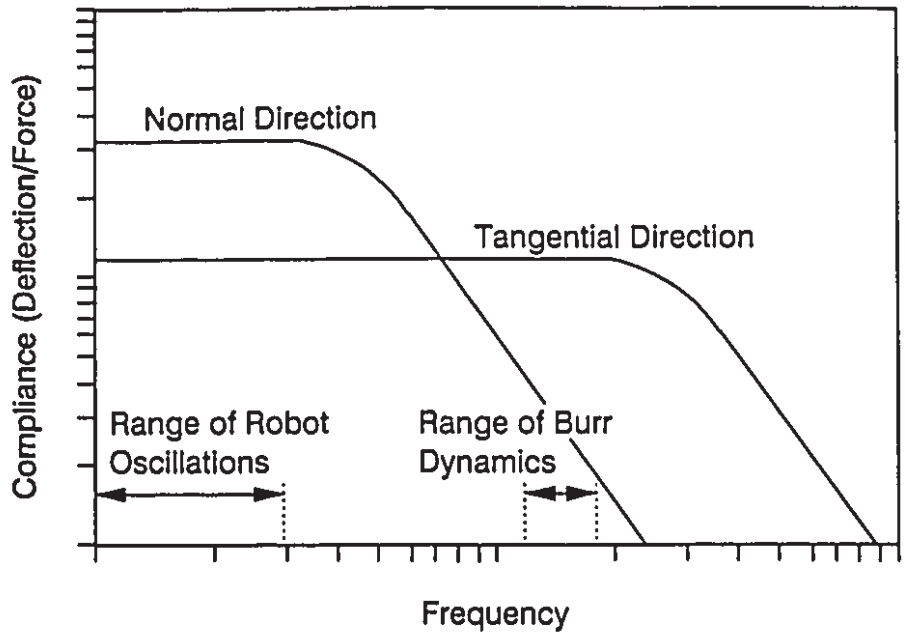

Figure 2.7 Required compliances (inverse of impedance) in the normal and tangential directions for deburring under impedance control (after Kazerooni *et al.* [10])

One limitation of the force control algorithms discussed thus far is that their parameters are fixed. For good performance these schemes require the process dynamics to be relatively time invariant. In practice however the arm's stiffness is known to vary with configuration and the deburring process is affected by changes in cutting conditions and part material. Parameter adaptive control is one potential solution to this problem. With parameter adaptive control the process model is estimated on-line and the control algorithm is updated based on these estimates. This approach is compared to non-adaptive control in Figure 2.8. A simulation study by Bone *et al.* [41] concluded that parameter adaptive control provided significant improvements in control bandwidth and robustness over non-adaptive schemes for deburring. Robust, high bandwidth control is required for deburring complex part

contours at high feedrates. An adaptive Smith predictor and a form of model reference adaptive control were investigated.

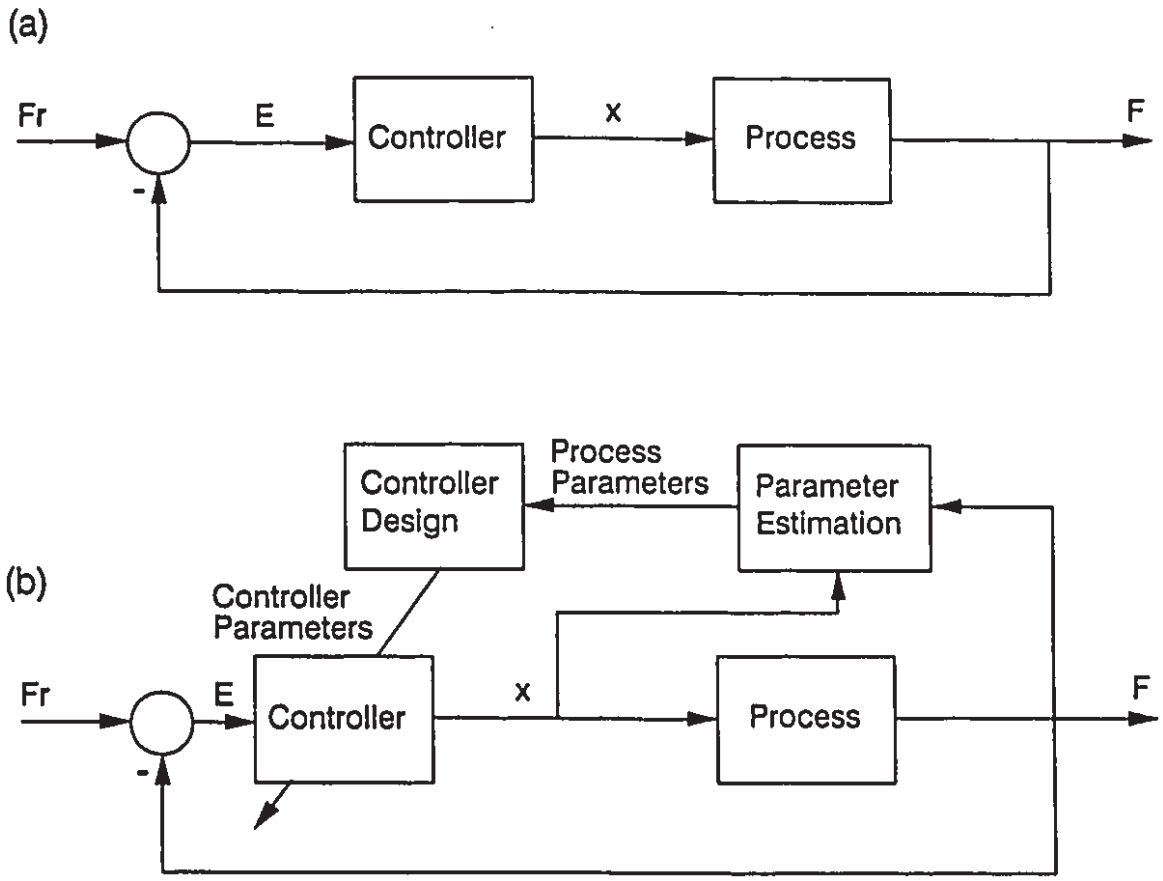

Figure 2.8 Block diagrams for: (a) non-adaptive force control, (b) parameter adaptive force control.

More recently, Duelen *et al.* [15] simulated a force control algorithm for deburring which adapted to changes in the deburring process. The process damping was estimated from the force and joint velocity values. Their results demonstrated greatly improved robustness in comparison to the non-adaptive case. In a subsequent paper [42] they failed to implement the control algorithm, stating that it was too complex.

Liu and Asada [43] have developed an adaptive controller for deburring based on a human skill model. Associative memories were first trained off-line from human demonstration data. On-line process parameter estimates were then used to evoke the appropriate control actions from these memories. In deburring experiments performed on 2014-T6 aluminum, straight edged parts using a direct drive robot, a force of 5±3 N was maintained.

Iterative learning control may be used as an alternative to, or an addition to, adaptive control. Whereas adaptive control adapts during a single repetition of a task, iterative learning control's aim is to improve the performance of a task over a series of repetitions. In many industrial applications, including deburring, a robot's motions are repeated over and over, making robotics an ideal candidate for learning control.

Research in this area began with the independent proposal of the technique by a number of researchers, including Arimoto *et al.* [44], and Craig [45]. When the research reported in this thesis began in 1988 there were no reported applications of learning control to robotic deburring. Very recently, Kobayashi and Kimura [46] reported the development of a learning control algorithm for application to robotic systems in which the feedrate is varied, as is sometimes the case in deburring. The system obtains feedback from the robot's motors, and only corrects for errors at each of the robot's joints. Multiple learning controllers are employed, each one taught at a particular feedrate. Eleven repetitions of the task were required to teach each controller. The correct control action is obtained by interpolating between the stored control actions for the two feedrates nearest to the current feedrate. A cutting experiment was performed on a planar aluminum part with a corner radius of 8 mm,

at an average feedrate of 90 mm/s. When the learning controller was applied the maximum position error during the cut was reduced from 2 mm to 0.5 mm. This error is still very large for the deburring application.

CHAPTER 3

ACTIVE END EFFECTOR DESIGN

3.1 INTRODUCTION

In this chapter the design objectives for the Active End Effector (AEE) are obtained from a dynamic analysis of the combined robot arm, end effector, and deburring process dynamics. The AEE is then designed, built, and performance tested [47].

3.2 DYNAMIC ANALYSIS

To determine the effect of the AEE design parameters, a dynamic model of the robotic deburring system was developed. Since the position corrections will be performed in the normal direction only, a one dimensional model was used. The model structure includes the robot arm, AEE, and deburring process dynamics, as shown in Figure 3.1. The robot is a Unimation PUMA-560, six-axis, industrial robot.

The robot is modeled as an actuator linked to the wrist by a two Degree-Of-Freedom (DOF) spring-mass-damper model of the arm dynamics. The arm parameters were obtained through modal testing, and are as follows: m_1=49.3 kg, m_2=0.982 kg, k_1=630 N/mm, k_2=14.7 N/mm, c_1=0.556 N/mm/s, and c_2=0.0113 N/mm/s [11].

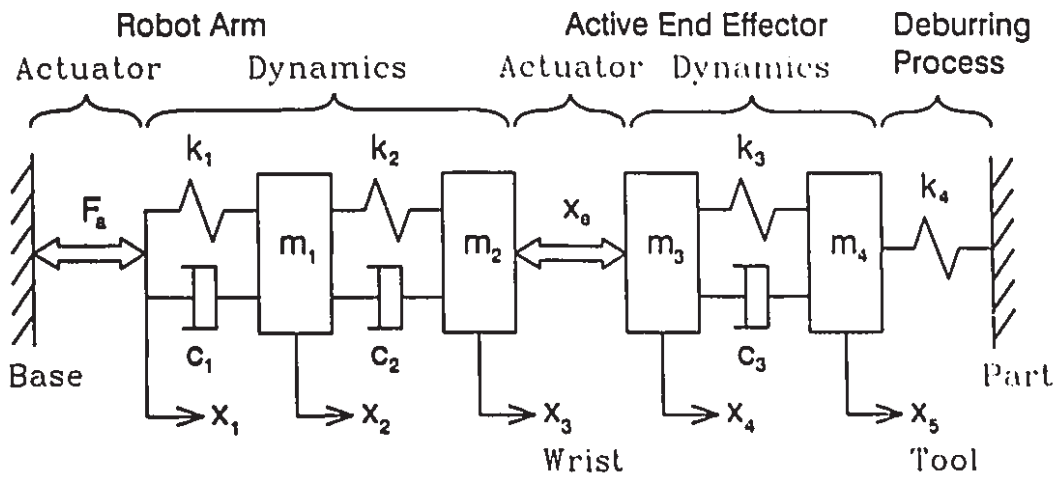

Figure 3.1 Structure of the model used for the dynamic analysis.

The AEE model consists of an actuator coupled to the cutting tool (mass m_4) by a single DOF spring-mass-damper model. This includes the combined flexibility of the drive components and force sensor. The actuator produces a relative motion x_e between the wrist position x_3, and position x_4. The actuator response is modeled as a critically damped second order system:

$$\frac{x_e}{x} = \frac{1}{[(0.65/\omega_b)s+1]^2} \tag{3.1}$$

where x_e is the actuator response, x is the AEE position command, and ω_b is the actuator bandwidth in rad/s.

The cutting process is modeled as a spring between the chamfer depth (equivalent to the tool position x_5 in the model) and the force. Although the spring is actually nonlinear in that the force is zero for negative depths of cut, it will be taken to be linear here, since the main concern is force regulation and not the initial transient upon cut entry. The cutting force is related to the tool position by:

$$\frac{F_c}{x_5} = G_c(s) = k_4 \tag{3.2}$$

where F_c is the cutting force. Based on cutting tests performed with the tool rigidly mounted on a milling machine, k_4=8.18 N/mm for mild steel workpieces cut with a feedrate of 25 mm/s.

The force sensor should be located as close as possible to the point of application of the force. In practice the sensor will be located between the tool and the AEE actuator, giving:

$$\frac{F_s}{x_5} = G_s(s) = k_4 + m_4 s^2 \tag{3.3}$$

where F_s is the sensed force. The additional $m_4\ddot{x}_5$ term in equation 3.3 is due to the tool's acceleration. While this component has been observed previously [48], it has not been theoretically studied.

For digital implementation the sensed force will be low pass filtered prior to sampling. The analog prefilter was modeled as a third order Butterworth filter, to give:

$$\frac{F}{x_5} = G_m(s) = \frac{k_4 + m_4 s^2}{\phi_3 s^3 + \phi_2 s^2 + \phi_1 s + 1} \tag{3.4}$$

where: F is the measured force, and ϕ_i are the filter coefficients. In this study a 20 Hz cutoff frequency was assumed.

The effect of the AEE design parameters: m_3, m_4, k_3, c_3, and ω_b, was examined via the frequency response of the uncompensated open-loop system. The design objective was to approach the ideal response of unity gain and zero phase lag

over an infinite frequency range. The uncompensated open-loop transfer function between the chamfer depth and the position command is:

$$\frac{x_5}{x} = G_p(s) = \frac{G_1(s)}{G_2(s)} \tag{3.5}$$

where $G_1(s) = (k_3 + c_3 s)[(m_1 s^2 + c_{12} s + k_{12})(m_2 s^2 + c_{12} s + k_2) - (k_2 + c_2 s)^2]$,

$G_2(s) = [(0.65/\omega_b)s + 1]^2 [(m_1 s^2 + c_{12} s + k_{12})(m_4 s^2 + c_3 s + k_{34})(m_{23} s^2 + c_{23} s + k_{23}) -$

$(k_2 + c_2 s)^2 (m_4 s^2 + c_3 s + k_{34}) - (k_3 + c_3 s)^2 (m_1 s^2 + c_{12} s + k_{12})]$, and α_{nm} denotes the sum $\alpha_n + \alpha_m$.

The parameter choice was subject to the following practical constraints:

1. Masses m_3 and m_4 must total less than the robot's dynamic payload capacity of about 4 kg. At the same time the actuator and cutting tool must be sufficiently powerful for the deburring operation.
2. The relative damping will be limited to about 10% unless mechanical dampers are added.

The test case parameters are listed in Table 3.1. The corresponding normalized frequency response curves are given in Figure 3.2. The frequency response of the reference curve (case B, Figure 3.2(a)) exhibited modes at 85.0 rad/s (13.5 Hz) and 116.2 rad/s (18.5 Hz), due to the robot dynamics, followed by a third mode at 276.8 rad/s (44.0 Hz) due to the AEE. The main findings of the study can be summarized as follows:

1. Increasing the actuator bandwidth lessens the overall phase shift (Figure 3.2(a)).
2. Reduction of either m_3 or m_4 reduces the resonance magnitude and increases the natural frequency of the 1st and 2nd modes. Reduction of m_4 has the

additional benefit of reducing the resonance magnitude of the third mode (Figure 3.2(b)).

3. Increasing the end-effector stiffness increased the natural frequency and reduced the resonance magnitude of the third mode. Increasing the damping also decreased the resonance of the third mode. Both parameters had a negligible effect on the first two modes (Figure 3.2(c)).

4. The sensed force corresponds to the cutting force at frequencies below $\omega_a = (k_4/m_4)^{1/2} = 91.2$ rad/s. At ω_a the acceleration component greatly attenuated the sensed force, while at frequencies greater than ω_a the sensed force was amplified with relation to the cutting force. The acceleration component also produced a $+180°$ phase shift at ω_a. The addition of the analog prefilter was beneficial in reducing both the phase shift and magnitude distortion effects of the acceleration force (Figure 3.2(d)).

Based on these findings the AEE design objectives in order of importance are:

1. Minimize the tool mass, m_4,
2. Minimize the base mass, m_3,
3. Maximize the actuator bandwidth, ω_b,
4. Maximize the AEE stiffness, k_3, and
5. Maximize the AEE damping, c_3.

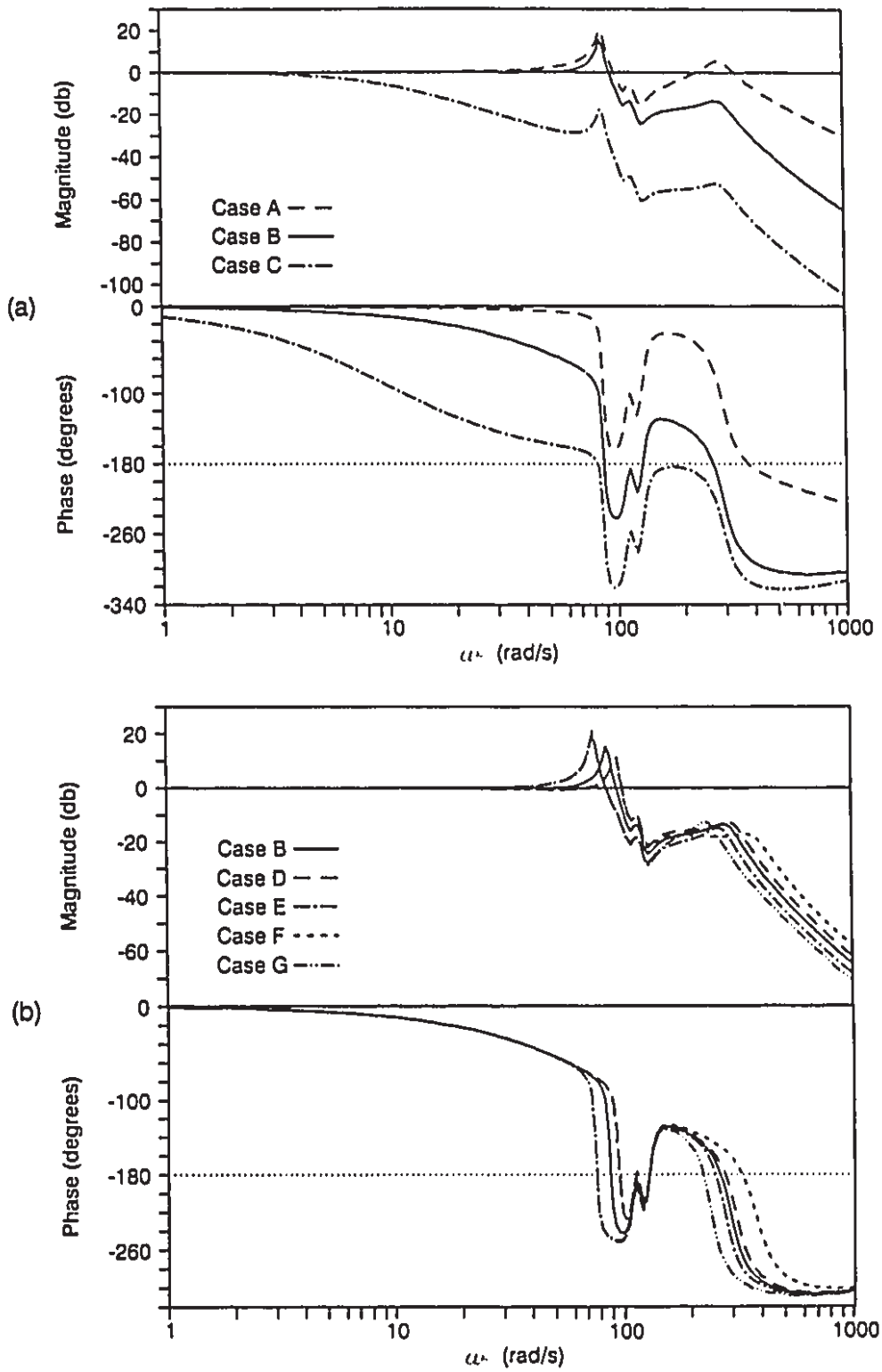

Figure 3.2a Effect of the AEE design parameters on the normalized frequency response of the dynamic model. (a) Bandwidth, ω_b. (b) Masses m_3 , and m_4.

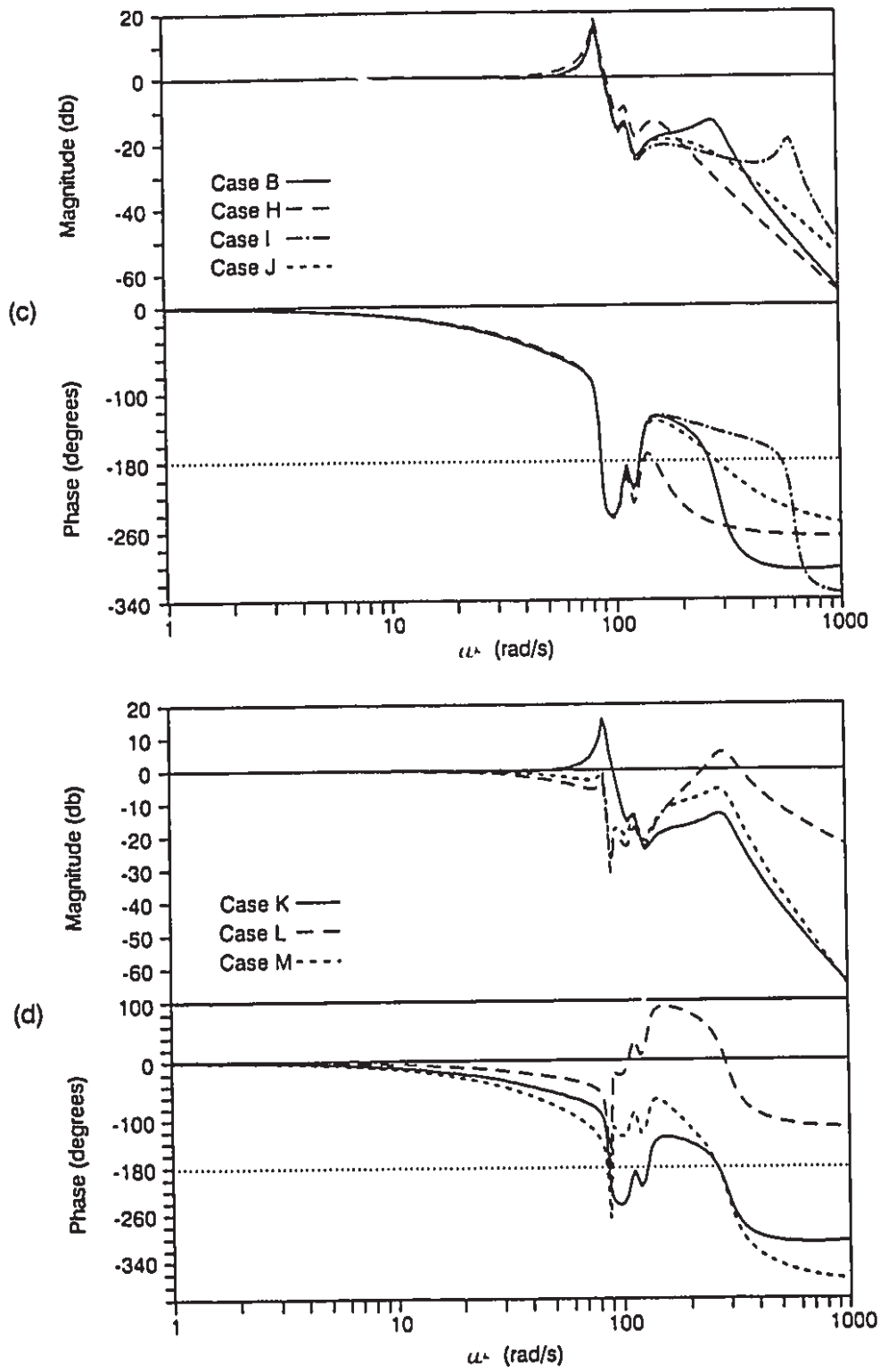

Figure 3.2b Effect of the AEE design parameters on the normalized frequency response of the dynamic model. (c) Stiffness k_3 , and damping c_3. (d) Acceleration force component.

Test Case	Transfer function $f(s)$	Bandwidth ω_b (rad/s)	Mass m_3 (kg)	Mass m_4 (kg)	Stiffness k_3 (N/mm)	Damping c_3 (N/mm/s)
A	G_p	6.3	1.0	1.0	50.0	0.045
B	G_p	62.8	1.0	1.0	50.0	0.045
C	G_p	62.8	1.0	1.0	50.0	0.045
D	G_p	62.8	0.5	1.0	50.0	0.045
E	G_p	62.8	2.0	1.0	50.0	0.045
F	G_p	62.8	1.0	0.5	50.0	0.045
G	G_p	62.8	1.0	2.0	50.0	0.045
H	G_p	62.8	1.0	1.0	10.0	0.045
I	G_p	62.8	1.0	1.0	250.0	0.045
J	G_p	62.8	1.0	1.0	50.0	0.225
K	G_pG_c	62.8	1.0	1.0	50.0	0.045
L	G_pG_s	62.8	1.0	1.0	50.0	0.045
M	G_pG_m	62.8	1.0	1.0	50.0	0.045

Table 3.1 Test case parameters used for the dynamic analysis.

3.3 DESIGN

The new AEE design was derived from the design of the old AEE used in previous research [11]. The old design has two orthogonal motion axes, each driven by a linear ball screw and D.C. servo motor. Lightweight, high torque, servo motors from Galil Motion Control (model 5/500) with 2000 count/rev encoders are used. A Galil DMC-420-10 motion controller is used for the servo control. The ball screws (THK model MBF0401) have a lead of 1 mm which gives the system a theoretical accuracy of 0.0005 mm. THK linear ball slides (model RSR15UU) are used to guide

the motion axes. The manufactured parts were machined from 6061-T6 aluminum for high strength with low mass. The deburring tool is a carbide rotary file (Grobet, 9.5 mm dia.) driven by a Dotco pneumatic grinder (model 10B2000C-01, 20 kRPM, 0.57 kg). A small three axis piezoelectric sensor by Kistler (model 9251A) is used to measure the cutting forces. The sensor's output is amplified by Kistler model 5004 charge amplifiers.

The new AEE design is shown in Figure 3.3. In accordance with the first design objective the new design uses a Dotco 10L1082-36, 20 kRPM, 0.36 kg, grinder to drive the deburring tool, for a 0.21 kg mass reduction. The base mass was reduced by changing to a single motion axis design. This modification was possible because the position corrections will be performed in the normal direction only. With the old design both normal and tangential corrections could be performed.

The actuator bandwidth was increased by modifying the servo amplifier. Two modifications were performed. The current limiting circuitry was bypassed, increasing the peak current available from 2.5 to 5 A. To take advantage of this additional current, the gain of the amplifier was increased from 0.2 to 0.6 A/V. These modifications increased the bandwidth from 20 to 65 Hz. The bandwidth tests are described in the next section.

To increase the AEE stiffness the ball slide was replaced with a THK model HSR15CR. This unit has a 430% greater moment load rating, and 206% greater force load rating than the old slide. Its disadvantage is that it increases the base mass by 0.11 kg.

The motor, motion controller, ball screw, and force sensor are unchanged from the previous design. The system has a ±10 mm range of motion. The force sensor calibration procedure and results are given in Appendix A. The new design

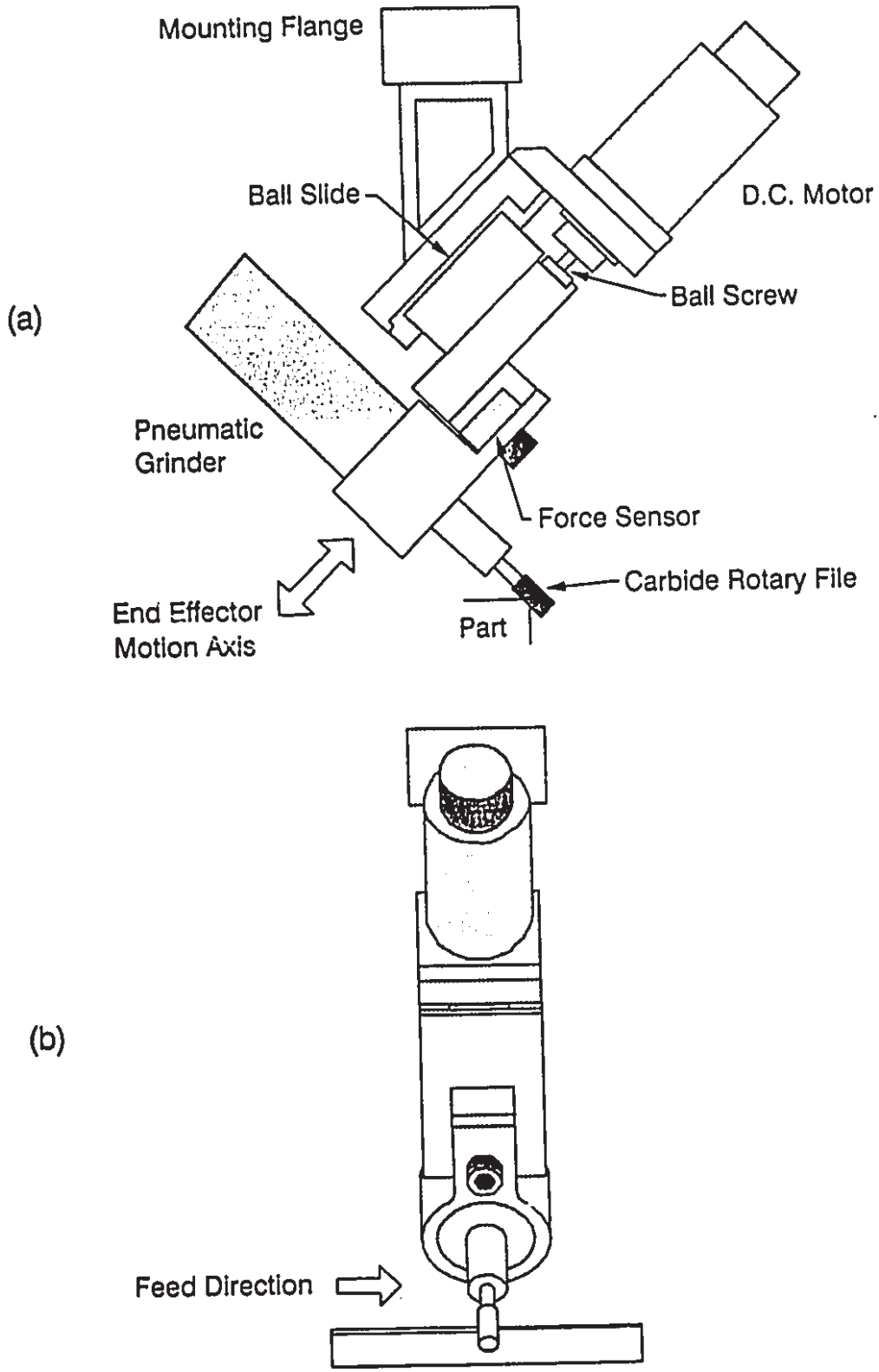

Figure 3.3 The new AEE design. (a) Side view. (b) Front view.

also incorporates a vision sensor for on-line control and inspection, whose development is detailed in Chapter 5. The total mass of the AEE is 2.0 kg without the vision sensor, and 3.0 kg with the vision sensor.

3.4 PERFORMANCE TESTING

The positioning accuracy, bandwidth, and structural dynamics of the AEE were tested experimentally. The AEE's accuracy and repeatability were determined to be at least as good as 0.01 mm over a 1 mm range, based on dial gauge measurements [11].

The AEE's servo loop was tuned based on its step input response. The motion controller's software gains were adjusted until a response with minimal risetime, minimal overshoot, and no steady state error was achieved. Step responses for 0.1 and 0.2 mm position commands are shown in Figure 3.4. The slightly longer risetime for the 0.2 mm response was due to amplifier saturation.

The servo loop's frequency response was obtained by commanding a sinusoidal input with a 0.05 mm amplitude at frequencies of 1, 5, 10, ..., 100 Hz. The amplitude of the response was measured at each frequency using a proximity sensor sampled at 2 kHz. The frequency response is shown in Figure 3.5. Based on this response the servo loop's bandwidth is about 65 Hz.

The structural dynamics of the AEE were identified using an HP 3566A Spectrum Analyzer. The structure was excited near the tool tip (as close as possible to the point of application of the cutting force) by a force sensor tipped hammer (Kistler model 9726A-20000), while the response was measured with an accelerometer (PCB model 308B). The position transfer function was obtained by dividing the acceleration measurement by $j\omega$ twice. The direct transfer function of the

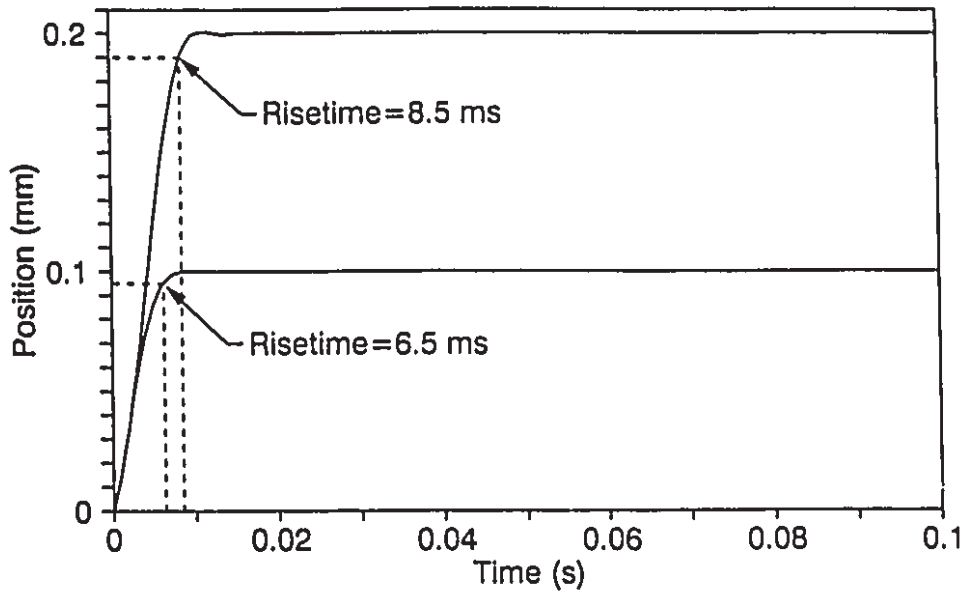

Figure 3.4 AEE step input responses for 0.1 mm and 0.2 mm position commands.

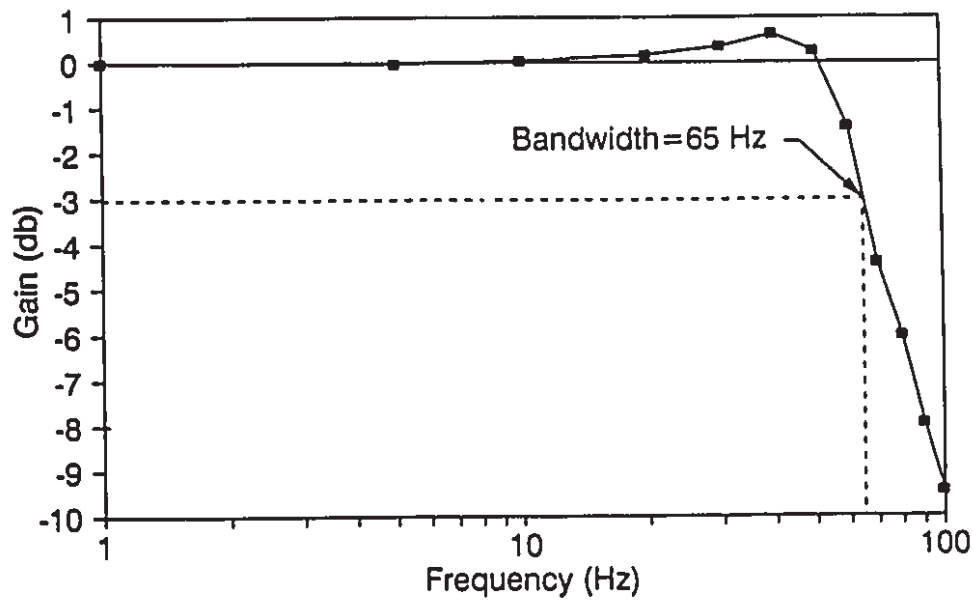

Figure 3.5 AEE frequency response for a position command amplitude of 0.05 mm.

AEE without the vision sensor attached is shown in Figure 3.6. The response shows two structural modes at 75 and 97 Hz. Of these, the 2nd mode at 97 Hz is dominant. This is a significant improvement over the response of the old AEE whose 1st mode at 33 Hz was dominant. This indicates that the ratio of stiffness to mass in the new design is 8.6 times larger than with the old design. When the vision sensor was added the additional mass lowered the frequency of both modes to 55 and 74 Hz respectively, and caused the 1st mode to be dominant. The direct transfer function is shown in Figure 3.7. In this case the stiffness to mass ratio was 2.8 times larger than with the old design.

3.5 CONCLUSIONS

The design for the new AEE was obtained by modifying the previous design, based on the conclusions drawn from a dynamic analysis of the robotic deburring system. The dynamic model included the robot arm, AEE, and deburring process dynamics. The analysis concluded that minimizing the AEE's tool mass has the most beneficial effect, followed by minimizing the AEE's base mass, maximizing the actuator bandwidth, and maximizing the AEE's stiffness. The new design incorporates a lighter tool, a single (rather than double) motion axis to reduce the base mass, and a stiffer ball slide. The actuator bandwidth was increased from 20 to 65 Hz by modifying the servo amplifier. Based on dial gauge measurements the AEE's positioning accuracy and repeatability are at least as good as 0.01 mm. The new AEE also incorporates a vision sensor whose design is detailed in Chapter 5. Based on transfer function measurements the stiffness to mass ratio for the new AEE was 8.6 times greater without the vision sensor attached, and 2.8 times greater with the vision sensor attached, than the old AEE.

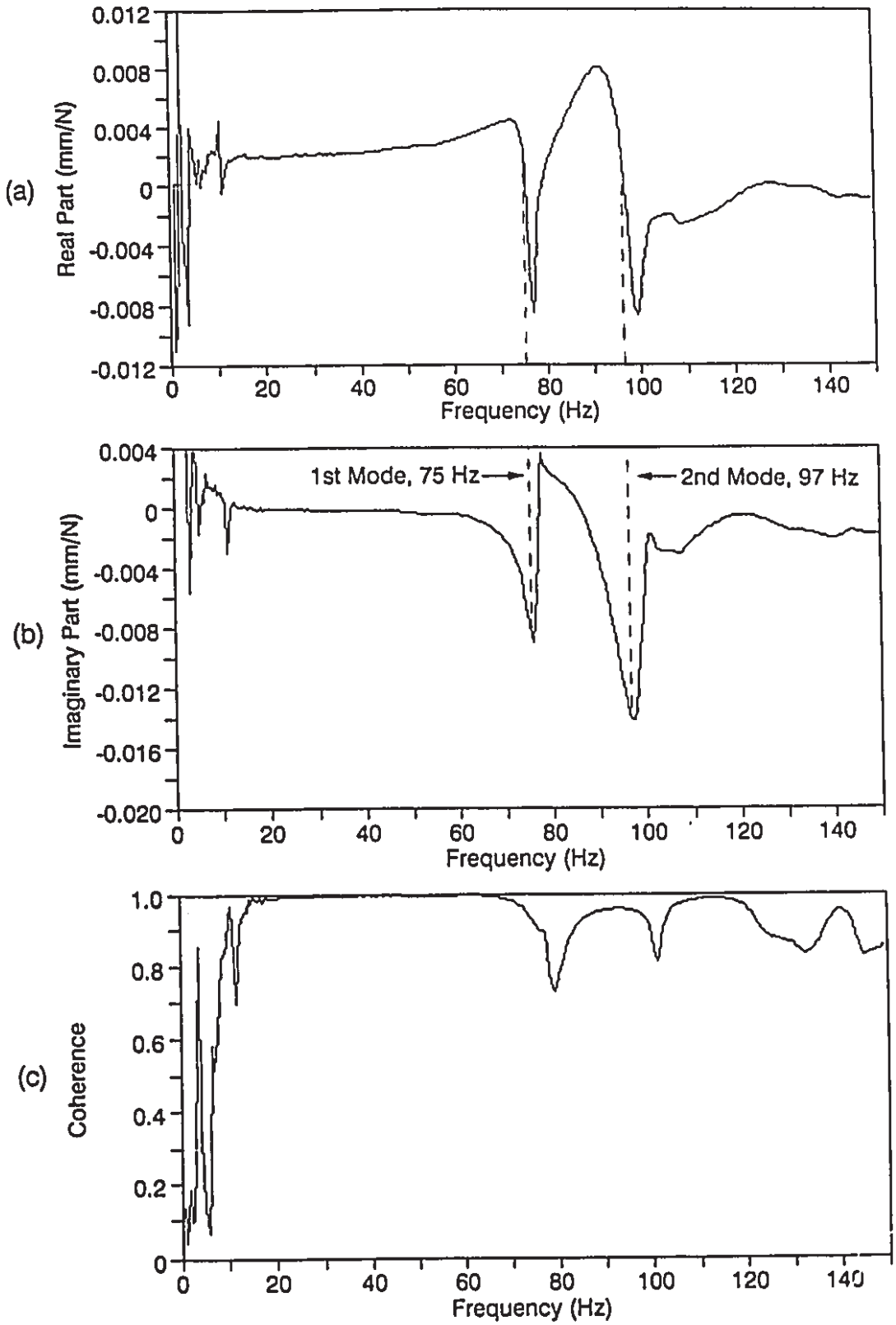

Figure 3.6 Direct transfer function for the AEE without the vision sensor. (a) Real part. (b) Imaginary Part. (c) Coherence.

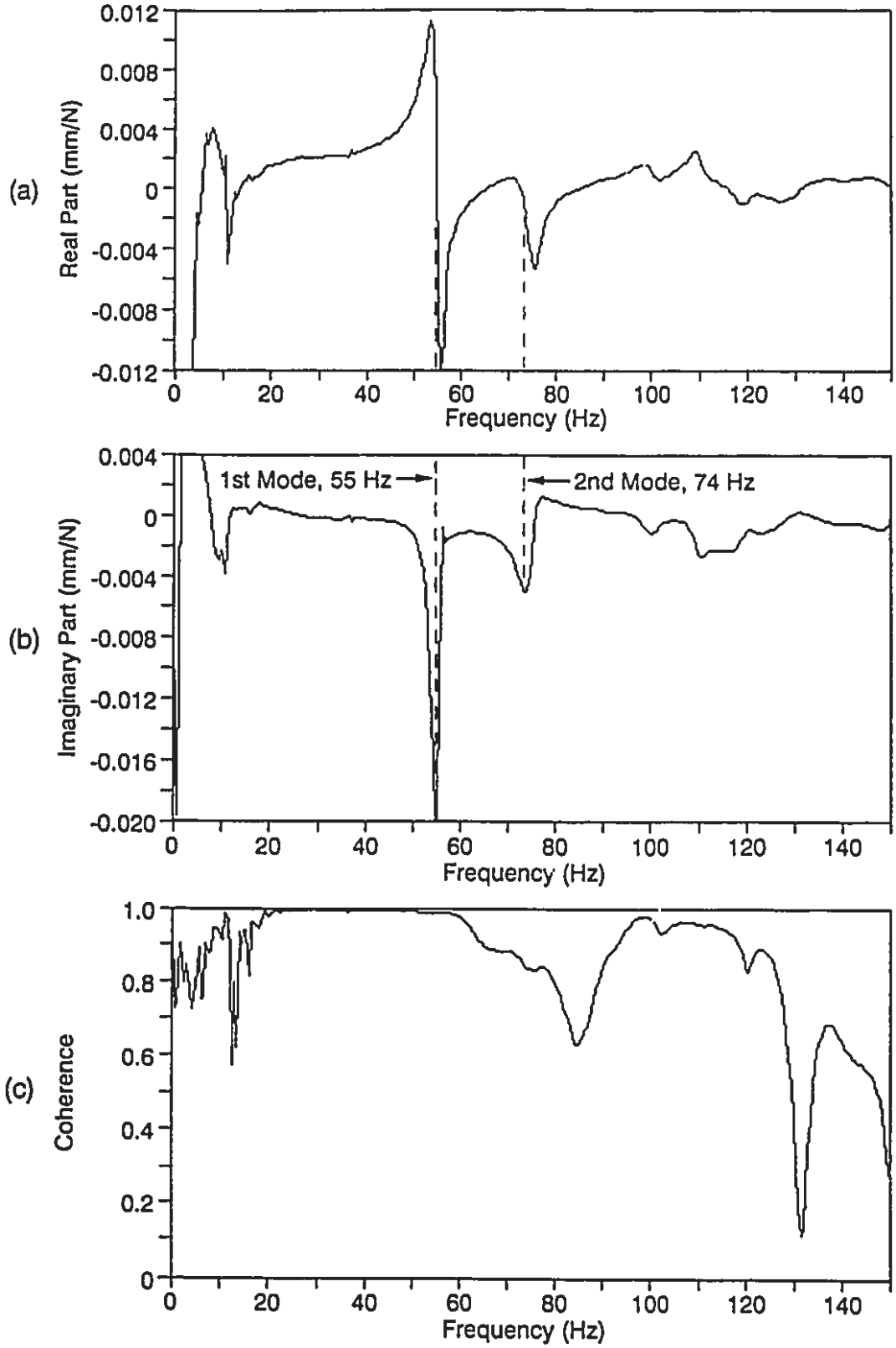

Figure 3.7 Direct transfer function for the AEE with the vision sensor. (a) Real part. (b) Imaginary Part. (c) Coherence.

CHAPTER 4

FORCE CONTROL

4.1 INTRODUCTION

As discussed in Chapter 2, control of the normal deburring force is the most common method used to indirectly control the chamfer depth. In this chapter several parameter adaptive and non-adaptive force control algorithms are investigated [41, 49]. The algorithms' performance are compared based on the results of computer simulations and deburring experiments.

4.2 PROCESS MODELLING

The structure of the force control system is shown in Figure 4.1. The controller sends a position command, x, to the end effector servo based on the normal force error, E. The end effector then performs corrections to the robot's path in order to control the depth of cut. The robot's path includes positioning errors due to both the robot's motion and to inaccurate part fixturing. In previous tests of the PUMA-560 robot, static errors up to 2 mm, and dynamic errors with an amplitude of 0.15 mm, were measured [11]. The path corrections must also compensate for deflections of the robot arm and end effector due to the cutting force. As in the dynamic model used in the previous chapter, the process dynamics includes the robot arm, end effector and deburring process dynamics.

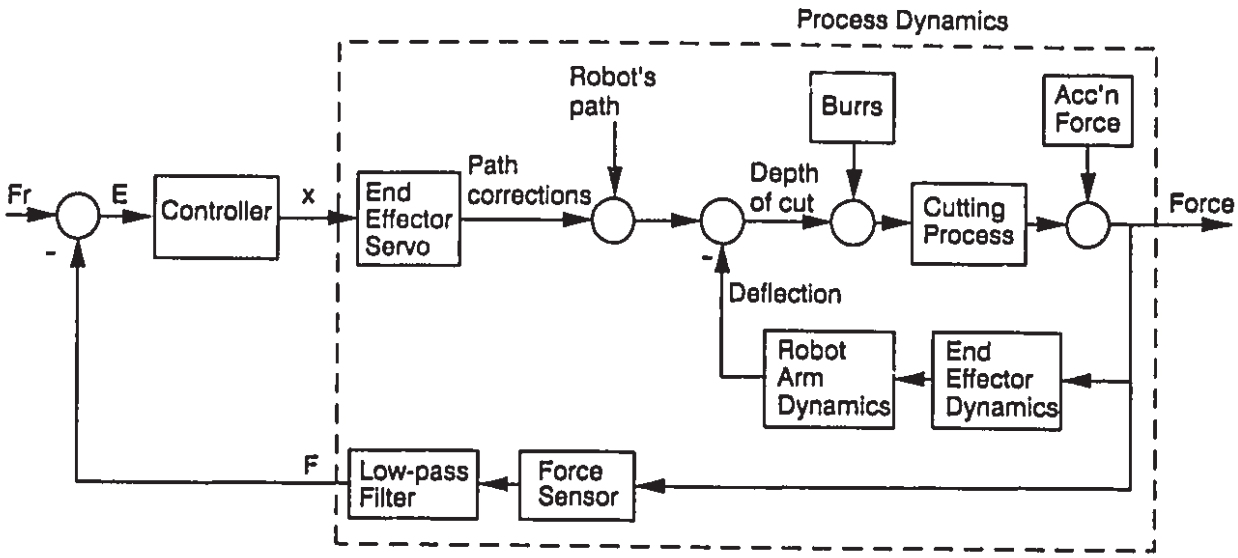

Figure 4.1 Structure of the force control system.

The process modelling data was obtained under open-loop conditions, by commanding the end effector to follow a Pseudo-Random Binary Signal (PRBS) while simultaneously measuring the force during a cut. The tests were performed using the PUMA-560 robot equiped with the old AEE. Low-carbon steel workpieces with straight burred edges, and a feedrate of 25 mm/s, were used. The force signal was low-pass filtered at 10 Hz prior to sampling at 50 Hz. A general-purpose time series model combining a deterministic transfer function between the position command and output force with a non-stationary stochastic disturbance, known as a Controlled Auto-Regressive Integrated Moving-Average (CARIMA) model, was used:

$$A(q^{-1})F(t) = B(q^{-1})x(t-k) + C(q^{-1})\xi(t)/\Delta \tag{4.1}$$

where $A(q^{-1}) = 1 + a_1 q^{-1} + \ldots + a_{na} q^{-na}$, $B(q^{-1}) = b_0 + b_1 q^{-1} + \ldots + b_{nb} q^{-nb}$, $C(q^{-1}) = 1 + c_1 q^{-1} + \ldots + c_{nc} q^{-nc}$, $F(t)$ is the normal force measurement, $x(t-k)$ is the end effector position command, k is the deadtime, $\{\xi(t)\}$ is a zero mean uncorrelated random sequence, and $\Delta = 1 - q^{-1}$ is the differencing operator. Using least squares parameter

estimation a model structure with: $na=4$, $nb=3$, $nc=0$ and $k=3$, was selected. For PRBS amplitudes of: (a) 0.1 mm, (b) 0.15 mm and (c) 0.2 mm, the following model parameters where obtained:

(a) $a_1=-1.5654$, $a_2=1.0207$, $a_3=-0.1798$, $a_4=-0.0204$, $b_0=0.2765$, $b_1=0.6441$, $b_2=0.6907$, $b_3=0.3409$, and $V=0.00223$ N^2.

(b) $a_1=-1.6959$, $a_2=1.7221$, $a_3=-0.9353$, $a_4=0.2337$, $b_0=0.2537$, $b_1=0.6692$, $b_2=0.6800$, $b_3=0.2885$, and $V=0.00447$ N^2.

(c) $a_1=-1.8031$, $a_2=1.6790$, $a_3=-0.7493$, $a_4=0.1676$, $b_0=0.2033$, $b_1=0.4527$, $b_2=0.5486$, $b_3=0.2529$, and $V=0.00437$ N^2.

V is the estimated variance of $\xi(t)$. The average change in parameters relative to case (b), is 32% for case (a) and 18% for case (c). Considering the 33% change in input amplitude, these variations represent significant nonlinearities in the process. The importance of these models to the controller design is discussed in the following section.

4.3 NON-ADAPTIVE CONTROL: DESIGN AND SIMULATION

4.3.1 Introduction

A simulation was written in C to allow fast and safe testing of the force control algorithms. The controllers are designed based on the 0.15 mm PRBS model. The effect of model mismatch (i.e. errors between the model and the real process) is studied by changing the simulated process dynamics from the 0.15 mm PRBS model to either of the 0.1 and 0.2 mm PRBS models. An insensitivity to this mismatch is important for reliable real-time performance of the controller. The final controller tunings are a compromise between this requirement for robustness and the

main objective of minimizing the force variance.

4.3.2 Linear-Quadratic-Gaussian Control

The design objective of Linear-Quadratic-Gaussian (LGQ) control is to minimize the variance of the process's output subject to a constraint on the input variance [50]. In this application the normal force variance is minimized subject to a constriant on the position command variance:

$$J = \mathrm{E}\{E^2(t+k) + \lambda \Delta x^2(t)\} \tag{4.2}$$

$$E(t) = F_r(t) - F(t) \tag{4.3}$$

where J is the cost-function to be minimized, $\mathrm{E}\{\}$ is the expected value, $E(t)$ is force error, λ is the constraint factor, and $F_r(t)$ is the reference force.

The solution requires the spectral factorization of the discrete Wiener-Hopf equation:

$$B(q^{-1})B(q) + \lambda \Delta A(q^{-1})A(q)\Delta = \gamma(q^{-1})\gamma(q) \tag{4.4}$$

The resulting polynomial $\gamma(q)$ is used to solve the Diophantine equation:

$$B(q)q^k = T_1(q^{-1})\gamma(q) + T_2(q)A(q^{-1})\Delta \tag{4.5}$$

The control law is then given by:

$$[\gamma(q^{-1}) + T_1(q^{-1})B(q^{-1})q^{-k}]x(t) = A(q^{-1})T_1(q^{-1})E(t) \tag{4.6}$$

The effect of the constraint factor, λ, on the force and command variances is shown in Figure 4.2. When $\lambda < 0.05$ the minimum force variance is achieved, at the cost of a very large command variance. Since a large command variance tends to excite system nonlinearities, and wear out the end effector actuator, this situation is undesirable. When λ is increased from 0.01 to 0.2, a 500 fold decrease in the command variance is realised for an 11% increase in the force variance. However with $\lambda = 0.2$ the robustness to model mismatch was poor. With $\lambda = 0.6$ the best

compromise between robustness and force variance was achieved. The simulated force response for a 5 N reference force is shown in Figure 4.3. The remaining force variance of 0.099 N^2 is due to incomplete removal of the stochastic disturbance.

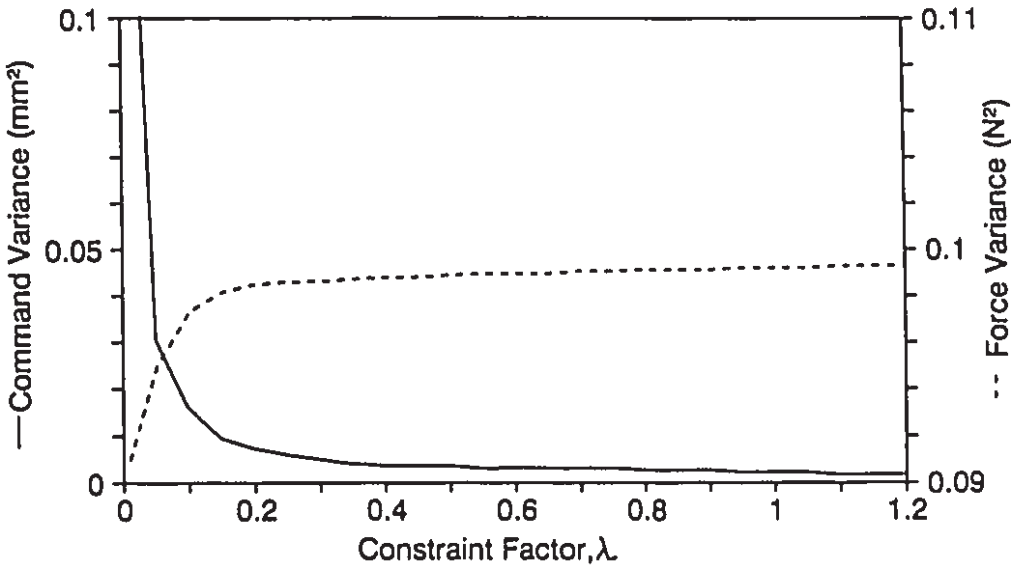

Figure 4.2 Force and command variance for LQG control as a function of λ.

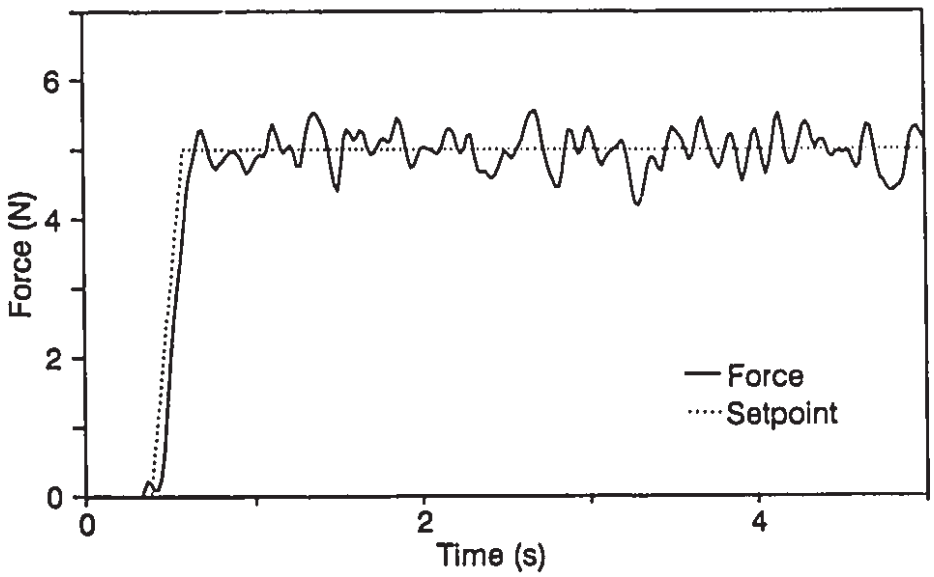

Figure 4.3 Simulated force response for LQG control.

4.3.3 Generalized Minimum-Variance Control

The Generalized Minimum-Variance (GMV) [50] design is related to LQG control, with the cost function simplified to:

$$J=\hat{E}(t+k\,|\,t)+\rho\Delta x(t) \tag{4.7}$$

The design is a one-step optimization which does not take into account the effect the present position command will have on future errors at lead times greater than k (the process model's deadtime). In theory this should result in a poorer performance in comparison to the LQG design. The advantage of GMV is that its simplified design calculations make it better suited for use in real-time adaptive control.

The control law is given by:

$$1=L(q^{-1})q^{-d}+\psi(q^{-1})A(q^{-1})\Delta \tag{4.8}$$

$$[\Delta B(q^{-1})A(q^{-1})\psi(q^{-1})+\rho\Delta A(q^{-1})/b_0]x(t)=A(q^{-1})L(q^{-1})E(t) \tag{4.9}$$

The best combination of low force variance with robustness was achieved with $\rho=4.5$. The simulated force response is shown in Figure 4.4. As predicted, the force variance of 0.126 N^2 was 26% greater than achieved with the LQG design.

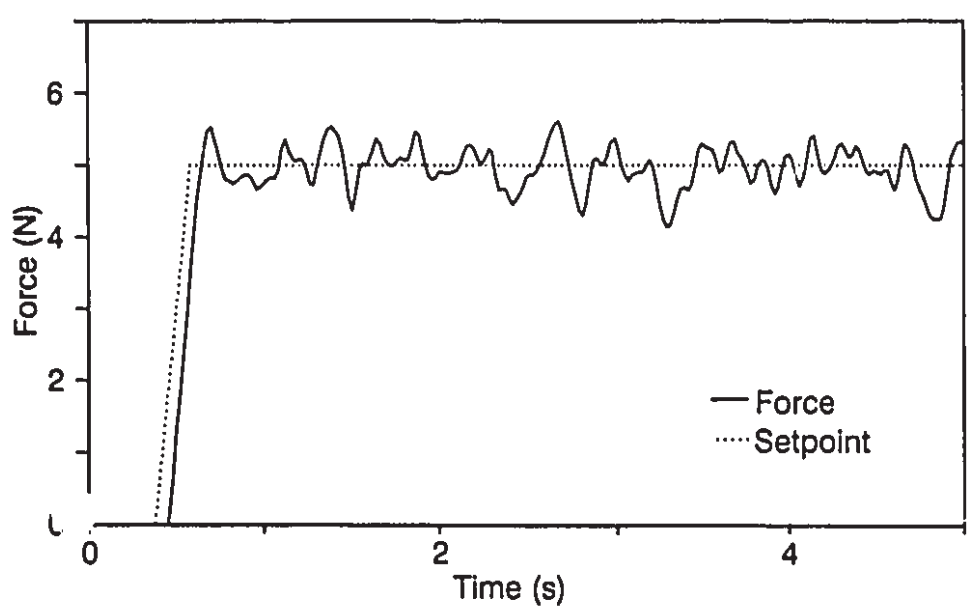

Figure 4.4 Simulated force response for GMV control.

4.3.4 Extended Horizon Control

The Extended Horizon (EH) controller [51] is a predictive controller, whose design objective is to bring the force to the setpoint at the control horizon with minimum effort. In equation form:

$$E\{F_r(t+h)-F(t+h)\}=0 \qquad h>k \tag{4.10}$$

$$J=\sum_{i=0}^{h-k}\Delta x^2(t+i) \tag{4.11}$$

The prediction model is given by:

$$\hat{F}(t+h\,|\,t)=[1+H(q^{-1})\Delta]F(t)+G(q^{-1})B(q^{-1})\Delta x(t+h-k) \tag{4.12}$$

$$1-q^{-h}=A(q^{-1})G(q^{-1})\Delta+q^{-h}H(q^{-1})\Delta \tag{4.13}$$

The control law is then:

$$\Delta x(t)=K[F_r(t+h)-\hat{F}(t+h\,|\,t)] \tag{4.14}$$

where $K=\beta_h/\sum_{i=0}^{h}\beta_i^2$ and (4.15)

$$\beta(q^{-1})=G(q^{-1})B(q^{-1}). \tag{4.16}$$

The controller is tuned through selection of the control horizon, h. With h=6, a robust response with a force variance of 0.109 N^2 was achieved. The simulated normal force is shown in Figure 4.5.

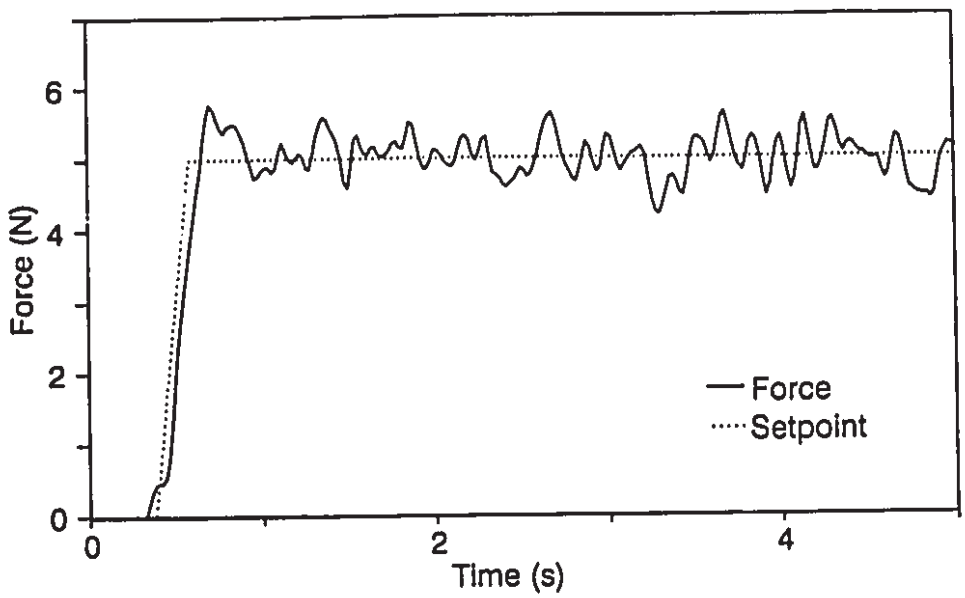

Figure 4.5 Simulated force response for EH control.

4.3.5 Extended PID Control

The conventional discretized form of PID control is [52]:

$$x(t) = [K_p + (K_i T q^{-1}/\Delta) + (K_d \Delta/T)]E(t) \tag{4.17}$$

where K_p is the proportional gain, K_i is the integral gain, K_d is the derivative gain, and T is the sampling interval. This can be rewritten in the form:

$$\Delta x(t) = (r_0 + r_1 q^{-1} + r_2 q^{-2})E(t) \tag{4.18}$$

where $r_{0\text{-}2}$ are the controller coefficients. This controller is standardly used to control a second order process. With the Extended PID (EPID) algorithm the numerator polynomial's order is increased from 2 to *na*, where *na* is the order of the model polynomial, A.

$$\Delta x(t) = R(q^{-1})E(t) \tag{4.19}$$

where $R(q^{-1}) = r_0 + r_1 q^{-1} + \ldots + r_{na} q^{-na}$. Using Isermann's [53] approach the parameters are derived from the process model as follows:

$$r_0 = K_c / \sum_{i=0}^{nb} b_i \tag{4.20}$$

$$r_i = r_0 a_i \quad \forall i \mid 1 \le i \le na \tag{4.21}$$

The tuned force response with $K_c = 0.13$ is shown in Figure 4.6. The EPID's performance , with a force variance of 0.128 N^2 , was very close to that achieved by the GMV design.

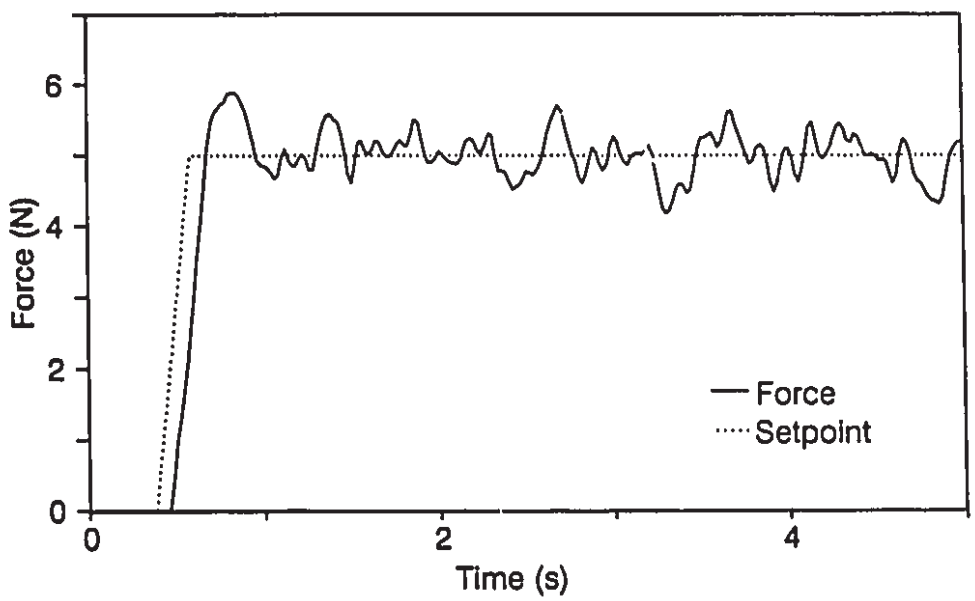

Figure 4.6 Simulated force response for EPID control.

4.4 EXPERIMENTAL VERIFICATION

The experiments were performed using the same equipment and settings as used in the process modelling tests.

A comparison of the simulated and experimental force and position command variances, along with the surface roughness produced by each of the control algorithms is given in Figure 4.7. The experimental results were averaged over 5 cutting tests. The experimental force variance of the EH and EPID controllers was

on average 27% smaller than predicted by the simulations with model mismatch, and only 4% larger than the results with no model mismatch. This suggests that the dynamics of the real process were well modelled by the 0.15 mm PRBS, CARIMA model. In contrast, the LQG design's average experimental force variance of 0.168 N^2 was 54% greater than predicted by the simulation with model mismatch. This was most likely due to the LQG's large command variance exciting process nonlinearities, which produced a greater mismatch than used in the simulation, and resulted in poorer performance. A typical experimental force response is shown in Figure 4.8. Increasing the LQG constraint factor, λ, could have resulted in improved performance. The excellent experimental performance of the EH design, which minimizes the command variance (over the specified control horizon), validates this observation.

The EH design achieved an average experimental force variance of 0.110 N^2, the smallest of the experimental results, and only 1% larger than predicted by the simulation. A typical experimental result is shown in Figure 4.9. This low variance produced the smoothest chamfer, with an average surface roughness of 9.5 μm (measured according to the International Standards Organization, Roughness Average).

An examination of the GMV, EH and EPID results (Figure 4.7), suggests that the normal force variance was a reasonable measure of the chamfer surface roughness. However, with the LQG design a rougher surface was produced than the force variance would suggest, possibly due to the LQG's large command variance. Measurements of the chamfer depth under closed and open-loop conditions suggested that all of the controllers had a beneficial effect. With force control the

depth remained fairly constant at 0.68 mm, while in the open-loop it varied from 0.23-0.57 mm along the length of the cut.

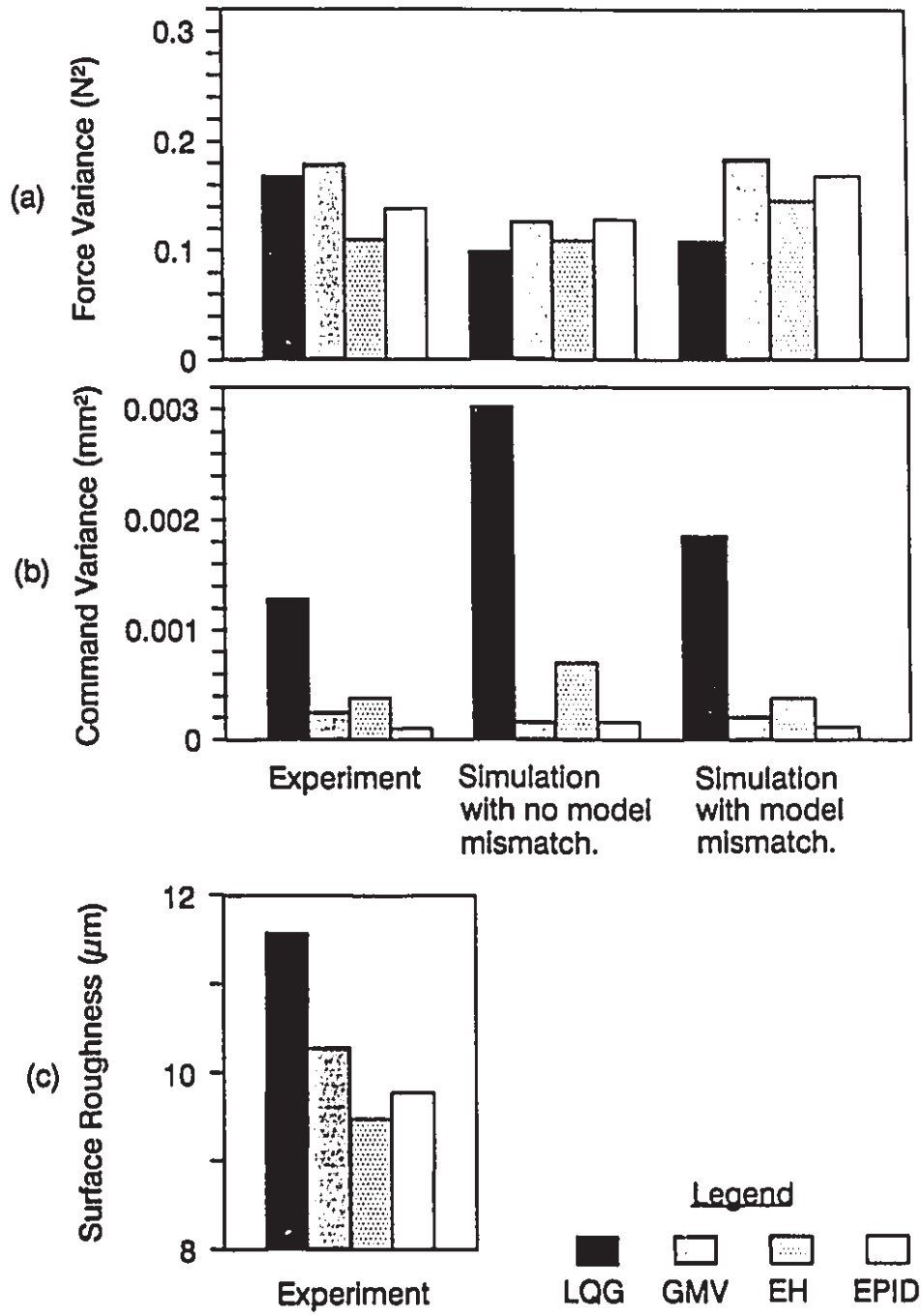

Figure 4.7 Comparison of the force control algorithms investigated. (a) Force variance. (b) Position command variance. (c) Chamfer surface roughness.

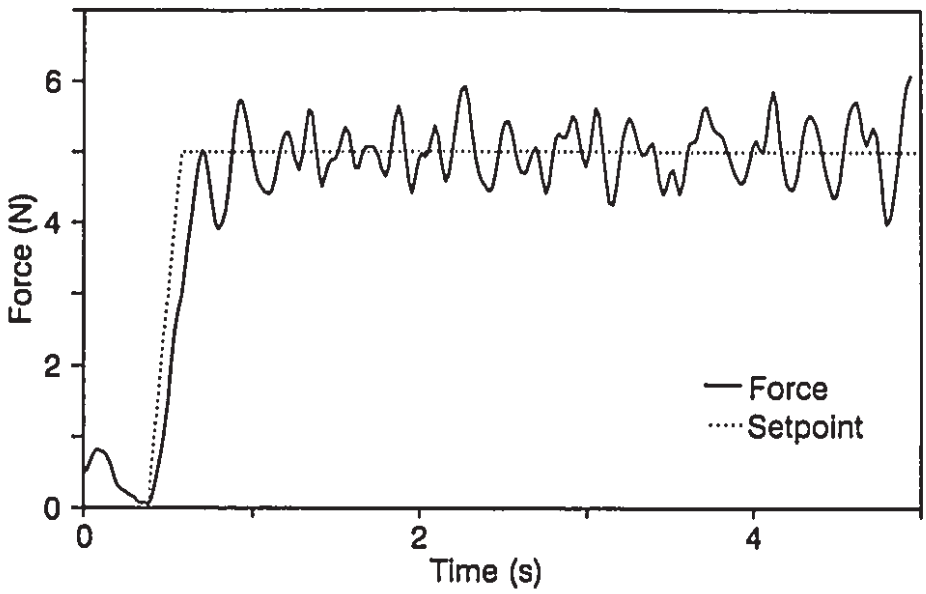

Figure 4.8 Experimental force response for LQG control.

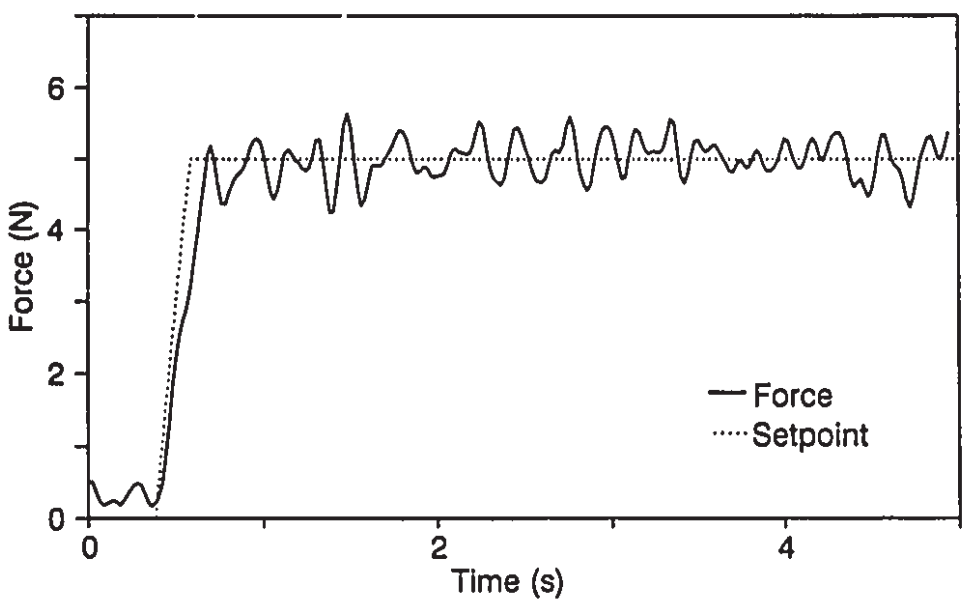

Figure 4.9 Experimental force response for EH control.

4.5 ADAPTIVE CONTROL: DESIGN AND SIMULATION

4.5.1 Introduction

For good performance the non-adaptive control algorithms investigated require the process dynamics to be both known and fairly time invariant. This was

the case for the control tests performed. However, when deburring more complex parts the robot arm's stiffness varies with configuration, and the deburring process is affected by part material, burr size, and feedrate variations. Simulations were performed to access the potential benefits of parameter adaptive force control for deburring with time varying process dynamics. An adaptive version of the Smith predictor [54], which has been shown to perform well with systems with deadtime, and a form of model reference adaptive control were investigated.

4.5.2 Parameter Estimation

With parameter adaptive control the process model parameters are estimated on-line and the control algorithm is updated based on these estimates. For the CARIMA model structure Recursive Least Squares (RLS) estimation is the most popular approach [55].

With RLS the data vector is given by:

$$\psi(t)^T = [-F(t-1), \ldots, -F(t-na) \mid x(t-k), \ldots, x(t-k-nb)] \tag{4.22}$$

The parameter vector is: $\theta = [a_p, \ldots, a_{na} \mid b_0, \ldots, b_{nb}]^T$ (4.23)

The estimation algorithm is then:

$$e(t) = F(t) - \psi^T(t)\theta(t-1) \tag{4.24}$$

$$\gamma(t) = \lambda + \psi(t)^T P(t-1)\psi(t) \tag{4.25}$$

$$\theta(t) = \theta(t-1) + P(t-1)\theta(t)e(t)/\gamma(t) \tag{4.26}$$

$$P(t) = [P(t-1) - P(t-1)\psi(t)\psi(t)^T P(t-1)/\gamma(t)]/\lambda \tag{4.27}$$

where $e(t)$ is the one-step-ahead prediction error, $P(t)$ is the covariance matrix, and λ is the forgetting factor.

4.5.3 Adaptive Smith Predictor

The structure of the Adaptive Smith Predictor (ASP) is given in Figure 4.10. The k step ahead force prediction is:

$$F_p(t) = B(q^{-1})x(t)/A(q^{-1}) \tag{4.28}$$

When the deadtime is included:

$$F_m(t) = B(q^{-1})x(t-k)/A(q^{-1}) \tag{4.29}$$

The modeling error is:

$$E_m(t) = F(t) - F_m(t) \tag{4.30}$$

The augmented force error is then:

$$E'(t) = F_r(t+k) - [F_p(t) + E_m(t)] \tag{4.31}$$

The control law is then the same as in EPID (equation 4.19) with the augmented error substituted for the force error. The controller was tuned as before (eq.'s 4.20 and 4.21), except that the parameter estimates are used.

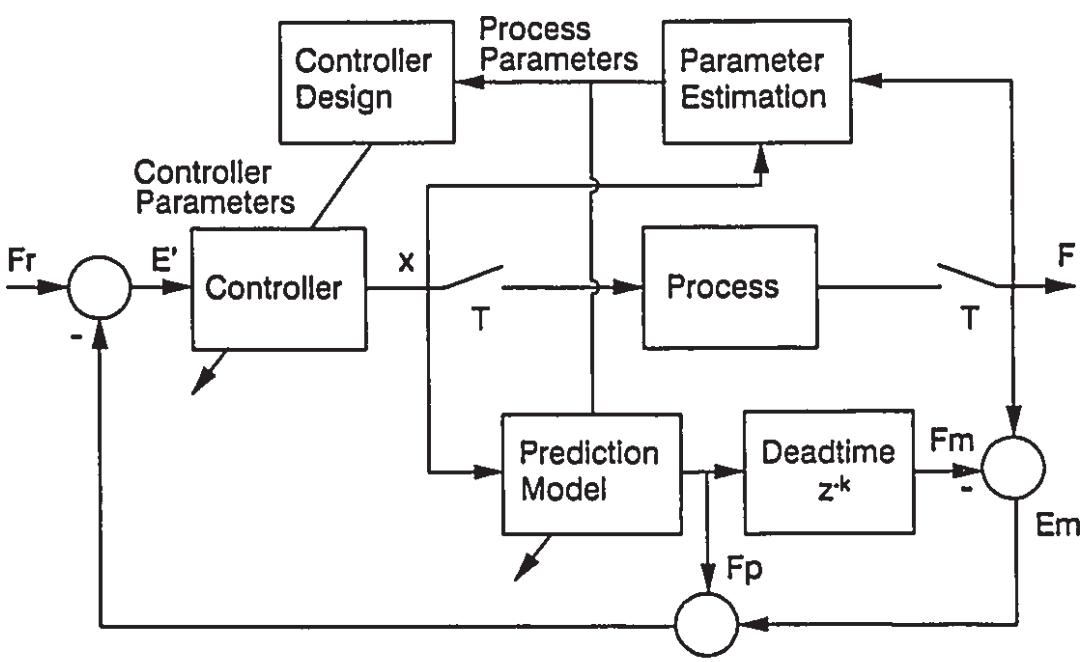

Figure 4.10 Structure of the Adaptive Smith Predictor.

4.5.4 Model Reference Adaptive Controller

The Model Reference Adaptive Control (MRAC) structure used is shown in Figure 4.11. Landau's [56] algorithm was used to design the control law. The regulation dynamics are defined by:

$$C(q^{-1}) = (1 + c_1 q^{-1} + \ldots + c_{na} q^{-na}) / (1 + c_1 + \ldots + c_{na}) \tag{4.32}$$

The controller design is then given by the identity:

$$C(q^{-1}) = A(q^{-1}) S(q^{-1}) + q^{-k-1} R(q^{-1}) \tag{4.33}$$

where $S(q^{-1}) = 1 + s_1 q^{-1} + \ldots + s_k q^{-k}$, and $R(q^{-1}) = r_0 + r_1 q^{-1} + \ldots + r_{na-1} q^{-na+1}$

The desired control is then:

$$x(t) = [C(q^{-1}) F_r(t+k) - R(q^{-1}) F(t) - B_s(q^{-1}) x(t)] / B(1) \tag{4.34}$$

where $B_s(q^{-1}) = B(q^{-1}) S(q^{-1}) - B(1)$ (4.35)

In equation (4.34) the steady state gain, $B(1)$, was used in place of $B(q^{-1})$ to prevent unbounded control due to the cancellation of zeros outside the unit circle.

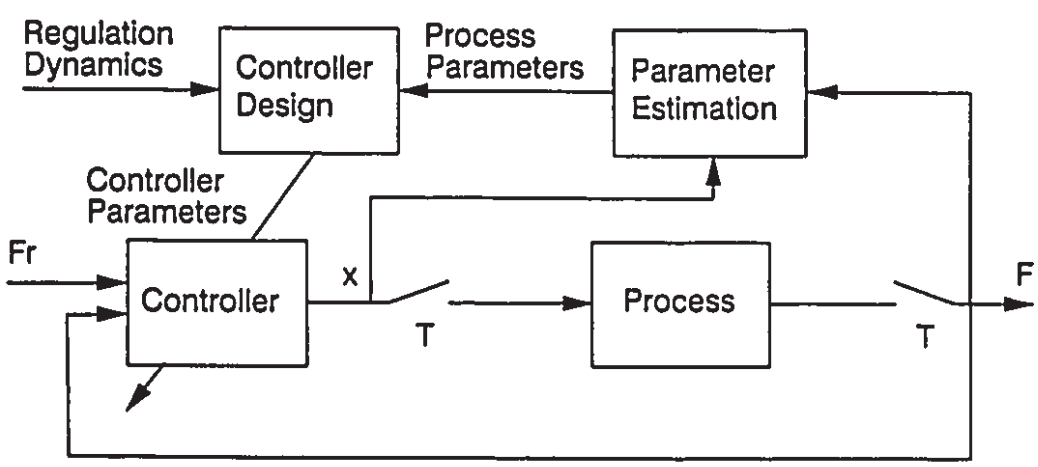

Figure 4.11 Structure of the Model Reference Adaptive Controller.

4.5.5 Simulation

The controllers' performance when subjected to sudden changes in the process parameters was simulated. The results are given in Figures 4.12-4.14. At times of 1 and 3 s the process was instantaneously switched between the different PRBS models to simulate the sudden changes in the cutting process or arm dynamics possible when deburring (when negotiating a corner for example). With the non-adaptive Smith predictor and a gain $K_c = 0.4$, the force response became highly oscillatory when subjected to the model changes as shown in Figure 4.12. With the ASP and the same gain the response stabilized quickly following the model changes (Figure 4.13a). The ASP response has a risetime of 0.07 s. To achieve an equally stable response with the non-adaptive predictor the gain had to be decreased to 0.15, which increased the risetime to 0.36 s.

The model gain (B(1)/A(1)) is compared to the process gain for the ASP in Figure 4.13b. The model gain converges in 0.5 s to within 1% of the process gain. This fast convergence was achieved by setting the covariance matrix $P = \alpha I$ whenever the force error exceeded 0.5 N. An α value of 10,000 was used, along with a forgetting factor of 0.95.

The MRAC system achieved a slower and less stable response than the ASP. A typical system response is shown in Figure 4.14. The regulation dynamics were set as critically damped, with the four poles at 0.35. The response was relatively slow with a risetime of 0.16 s, and a greater degree of oscillatory behaviour. Attempts to further increase the speed of response produced instability. This was probably due to the effect of the modified B polynomial used in the controller design to prevent unbounded control.

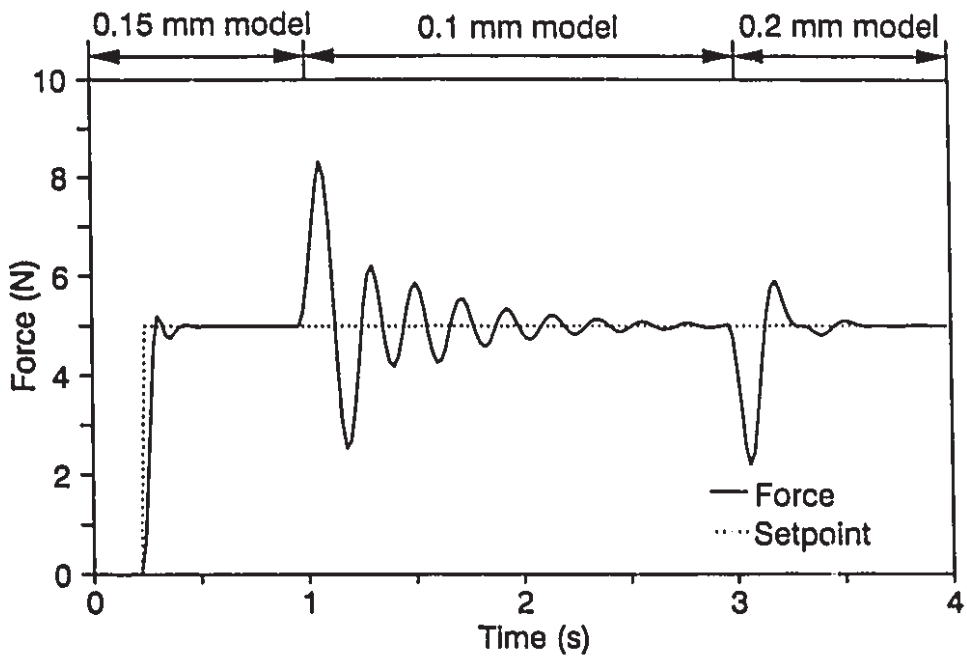

Figure 4.12 Simulated force response for a non-adaptive Smith predictor.

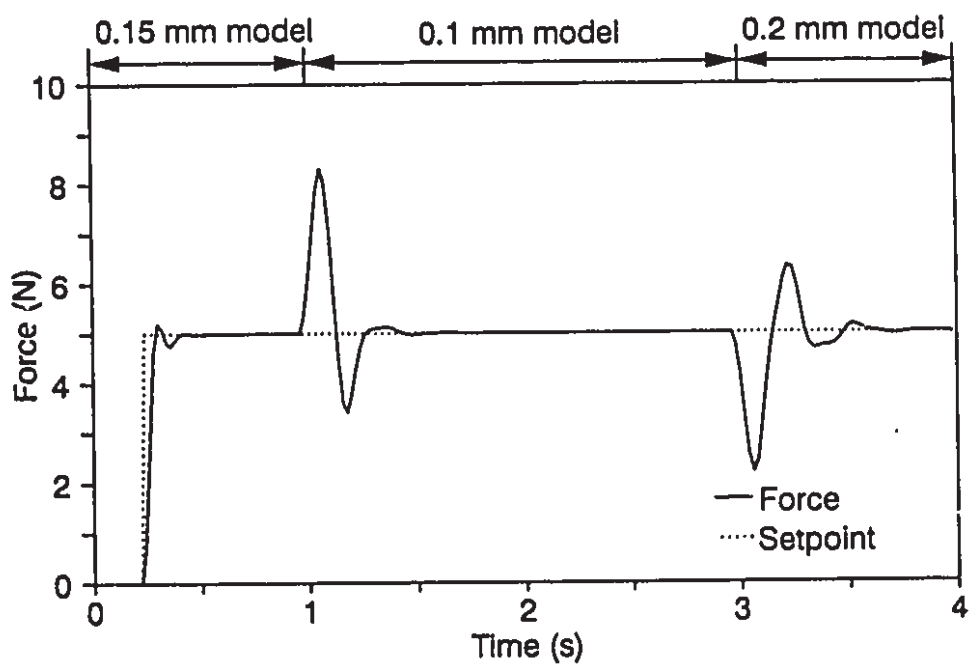

Figure 4.13a Simulated force response for the ASP.

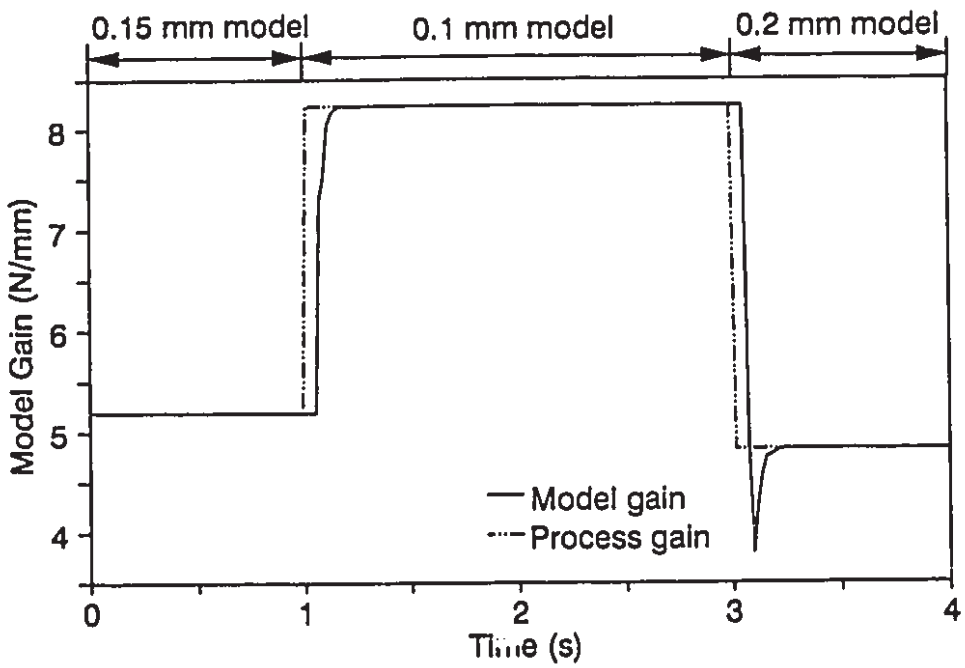

Figure 4.13b Simulated model gain for the ASP.

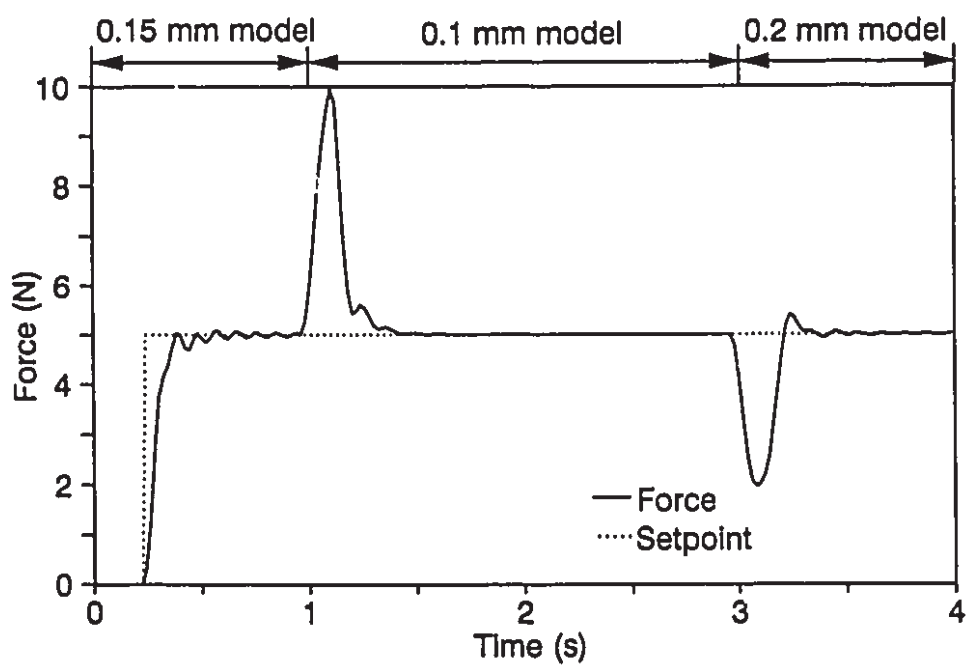

Figure 4.14 Simulated force response for the MRAC algorithm.

4.6 CONCLUSIONS

4.6.1 Non-Adaptive Control

Several non-adaptive force control algorithms based on a CARIMA time series process model were investigated. The objective was to control the chamfer depth by minimizing the normal force variance. The algorithms were evaluated through computer simulation prior to experimental verification using the PUMA-560 robot and the old AEE. Based on the experimental force variances and chamfer surface finish produced, the controllers ranked (from best to worst): EH, EPID, GMV, and LQG. The poor performance of the LQG design was attributed to the excitation of process nonlinearities as a result its large position command variance. The EH design achieved an experimental force variance of 0.11 N^2 for a 5 N reference force. This produced a chamfer with a depth of 0.68 mm and a roughness of 9.5 μm. Measurements of the chamfer depth under closed and open-loop conditions suggested that all of the controllers had a beneficial effect. With force control the depth remained a fairly constant 0.68 mm, while in the open-loop it varied from 0.23-0.57 mm along the length of the cut.

4.6.2 Adaptive Control

Simulations were performed to access the potential benefits of parameter adaptive force control for deburring with time varying process dynamics. The process model was instantaneously switched between three different CARIMA models to simulate the sudden changes in the cutting process or arm dynamics possible when deburring (when negotiating a corner for example). An adaptive version of the Smith predictor achieved a smooth, stable response with a risetime of 0.07 s. To achieve a

comparably smooth response the non-adaptive Smith predictor had to be detuned which increased the risetime to 0.36 s. A MRAC algorithm was also investigated which achieved a risetime of 0.16 s. Based on these results, along with the excellent experimental performance of the EH predictive controller, adaptive predictive control will be used as the control algorithm for the remainder of this work.

CHAPTER 5

SENSOR DEVELOPMENTS

5.1 INTRODUCTION

In the previous chapter force control was used to successfully control variations in the chamfer depth. To obtain a particular depth the relationship between the depth and the setpoint force must be both known, and constant. As discussed in Chapter 2, this relationship is a complex function of the tool, cutting conditions, and part material, and requires considerable off-line testing to obtain. When there are material hardness or feedrate variations, or the burrs are large relative to the chamfer depth, this function is not constant and the force cannot be used to accurately control the depth. Force control is also prone to overshoot or even instability at the time of initial tool/part contact [15, 25]. Given these limitations, one of the goals of this research was to develop a sensing system to more accurately and reliably measure the chamfer depth. The system combines the information from the force sensor and a newly developed vision sensor using a sensor fusion scheme. The resulting depth measurement is more accurate and reliable than possible using each sensor alone.

At the end of the chapter the development of the automated inspection system is described. The system uses the vision sensor hardware with software modified for the inspection case.

5.2 VISION SENSOR DEVELOPMENT

5.2.1 Introduction

The main design objectives for the vision sensor are to measure the tool's position relative to the part edge accurately, and at the fastest possible rate. The fast update rate is desirable since it allows a higher feedrate to be used without the measurements occurring too far apart (e.g. with a feedrate of 25 mm/s and a 50 Hz update rate the measurements occur every 0.5 mm). This type of measurement (i.e. distance of an object relative to a known reference) is termed range sensing. When the tool is contact with the edge the position measurement corresponds to the chamfer depth. Of the several range sensing methods available: time-of-flight, stereo vision (passive triangulation), moire, focusing, and active triangulation, active triangulation was chosen since it is fast, relatively inexpensive, and is the most well established [57]. Active triangulation requires a single camera and a structured light source. The range measurement is obtained by analyzing the image of the part edge illuminated by the structured light. The selection of the optical components, and other optical design issues, are described in the next section. The hardware pre-processing and image analysis are then described.

5.2.2 Optical Design

In this section the design of the sensor geometry and the selection of the individual optical components will be described. The design will be obtained from a set of design objectives, subject to practical constraints.

The sensor's design objectives are as follows (in order of importance):

1. Maximize the measurement accuracy.
2. Maximize the measurement update rate.
3. Field of view sufficient to track the edge.
4. Minimize the mass (concluded from the dynamic analysis in Chapter 3).
5. Minimize the overall size.

Objective 1 will be dependent on the triangulation geometry, the quality of the structured light source, the camera's resolution, the len's quality, the image processing used, and the image analysis algorithms used. With this in mind a laser line projector was chosen over a white light projection system due to the narrow light stripe achievable with the laser. A Newport Corporation V-SLM-S705 laser was selected. The S705 is a small, rugged, semiconductor laser with variable output power up to 10 mw, a 0.1 mm light stripe width, and a mass of 0.36 kg. Objective 2 is dependent on the video camera, and the image processing hardware and software. The video camera selected is an EG&G Reticon MC9256, a diode array type camera with a frame rate variable up to 105 Hz (the standard rate for video cameras is 30 Hz), a sensor array resolution of 256 lines × 256 pixels/line, and a mass of 0.34 kg. The image processing hardware is described in the next section. A field of view of 10 mm (diagonally) was chosen to provide a measurement range of about 5 mm. This range allows positioning errors (of the tool relative to the edge) of up to 5 mm. Assuming an ideal lens for simplicity, the object-lens-image relationship is defined by the classic lens equations:

$$(1/L)+(1/L')=(1/F) \quad \text{and} \tag{5.1}$$

$$M=L'/L=FOV/AL \tag{5.2}$$

where L is the working distance (from object to lens), L' is the extension length

(from lens to sensor array), F is the len's effective focal length , M is the object-to-image magnification, FOV is the field of view, and AL is the length of the sensor array. For the camera's array length (diagonally) of 14.5 mm, equation 5.2 gives $M=0.69$. To keep the lens away from the part and cutting action, without making the sensor too large, a working distance of 50 mm was chosen. Then from equations 5.1 and 5.2, $L=72$ mm, and $F=30$ mm. A Cosmicar CCTV lens with $F=32$ mm (the closest available focal length) was selected. When a 30 mm extension tube was used, the field of view and working distance were approximately 12 mm, and 50 mm, respectively. The vision sensor is shown mounted on the AEE in Figure 5.1. The laser, video camera, and deburring tool are rigidly connected. A sectional view of the triangulation geometry is shown in Figure 5.2. Ideally, for maximum accuracy, the measurement should be taken at the tool/part contact point, but since this was not possible the measurement is taken a distance D ahead. This also allows the edge location to be measured just prior to the initial contact at the beginning of the deburring pass. The relationship between the distance measured by the camera, c', and the distance moved by the part, a, is obtained from an analysis of the triangulation geometry detailed in Figure 5.2(b) as:

$$b=a/sin\alpha \tag{5.3}$$

$$c=bsinB=asinB/sin\alpha \quad \text{and} \tag{5.4}$$

$$c'=c/M=asinB/Msin\alpha \tag{5.5}$$

For maximum accuracy the sensor's sensitivity, given by the ratio c'/a, should be maximized. From equation 5.5 it can be seen that to maximize the sensitivity, α should be minimized, and B set equal to 90°. While B may be easily set close to 90°, small values of α increase the lead distance D and the width of the light stripe seen

by the camera, both of which can decrease the sensor's accuracy. A further issue is the effect of α on the reflections from the part surface. Specular (mirror-like) reflections were found to cause camera saturation which resulted in a highly distorted image. These reflections occur when the angle of incidence, α, is equal to the viewing angle, $180° - (\alpha + B)$. With $B = 90°$ this condition occurs when $\alpha = 45°$. Based on these considerations α was set to 60°, which gives a theoretical sensitivity of 1.67 mm/mm or 42 pixels/mm. The completed sensor has an overall size of about 300 × 50 × 200 mm (length × width × height) with a mass of 1.0 kg. The lead distance, D, is 12 mm. This was the minimum value achievable with the 9.5 mm diameter cutting tool.

5.2.3 Hardware Pre-processing

The image processing hardware performs image processing and preliminary image analysis to reduce the large quantity of information output by the video camera to only the quantities required for the remaining analysis. The hardware consists of an EG&G Reticon MB9000 Video Data Formatter, and a custom-built hardware circuit.

The camera outputs an analog video signal on a line by line basis, beginning with the first pixel of the first line, and ending with the last pixel of the last line. The transmission of each pixel is initiated by a clock pulse generated by the Formatter. The clock frequency can be varied according to the formula: $8/2^n$ MHz for $n = 0$ to 7. In accordance with design objective 2 the maximum clock frequency of 8 MHz was used, to give a frame rate of 105 Hz. As each pixel is output it's voltage level is digitized with a 6-bit resolution, and digitally thresholded to binary by the Formatter. Thresholding was used to reduce the quantity of data per pixel from 6 to 1 bits, and

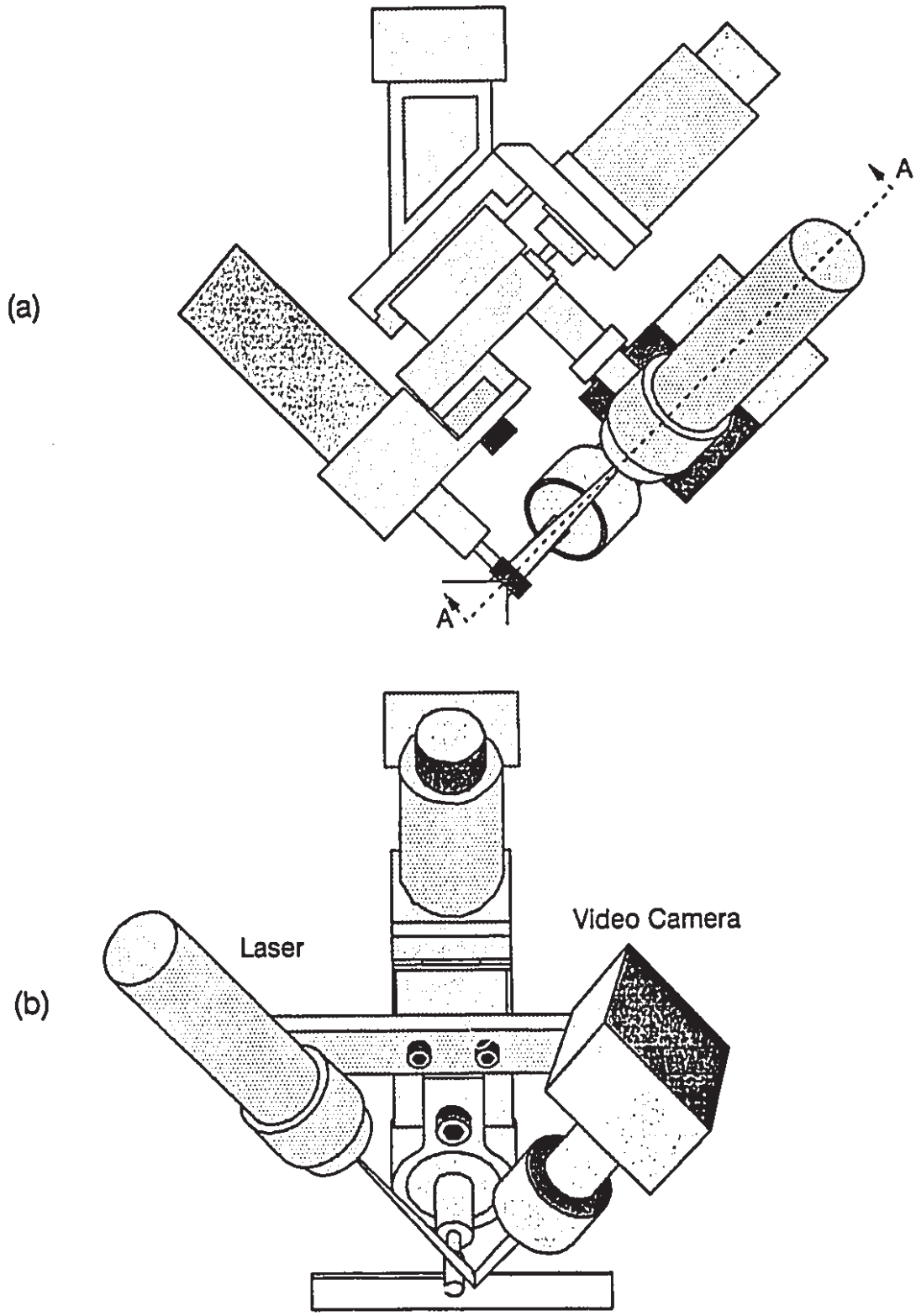

Figure 5.1 The vision sensor shown mounted on the AEE. (a) Side view. (b) Front view.

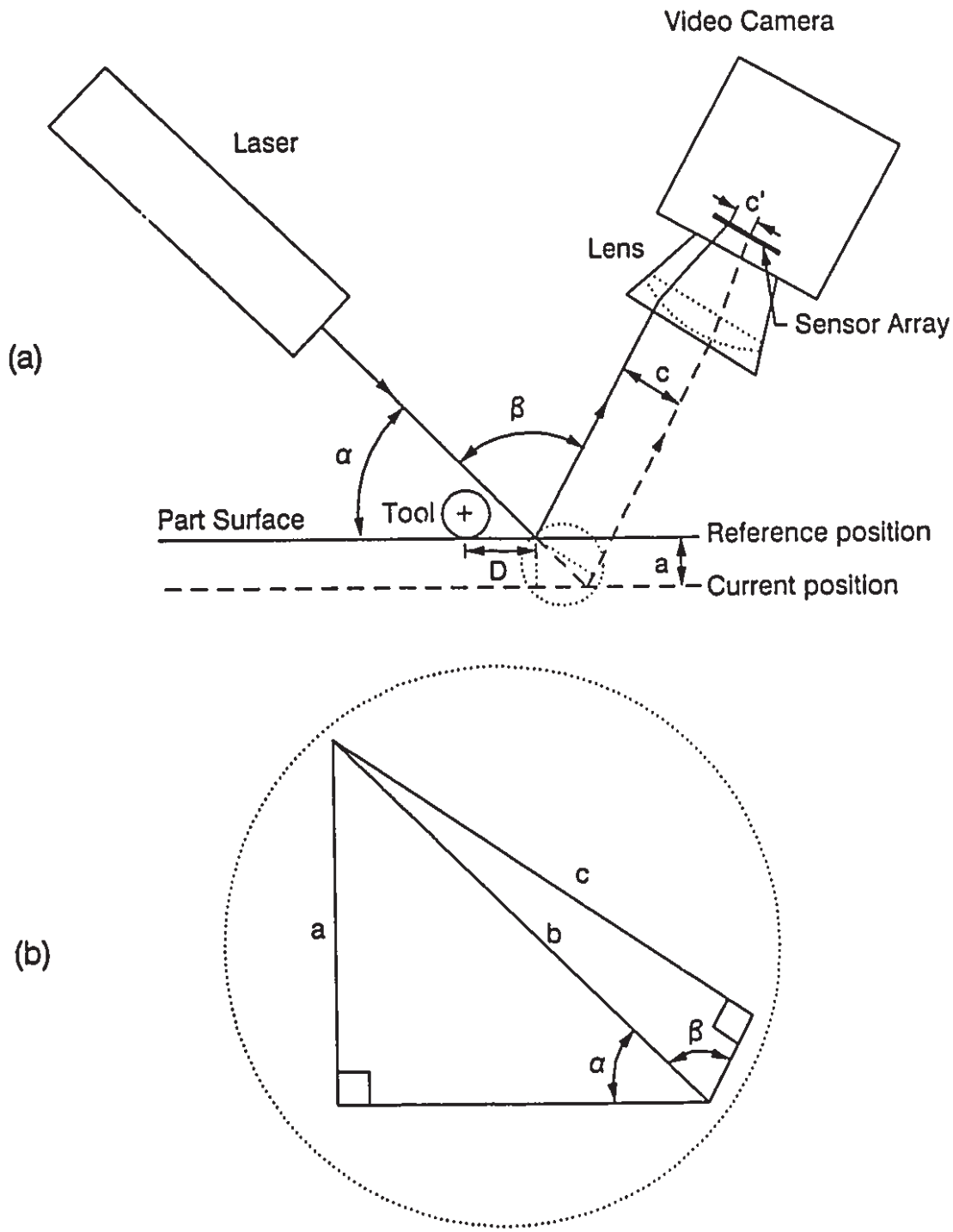

Figure 5.2 (a) Sectional view of the vision sensor's triangulation geometry (section A-A in Figure 5.1(a)). (b) Detail.

also to segment the image foreground (the light stripe) from the image background. Because the light stripe is distinctly brighter than the image background the level of this threshold was not found to be critical and following some experimentation was set to 8 (12.7% of maximum brightness). A custom hardware circuit is then used to encode the image in a run-length form. For the light stripe image each line of the binary image has only one dark-to-light (rising edge) transition corresponding to the beginning of the stripe, followed by one light-to-dark (falling edge) transition indicating the end of the stripe. The dark-to-light transition (hereafter referred to as the stripe start) was recorded by using an 8-bit counter to count the clock pulses until the rising edge occurs. At the rising edge a second 8-bit counter begins counting the pulses until the falling edge occurs, to record the stripe width. The quantity of information has now been reduced to 2 bytes or 16 bits/line from the 1536 bits/line in the original digitized video. At the end of each line these byte values are read into a Single Board Computer (SBC) which performs the remaining image analysis.

5.2.4 Image Analysis

The secondary image analysis is performed mainly on an Intel EV80C196KC SBC programmed in Intel 8096 assembly language. The EV80C196KC has a 16 MHz 16-bit microprocessor (Intel's 80C196KC) and 32k of RAM. Because of the slow speed of floating point arithmetic calculations on the SBC, fixed point arithmetic is used (with no loss of precision). The final line fitting calculations requiring floating point arithmetic are performed on a 33 MHz Intel 80486-based microcomputer programmed in C.

The analysis involves fitting a polyline (i.e. a concatenation of line segments

[58]) to the centres of the stripe of light. This is illustrated in Figure 5.3. The tool position is then obtained from the location of the part corner, given by the intersection of top and side surface segments. The centres are obtained by simply adding one half of the stripe's width to its start location for each line of video. Exceptions to this formula occur at the frame boundaries (i.e. pixels 0 and 255) where the stripe's width is truncated. To prevent these incorrect centre values from being used, centres whose start=0 pixels, or whose start+width=255 pixels are ignored. Gaps in the stripe image are detected when the width=0. It was found that for successful segmentation of the polyline these gaps had to be filled. The simple extrapolation formula:

$$\hat{y}(l) = (l - l_n)[y(l_n) - y(l_{n-4})]/(l_n - l_{n-4}) \tag{5.6}$$

is used, where $\hat{y}(l)$ is the estimated centre for the current line l, $y(l_n)$ is the previous centre, $y(l_{n-4})$ is the 4th previous centre, l_n is the line number for the previous centre, and l_{n-4} the line number of the 4th previous centre. The polyline is segmented using a merging algorithm [58]. In a merging algorithm data points are merged into the current line segment until a breakpoint (corner) is found. Following the breakpoint a new segment is begun. The breakpoints are found by monitoring the curvature of the sequence of stripe centres. A breakpoint is set when the curvature is a local maximum above a threshold value, as follows:

IF $(y(l) \neq 0)$ *THEN*

$y'(l) = y(l)$

ELSE

$y'(l) = \hat{y}(l)$

END IF

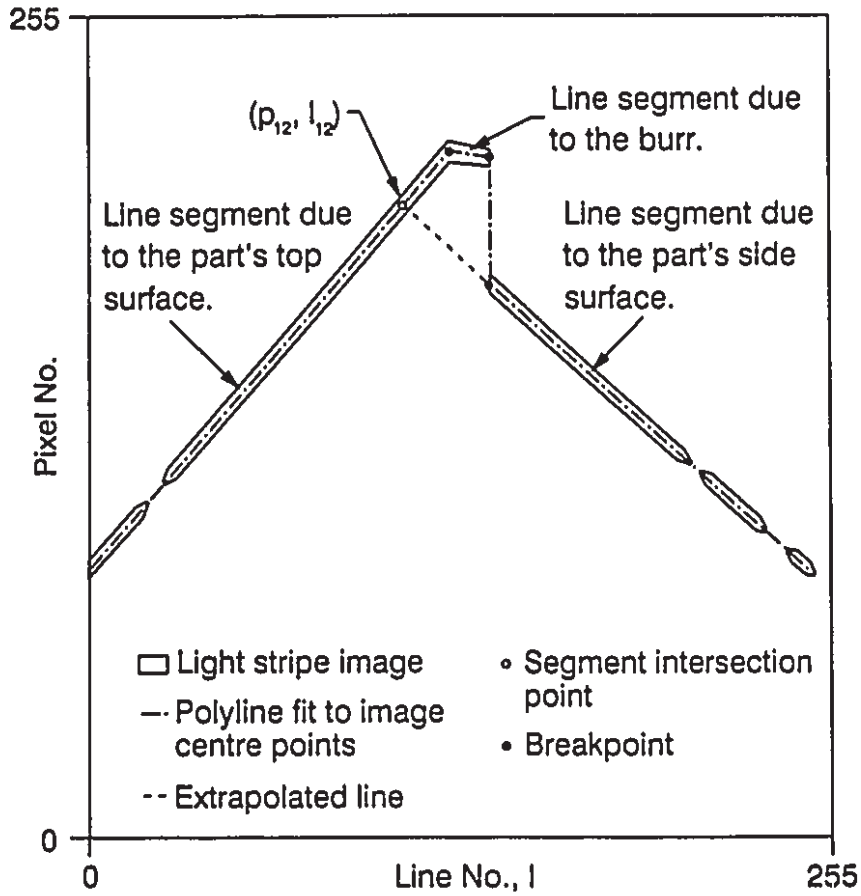

Figure 5.3 Image analysis of the light stripe for the deburring case.

$\Gamma(l-\delta) = |y'(l) - 2y'(l-\delta) + y'(l-2\delta)|$ where $\delta \geq 1$

IF $(\Gamma(l-\delta-2) \geq \Gamma(l-\delta)$ *AND* $\Gamma(l-\delta-2) \geq \Gamma(l-\delta-4))$ *THEN*

IF $(\Gamma(l-\delta-2) \geq \Gamma_{th})$ *THEN*

$l_b = l-\delta-2$

END IF

END IF

where $\Gamma(l)$ is the curvature index at line l, $y'(l)$ is the stripe centre at line l, δ is the smoothing step size in lines, Γ_{th} is the curvature threshold, and l_b is the breakpoint line number. This algorithm is based on Shirai's work [59], and is very efficient because it allows the polyline segmentation and line fitting to be performed during the transmission of the video image, unlike some other approaches which require the entire image before the analysis can begin. Because the delay between the current line and breakpoint detection is $\delta+4$ lines, the line fitting must be delayed by at least $\delta+4$ lines. The remaining data points are then fit at the end of the frame. Because the next video frame is transmitted almost immediately after the current frame, the last lines of the current frame must be skipped to allow time for these calculations. This is undesirable since skipping lines reduces the frame's size and resolution, which could in turn reduce the sensor's range and accuracy. With this in mind δ should be set equal to 1, its lower limit. However a δ value greater than 1 is necessary to reduce the effect of noise on $\Gamma(l)$, by effectively low-pass filtering the $\Gamma(l)$ values. The larger the step size the greater the noise reduction. Following some experimentation a value of $\delta=8$ was found to be a reasonable compromise between maximum noise reduction and minimum reduction in frame size. When the additional delay required for data transmission to the microcomputer was included the frame

size had to be reduced to 236 lines. To allow time for the segmentation and line fitting to be performed it was also necessary to skip alternate lines during the frame. This reduces the line resolution by one half. Since the range measurement is derived from the stripe centre pixel coordinates, this reduction has minimal effect on the accuracy. It does reduce the number of points per line segment, which could then lead to a poor quality fit. In practice however, the quality of fit was found to be extremely good. A sample result is shown in Figure 5.4. The merging algorithm correctly located the breakpoint between the top and side surface segments at line 126. In this particular case the burr with an approximate height of 0.2 mm located on the part corner did not generate any line segments, but instead generated a discontinuity in the image at the breakpoint. Any segments due to burrs are ignored by rejecting any segment whose length is under 20 lines. From Figure 5.4(b) it can be seen that the corner is easily discernable from the noise, and the value of the threshold, Γ_{th}, (set equal to 12) is not critical.

The conventional least-squares method is used to fit the stripe centres of each line segment to equations of the form:

$$y(l) = m_i l + b_i \tag{5.7}$$

where i is the segment number, m is the slope, and b is the intercept. The required summations: $\Sigma\, l$, $\Sigma\, y(l)$, $\Sigma\, l^2$, $\Sigma\, y^2(l)$, and $\Sigma\, ly(l)$, for each segment are computed during the video frame. These values are then sent, along with a status byte, to the 80486 microcomputer which computes the slopes, intercepts, and coefficient of determination (R^2) values. The R^2 values indicate the quality of the fit, with unity indicating a perfect fit. For the results shown in Figure 5.4 the R^2 values were 0.9999 and 0.9983 for the top and side surfaces respectively. The status byte is used to

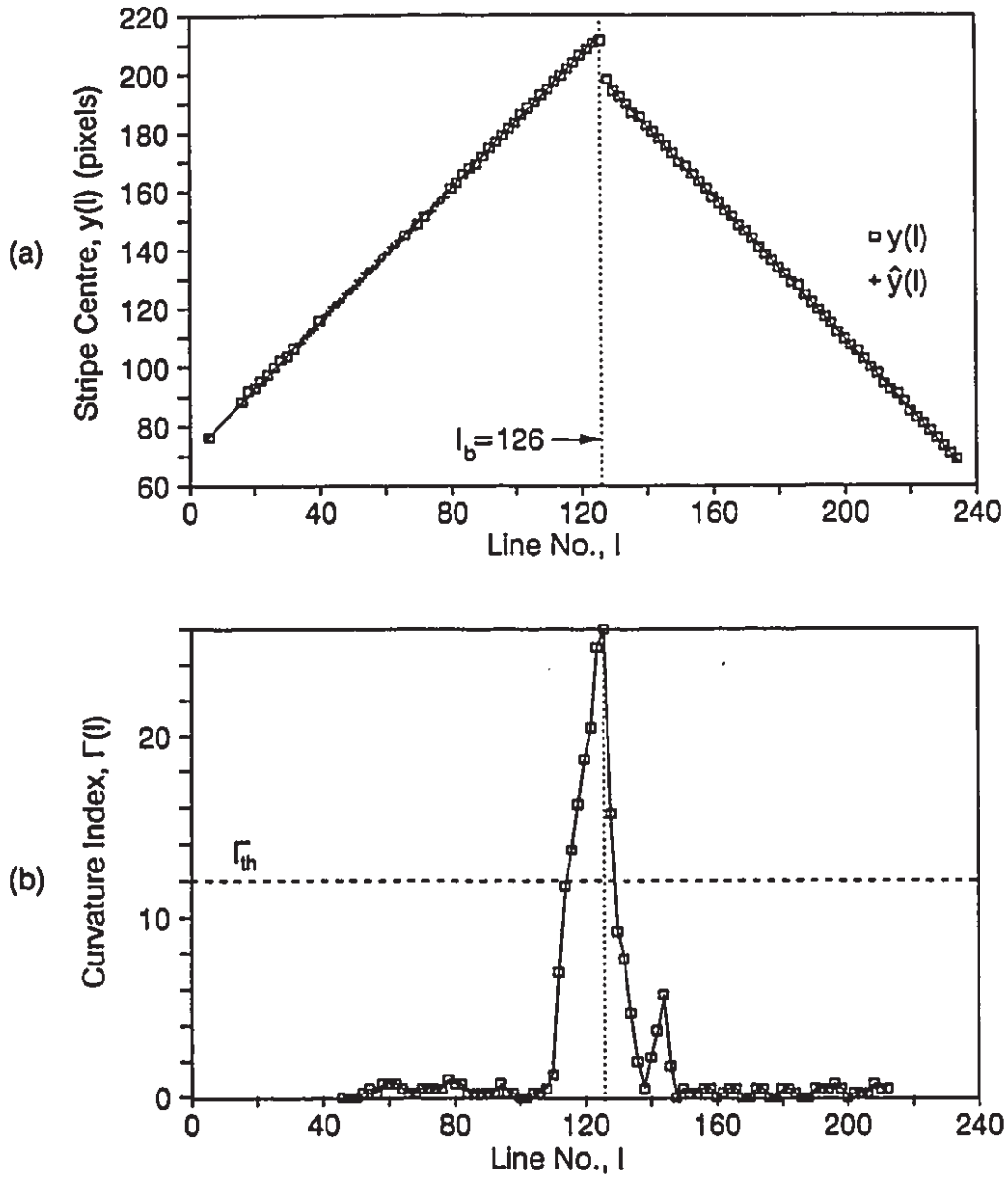

Figure 5.4 Image analysis results for the deburring case. (a) Stripe centre vs. line number. (b) Curvature index vs. line number.

indicate whether the correct number (i.e. 2) of line segments have been identified or not. The location of the part corner is given by the intersection of the top and side surface segments, numbered *1* and *2* respectively, as:

$$l_{12}=(b_2-b_1)/(m_1-m_2) \text{ and} \tag{5.8}$$

$$p_{12}=m_1 l_{12}+b_1 \tag{5.9}$$

where: l_{12} is corner's line coordinate, p_{12} is the corner's pixel coordinate. Note that l_{12} and p_{12} are floating point values with subpixel precision. Because the tool and camera are rigidly connected, the tool position relative to the part edge is simply:

$$d_v=c_1 p_{12}+c_2 \tag{5.10}$$

where d_v is the tool position relative to the edge, and $c_{1,2}$ are calibration constants. The tool position is equivalent to the chamfer depth when deburring, so d_v is also the vision sensor's chamfer depth measurement. The sensor calibration procedure and results are detailed in Appendix B. In these tests the sensor achieved a precision of ±1.2 μm, and an accuracy of ±13 μm over a 1 mm measurement range. The maximum measurement range of the tool position relative to the edge is −6 to 3 mm.

5.3 FUSION OF FORCE AND VISION SENSORY INFORMATION

The limitations of using force sensing for control of deburring were discussed in section 5.1. While vision sensing is capable of a very accurate measurement (independent of the cutting conditions), its reliability was found to be much lower than force sensing's. Vision sensing was found to fail for a variety of reasons: sensitivity to changes in part finish (resulting in an incomplete or saturated image), occlusion of the part edge, image analysis failure, or if the edge was outside the sensor's field of view. These failures are indicated by the analysis software when too

few or too many line segments are detected, the parameters of the least square fits are outside their ranges of expected values, or the average quality of the line fits is poor. In pseudo-code:

```
IF (i_max ≠ 2) THEN
    vision_sensor_status = FAILED
ELSE IF ( |(m_1 - m_1^*)/m_1^*| > 0.25 OR |(m_2 - m_2^*)/m_2^*| > 0.25 OR
    ((R_1^2 + R_2^2)/2) < 0.95) THEN
        vision_sensor_status = FAILED
    ELSE
        vision_sensor_status = ACTIVE
    END IF
END IF
```

where i_{max} is the number of line segments detected, and $m^*_{1,2}$ are the expected slopes. Force sensor failure is indicated when there is no contact between the tool and part (determined by a simple electrical continuity check). The limitations of using force or vision sensing alone prompted the development of a new sensor fusion based approach. With this approach the information from the force and vision sensors is combined to give a more accurate and reliable measurement of the chamfer depth.

The force is first transformed to an estimate of the depth using:

$$d_f(t) = k_f F(t) \tag{5.11}$$

where $d_f(t)$ is the force sensor depth estimate at sample time t, k_f is the gain, and $F(t)$ is the normal force measurement. This static model was used because the dynamics between the depth and the force were found to be non-causal. When the force depth estimate is used in the controller the missing depth/force dynamics are accounted for

by switching the process model (see Chapter 6, section 6.2.2). Rather than use a fixed gain, which would be dependant on the tool, part material, and cutting conditions, the gain is estimated on-line. The estimator minimizes the error between the estimate, $d_f(t)$, and the vision measurement, $d_v(t)$. The estimation algorithm is the same one used to identify the process model (as described in section 6.2.2), except that the force and vision measurements are both digitally low-pass pre-filtered at 2 Hz to improve the gain estimate. Since the vision sensor provides the most accurate measurement, $d_f(t)$ is used only in the case of vision failure. For the four possible failure cases, the depth measurement, $d(t)$, is given by:

1. No sensor failure: $d(t)=d_v(t)$.
2. Force sensor failure: $d(t)=d_v(t)$.
3. Vision sensor failure: $d(t)=d_f(t)$.
4. Both sensors fail: $d(t)=d(t-1)$.

Additionally, in case 4 the controller is halted (i.e. the current command is set equal to the previous one) to prevent unsafe drifting.

In Figure 5.5 a scenario for sensor fusion during a deburring pass is shown. During the initial approach the force sensor fails and the vision sensor measurement must be used. When deburring is under way and both sensors are active, the vision measurement is used, and the gain k_f is continually estimated. When the edge is no longer in the vision sensor's field of view near the end of the pass, the vision sensor fails and the depth estimate from the force is used. The fusion strategy will be tested experimentally in Chapter 7.

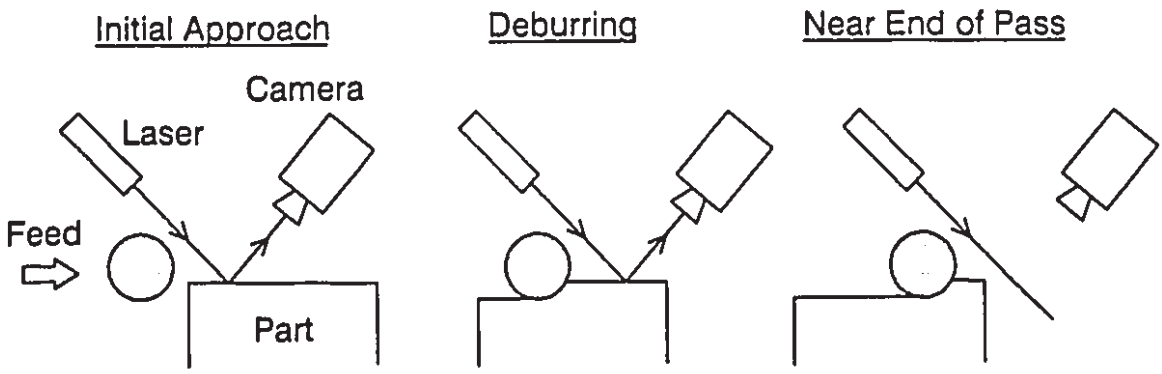

Figure 5.5 Scenario for sensor fusion during a deburring pass.

5.4 INSPECTION SYSTEM DEVELOPMENT

The inspection system is used to verify the deburring performance in a secondary non-contact inspection pass. The same hardware as in the vision sensor is used with software modified for the inspection case. During the inspection pass the chamfer depth and angles (relative to the top and side surfaces) are obtained from the slopes and intercepts of the line segments 1-3 (the top surface, chamfer surface, and side surface respectively) as shown in Figure 5.6. Because of the short length of the chamfer surface it was not possible to skip alternate lines (as with the vision sensor) without affecting the line fit quality. Without line skipping the clock frequency had to be set to 4 MHz, reducing the frame rate to 52.5 Hz. The reduced frame size was 233 lines. Following image segmentation and line fitting, inspection sensor failure is detected as follows:

$$IF\ (i_{max} \neq 3)\ THEN$$

$$inspection\_system\_status = FAILED$$

$$ELSE\ IF\ (|(m_1 - m_1^*)/m_1^*| > 0.25\ OR\ |(m_2 - m_2^*)/m_1^*| > 0.25\ OR$$

$$|(m_3 - m_3^*)/m_3^*| > 0.25\ OR\ ((R_1^2 + R_2^2 + R_3^2)/3) < 0.85)\ THEN$$

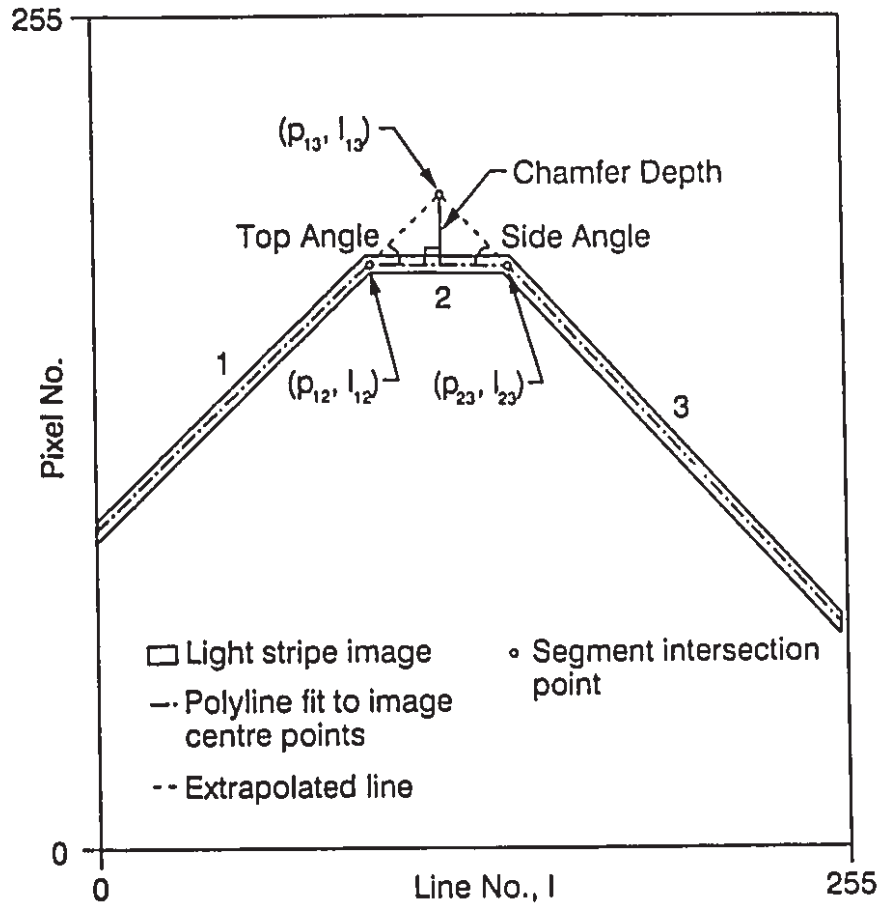

Figure 5.6 Image analysis of the light stripe for the inspection case.

inspection_system_status = FAILED

ELSE

inspection_system_status = ACTIVE

END IF

END IF.

Note that since $m_2^* = 0$ the term $(m_2 - m_2^*)$ is scaled by $1/m_1^*$ rather than $1/m_2^*$.

If the system is active the segment intersection points are solved in the same manner as in equations 5.8 and 5.9. The inspected depth and angles are given by:

$$d_i = c_3 \sin(\tan^{-1}(m_1) - \tan^{-1}(m_2))[(l_{13} - l_{12})^2 + (p_{13} - p_{12})^2]^{1/2} + c_4 \qquad (5.12)$$

$$\theta_t = c_5[\tan^{-1}(m_1) - \tan^{-1}(m_2)] + c_6 \quad \text{and} \qquad (5.13)$$

$$\theta_s = c_7[\tan^{-1}(m_2) - \tan^{-1}(m_3)] + c_8 \qquad (5.14)$$

where d_i is the inspected depth, θ_t is the top angle, θ_s is the side angle, and $c_{3\text{-}8}$ are calibration constants. The calibration procedure and results are detailed in Appendix C. In these tests the system achieved a precision of ±3.6 μm, and an accuracy of ±24 μm over a 0.2-0.8 mm range of depths; and an accuracy of 2° over a range of 40-50° for both angle measurements. The depth accuracy is worse than for the deburring case because the chamfer surface line segment was too short to obtain a good quality of fit. This also accounts for the low accuracy of the angle measurements. Since depth control is the main emphasis of this work, the angle measurements will not be used.

A sample image analysis result is shown in Figure 5.7. Note that because the chamfered edge profile is smoother than the burred edge the values of the curvature index at the breakpoints are much smaller than observed for the deburring case (in Figure 5.4). Although this reduced the difference between the breakpoint peaks and

the noise, the merging algorithm correctly located the breakpoints at lines 107 and 126. The R^2 values were 0.9998, 0.7092, and 0.9999 for segments 1-3 respectively. The depth measurement was 0.35 mm. In comparison to a reference measurement performed with a Nikon Measurescope microscope the error was 12 μm, which is within the systems accuracy limit.

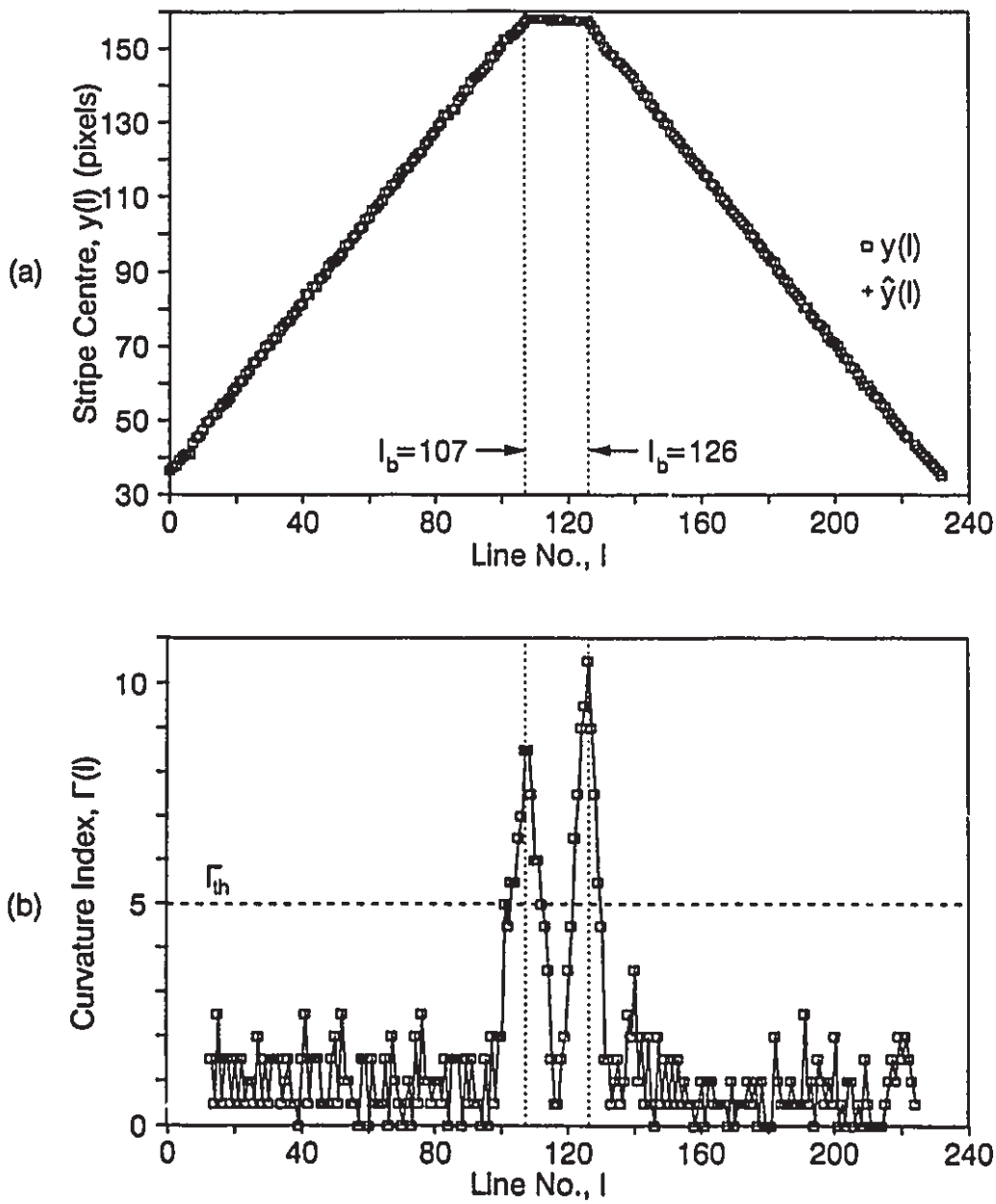

Figure 5.7 Image analysis results for the inspection case. (a) Stripe centre vs. line number. (b) Curvature index vs. line number.

CHAPTER 6

CHAMFER DEPTH CONTROL

6.1 INTRODUCTION

In Chapter 4 on force control, it was concluded that adaptive predictive control is well suited to the robotic deburring problem. In Chapter 5 the limitations of force sensing were discussed, and a new sensing system was developed to allow the chamfer depth to be measured directly on-line. In this chapter, adaptive predictive control is applied to the problem of controlling the chamfer depth. The predictive control algorithm is then modified to include learning control. This new algorithm is shown, both theoretically and experimentally, to improve the regulation of a process with a partially repeatable disturbance. An alternate form of the algorithm is then developed for the robotic deburring case.

6.2 ADAPTIVE PREDICTIVE CONTROL: DESIGN AND SIMULATION

6.2.1 Introduction

Of the various predictive control algorithms proposed in recent years, Generalized Predictive Control (GPC) was chosen for this work. GPC is an extension of GMV and EH control, and has been applied successfully to many industrial processes, including robotic grinding [60].

6.2.2 Process Modelling

As in Chapter 4 the process dynamics are modelled by a CARIMA type time series model. For controlling the chamfer depth this has the form:

$$A(q^{-1})d(t) = B(q^{-1})x(t-1) + C(q^{-1})\xi(t)/\Delta \tag{6.1}$$

where $A(q^{-1}) = 1 + a_1 q^{-1} + \ldots + a_{na} q^{-na}$, $B(q^{-1}) = b_0 + b_1 q^{-1} + \ldots + b_{nb} q^{-nb}$, $C(q^{-1}) = 1 + c_1 q^{-1} + \ldots + c_{nc} q^{-nc}$, $d(t)$ is the chamfer depth measurement, $x(t-1)$ is the end effector position command, $\{\xi(t)\}$ is a zero mean uncorrelated random sequence, and Δ is the differencing operator.

For control of the deburring operation three CARIMA models are used alternately. A common structure of $na=4$, $nb=5$ (with $b_0=0$) is used so that only the model parameters had to be changed. The first model is used during initial approach (prior to tool/part contact). Since the non-contact dynamics are not a function of the deburring conditions, this model is not estimated on-line, and was obtained from an off-line test. The parameters are: $a_1=0.150$, $a_2=0.247$, $a_3=-0.098$, $a_4=0.0$, $b_1=0.263$, $b_2=0.663$, $b_3=0.323$, and $b_4=0.0$. During deburring the controller switches between two contact models corresponding to $d_f(t)$ or $d_v(t)$, depending on which one is being used for $d(t)$. This scheme is necessary because of the dynamics missing from $d_f(t)$, as mentioned in Chapter 5, section 5.3. To adapt to changes in dynamics, the parameters of both contact models are estimated on-line. Initial values for the parameters were obtained from off-line tests. For the $d_v(t)$ model the initial parameters are: $a_1=0.281$, $a_2=0.017$, $a_3=0.058$, $a_4=0.127$, $b_1=0.278$, $b_2=0.560$, $b_3=0.133$, and $b_4=0.048$. For the $d_f(t)$ model the initial parameters are: $a_1=0.160$, $a_2=0.408$, $a_3=-0.033$, $a_4=0.073$, $b_1=0.0$, $b_2=2.51k_f$, $b_3=11.04k_f$, and $b_4=4.15k_f$. Note

that all three models are non-minimum phase. Hereafter the steady state gain of the $d_v(t)$ CARIMA model ($B(1)/A(1)$) is referred to as the "model gain".

As in Chapter 4, RLS parameter estimation will be used. For fast convergence the covariance matrix, **P**, is initially set equal to α**I**, where α is a "large" number. The estimator is periodically shut-off to prevent drift due to lack of excitation. If the modelling error increases, the estimator can be restarted and **P** is reset to α**I**. In the previous simulations (Chapter 4, section 4.5.5) this resetting was performed when the controller error exceeded a threshold value. This scheme has two main limitations: a large controller error does not necessary mean the model is poor, and if a single threshold is used the scheme is sensitive to noise. Unlike in the earlier adaptive control simulations, a stochastic disturbance will be included here to better model the actual deburring situation. This disturbance puts greater demands on both the estimator and the scheme used to supervise it.

Isermann and Lachmann [61] concluded that several indices are suitable for monitoring a recursive estimator, with the simplest being the one-step-ahead prediction error, and the mean of the prediction error. In this work a different index, the mean absolute prediction error, will be used. This choice was based on computer simulations which compared the sensitivity of each index to model mismatch. In Figure 6.1 a mismatch between the model and the process was introduced from $t = 20$-60 s. Specifically the model was first order with a gain of 1 and a pole of 0.8 while the process had a gain of 2 and a pole of 0.5. While the prediction error was clearly sensitive to the mismatch, its high frequency oscillations make it unsuitable as a monitoring index. The mean error was insensitive, and also shows considerable

oscillation. The mean absolute error was both sensitive to the mismatch and free of large oscillations, making it the most suitable monitoring index. The mean absolute error is computed by recursive averaging (with exponential forgetting):

$$\bar{e}(t) = \gamma\bar{e}(t-1) + (1-\gamma)\,|e(t)| \tag{6.2}$$

where a γ value of 0.9 was used. The next issue is how this index is used to supervise the estimator.

The supervising scheme uses $\bar{e}(t)$ with hysteresis and a deadband. In this scheme two thresholds are used to reduce the possibility of frequent resetting, which can occur with a single threshold as the index oscillates about it. The scheme is as follows: 1) To minimize parameter drift the estimator is shut-off when the mean absolute prediction error, $\bar{e}(t)$, is less than $\bar{e}_{lbound}$, and 2) The estimator is restarted and $\mathbf{P}$ is reset to $\alpha\mathbf{I}$ when $\bar{e}(t) > \bar{e}_{ubound}$ (where $\bar{e}_{ubound} > \bar{e}_{lbound}$). As shown in Figure 6.1 the lower threshold, $\bar{e}_{lbound}$, should be selected so that it is above the error level with no mismatch (due to the disturbance $\xi(t)$). The upper threshold, $\bar{e}_{ubound}$, should be set higher than $\bar{e}_{lbound}$, without being so large as to ignore the model mismatch. As a rule of thumb $\bar{e}_{ubound}$ is set equal to twice $\bar{e}_{lbound}$.

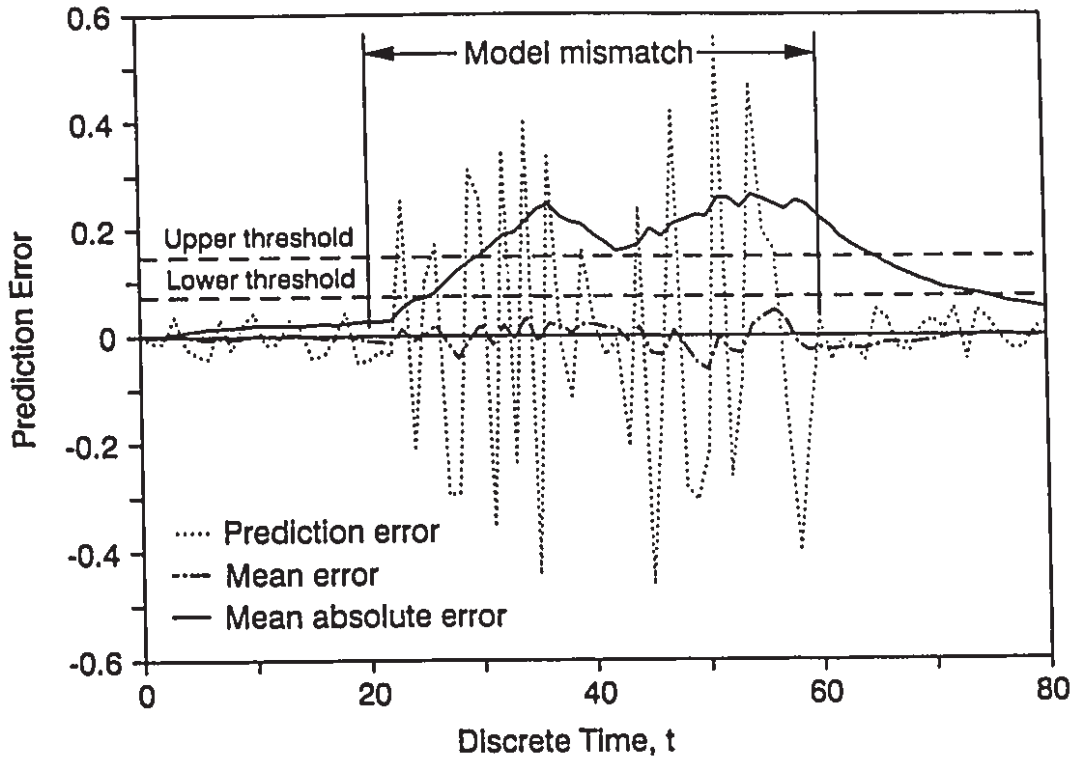

Figure 6.1 Comparison of the prediction error, mean error, and mean absolute error when subjected to model mismatch.

6.2.3 Generalized Predictive Control

The GPC design [62-64] minimizes the cost-function:

$$J(N1,\ N2,\ NU,\ \lambda) = \sum_{j=N1}^{N2} e^2(t+j) + \lambda \sum_{j=1}^{NU} \Delta x^2(t+j-1) \tag{6.3}$$

where $N1$ is the minimum costing horizon, $N2$ is the maximum costing horizon, NU is the control horizon, λ is the control weighting, $e(t) = d_{ref}(t) - d(t)$ is the depth error, and $d_{ref}(t)$ is the depth setpoint. To smooth the system's servo response $d_{ref}(t)$ is pre-filtered by $P(q^{-1}) = (1+p_1)/(1+p_1 q^{-1})$. The future predictions are given by:

$$\hat{\mathbf{d}} = \mathbf{G}\mathbf{x} + \mathbf{f} \tag{6.4}$$

with $\hat{\mathbf{d}} = [\hat{d}(t+N1), \hat{d}(t+N1+1), ..., \hat{d}(t+N2)]^T$, $\mathbf{f} = [f(t+N1), f(t+N1+1), ..., f(t+N2)]^T$, $\mathbf{x} = [\Delta x(t), \Delta x(t+1), ..., \Delta x(t+NU-1)]^T$, and $\mathbf{G}$ is the matrix of step weights with dimension $(N2-N1+1) \times NU$. $T(q^{-1}) = 1 + t_1 q^{-1}$ is a design polynomial used to improve robustness and limit the position command fluctuations. The free response predictions, $f(t)$, are obtained by convolving $T(q^{-1})/\Delta$ with $\{\tilde{d}(t+j)\}$, where:

$$\tilde{d}(t+j) = \Delta d(t+j)/T(q^{-1}) \quad \forall j \le 0, \tag{6.5}$$

$$\tilde{d}(t+j) = -\sum_{i=1}^{j} a_i \tilde{d}(t+j-i) + \sum_{i=0}^{j-1} b_i \tilde{x}(t+j-i) \quad \forall j \mid 1 \le j < N2 \tag{6.6}$$

$$\tilde{x}(t+j) = \Delta x(t+j)/T(q^{-1}) \quad \text{and} \tag{6.7}$$

$$\Delta x(t+j) = 0 \quad \forall j \mid 0 \le j < N2. \tag{6.8}$$

The position command which minimizes (6.3) is then given by:

$$\Delta x(t) = [1, 0, 0, ..., 0]^T (\mathbf{G}^T\mathbf{G} + \lambda \mathbf{I})^{-1} \mathbf{G}^T (\mathbf{d}_{ref} - \mathbf{f}) \tag{6.9}$$

where $\mathbf{d}_{ref} = [d_{ref}(t+N1), d_{ref}(t+N1+1), ..., d_{ref}(t+N2)]^T$ is the vector of future setpoints. For NU > 1, the matrix inversion can be efficiently computed using the recursive procedure described in [64].

While GPC's large number of tuning parameters ($N1$, $N2$, NU, λ, t_1, p_1) provide it with great control flexibility, they also make tuning GPC somewhat complex. The discussion which follows is based on the suggestions of Clarke *et al.* [62-64] and McIntosh *et al.* [65].

The minimum costing horizon, $N1$, should be set greater than or equal to the process deadtime. The maximum costing horizon, $N2$, must be greater than $N1$; and as $N2 \to \infty$ the controller is detuned and the closed-loop poles approach the open-loop poles. The "default" setting for the control horizon is $NU = 1$. When NU is increased

the control becomes more aggressive. In particular when $NU=N2-N1+1$ GPC becomes an "exact model-following" controller which cancels the process zeros and is therefore unsuitable for a non-minimum phase process. To keep the computations simple $N2$ and NU should be kept as small as possible. While a control weighting of $\lambda>0$ can be used to detune GPC and improve its robustness it is recommended that λ be set close to zero (a small value is necessary for numerical robustness). When a constant non-zero value of λ is used with adaptive GPC, the relative weighting of $e(t)$ and $\Delta x(t)$ in equation 6.3 can change, resulting in a variable closed-loop performance. $T(q^{-1})$ can be used to obtain a similar detuning effect as λ, while providing a consistent closed-loop performance. $T(q^{-1})$ effects only the regulation dynamics. $P(q^{-1})$ can then be used to independently tune GPC's servo response.

Based on these suggestions and the results of numerous computer simulations the tuning parameters: $N1=2$, $N2=3$, $NU=1$, $\lambda=0.0001$, $p_1=0.8$, and $t_1=0.5$ were selected for the deburring application. In Figure 6.2 a simulated response is shown for a deburring pass under adaptive GPC. A random sequence with a variance of 150 μm^2 was used for the disturbance $\xi(t)$. Contact was simulated by switching the process dynamics from the non-contact to the contact model. Because the contact model has a lower gain, the tool is momentarily pushed away from the edge at initial contact. To test the adaptive performance the model gain was initially set equal to 70% of the process gain. $\bar{e}_{lbound}=4.5$ μm, $\bar{e}_{ubound}=9$ μm, $\alpha=50$, and a forgetting factor of 0.99 were used with the RLS estimation. The estimator was shut-off within 0.5 s. After this point the model gain was within 3% of the process gain. The standard deviation of the depth was 15 μm.

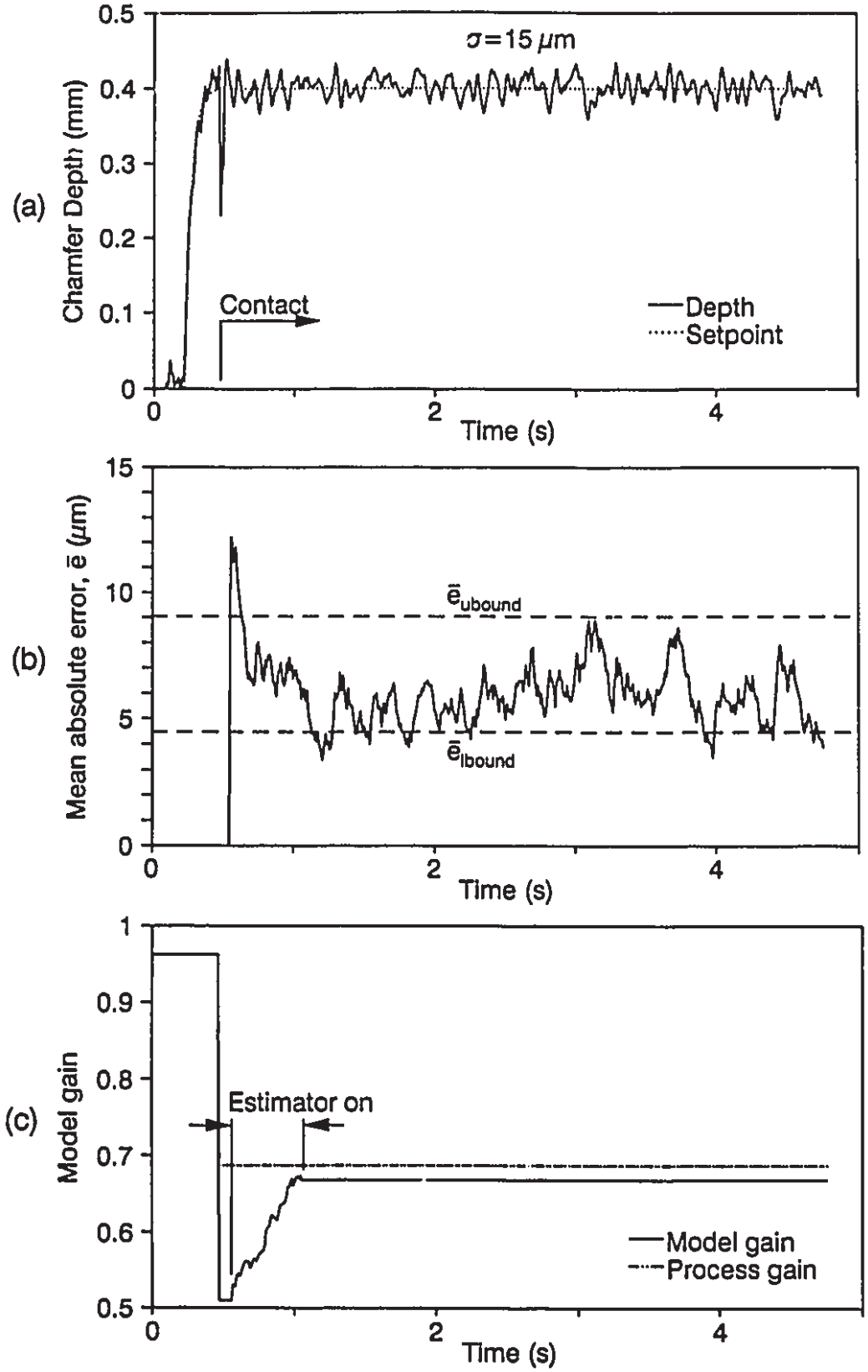

Figure 6.2 Simulated deburring pass under adaptive GPC. (a) Chamfer depth. (b) Mean absolute error. (c) Model gain.

6.3 LEARNING CONTROL: DESIGN AND VERIFICATION

6.3.1 Introduction

In iterative learning control schemes the system inputs are modified over a sequence of repetitions or trials with the objective that the system outputs converge to a predetermined reference trajectory. Ideally the convergence should be guaranteed even for the case of controlling a nonlinear, time-varying system, with minimal system knowledge. Research in this area began with the independent proposal of the technique by different researchers, including Arimoto *et al.* [44] and Craig [45], and continues to be active. These schemes are applicable to processes which are repetitive in nature and operate over a fixed time interval, such as mechanical systems in a manufacturing environment, or batch process control. Learning control differs from conventional adaptive control in that the learning is performed off-line between trials, and the controller parameters are typically fixed. Often learning control is proposed as an alternative to adaptive feedback control. Here a new iterative learning control algorithm will be developed as an addition to GPC's adaptive feedback control. The development and example application of the general form of the algorithm will be described first. This is followed by the development of an alternate version of the algorithm for the deburring case.

6.3.2 Development of the New Learning Algorithm

The new learning algorithm termed GPC with Learning (GPCL) improves the regulation performance of GPC by learning and compensating for the repeatable portion of the disturbance $\xi(t)$. In this development the arguments t and q^{-1} will be omitted for clarity. ξ is modelled as the sum of two independent, uncorrelated

random sequences:

$$\xi_k = m + v_k \tag{6.10}$$

where the subscript k indicates the trial number. The sequence $\{m\}$ is taken to be repeatable over the series of trials, while $\{v\}$ is random throughout. The estimate of the disturbance is obtained from the CARIMA model:

$$A\,\Delta y_k = q^{-1} B\,\Delta u_k + \xi_k \tag{6.11}$$

as:

$$\xi_k^* = A\,\Delta y_k - q^{-1} B\,\Delta u_k \tag{6.12}$$

where y_k is the process output, and u_k is the process input. The future disturbances are then predicted by the averaging from the previous passes:

$$\hat{\xi}_k(t+j) = \left(\sum_{i=0}^{k-1} \xi_i^*(t+j) \right) / k \qquad \forall k > 0 \tag{6.13}$$

and $\hat{\xi}_0(t+j) = 0$. GPCL is obtained from GPC by replacing equation 6.6 with:

$$\tilde{y}(t+j) = -\sum_{i=1}^{j} a_i\,\tilde{y}(t+j-i) + \sum_{i=0}^{j-1} b_i \tilde{u}(t+j-i) + \hat{\xi}^f(t+j) \qquad \forall j \mid 1 \le j < N2 \tag{6.14}$$

where $\hat{\xi}^f(t+j) = \hat{\xi}(t+j)/T$. $\hat{\xi}(t+j)$ must be filtered by $1/T$ to maintain the relationship between y, u, and ξ given by the CARIMA model (equation 6.11). In GPC the unknown future disturbances were estimated as $\hat{\xi}(t+j) = 0$, which is the minimum-variance prediction for a zero mean uncorrelated random sequence. If any portion of this disturbance is repeatable from trial to trial, GPCL learns and adds this information to GPC, resulting in improved prediction and regulation. Since this modification only adds a feedforward term to GPC, the stability properties of GPC are unaffected.

To obtain the convergence properties of GPCL the variances of y_k and Δu_k will be examined as $k \to \infty$. The estimates are first rewritten as:

$$\hat{\xi}_k(t) = m(t) + \epsilon_k(t) \tag{6.15}$$

From equation 6.13 it can be seen that $\{\epsilon_k\}$ is dependent on past values of $\{v_k\}$, and is independent of $\{m\}$ and $\{v_k\}$, so that:

$$\mathrm{E}\{\hat{\xi}_k^2(t)\} = \sigma_m^2 + \sigma_\epsilon^2 \tag{6.16}$$

From the central limit theorem and the reproductive property of the normal distribution:

$$\mathrm{E}\{\hat{\xi}_k^2(t)\} = \sigma_m^2 + \sigma_v^2/k \qquad \forall k > 0 \tag{6.17}$$

Combining (6.16) and (6.17) gives:

$$\sigma_\epsilon^2 = \sigma_v^2/k \qquad \forall k > 0 \tag{6.18}$$

GPCL was then converted into the transfer function form:

$$Tw = R\Delta u_k + Sy_k + H\hat{\xi}_k \tag{6.19}$$

Details of this conversion are given in Appendix D. Since the concern here is regulation and not servoing, a constant setpoint w is assumed. Combining equations 6.11 and 6.19, and simplifying:

$$G_c y_k = R\xi_k - q^{-1}HB\hat{\xi}_k \tag{6.20}$$

$$G_c \Delta u_k = -S\xi_k - HA\Delta\hat{\xi}_k \tag{6.21}$$

where $G_c = RA\Delta + q^{-1}SB$ is GPCL's characteristic polynomial. Substituting ξ_k from (6.10) and $\hat{\xi}_k$ from (6.14) gives for y_k:

$$G_c y_k = R(m + v_k) - q^{-1}HB(m + \epsilon_k) \tag{6.22}$$

$$G_c y_k = G_{yv} v_k + G_{ym} m + G_{y\epsilon} \epsilon_k \tag{6.23}$$

where $G_{yv} = R$, $G_{ym} = R - q^{-1}HB$, and $G_{y\epsilon} = -q^{-1}HB$. Similarly for Δu_k:

$$G_c \Delta u_k = -S(m+v_k) - HA\Delta(m+\epsilon_k) \tag{6.24}$$

$$G_c \Delta u_k = G_{uv} v_k + G_{um} m + G_{u\epsilon} \epsilon_k \tag{6.25}$$

where $G_{uv} = -S$, $G_{um} = -S - HA\Delta$, and $G_{u\epsilon} = -HA\Delta$. Given that $\{v_k\}$, $\{m\}$, and $\{\epsilon_k\}$ are independent, the variances σ_y^2 and $\sigma_{\Delta u}^2$ are:

$$\sigma_y^2 = K_{yv}\sigma_v^2 + K_{ym}\sigma_m^2 + K_{y\epsilon}\sigma_\epsilon^2 \tag{6.26}$$

$$\sigma_{\Delta u}^2 = K_{uv}\sigma_v^2 + K_{um}\sigma_m^2 + K_{u\epsilon}\sigma_\epsilon^2 \tag{6.27}$$

Substituting σ_ϵ^2 from equation 6.17 and recalling that $\hat{\xi}_0(t+j)=0$ gives:

$$\sigma_y^2 = K_{yv}(\sigma_v^2 + \sigma_m^2) \qquad \forall k=0 \tag{6.28}$$

$$\sigma_y^2 = K_{yv}\sigma_v^2 + K_{ym}\sigma_m^2 + K_{y\epsilon}\sigma_v^2/k \qquad \forall k>0 \tag{6.29}$$

$$\sigma_{\Delta u}^2 = K_{uv}(\sigma_v^2 + \sigma_m^2) \qquad \forall k=0 \tag{6.30}$$

$$\sigma_{\Delta u}^2 = K_{uv}\sigma_v^2 + K_{um}\sigma_m^2 + K_{u\epsilon}\sigma_v^2/k \qquad \forall k>0 \tag{6.31}$$

where the K values are the variance gains. Note that when $k=0$ no learning has taken place so GPCL's performance is identical to GPC's. The variance of a filtered uncorrelated random sequence can be obtained by integrating the spectral density of the filter's transfer function [66]. The variance gains can therefore be obtained by integrating the spectral density of their associated transfer functions in equations 6.23 and 6.25. For example:

$$K_{yv} = \frac{1}{2\pi i} \oint \frac{G_{yv}(z)G_{yv}(z^{-1})}{G_c(z)G_c(z^{-1})} \frac{dz}{z} \tag{6.32}$$

where $z = exp(i\omega)$. The method for evaluating this integral is given in [66].

Clearly, from equations 6.29 and 6.31 σ_y^2 and $\sigma_{\Delta u}^2$ converge asymptotically as $k \to \infty$, for finite σ_m^2, σ_v^2, and K values.

GPCL is distinct from the typical iterative learning control schemes described in the introduction in several ways. GPCL requires considerable system knowledge

in that a process model is required. While it is not applicable to any nonlinear process, it is applicable to processes which can be locally linearized about an operating point (which is often the case). Unlike typical learning controllers the reference trajectory may be changed over the series of trials. Typically learning controllers are based on purely deterministic analysis, with GPCL the stochastic part of the disturbance was considered explicitly. Lastly GPCL is an addition to GPC's adaptive feedback control, rather than an alternative to it.

6.3.3 Application Example

Non-contact edge following experiments were performed to demonstrate the general form of GPCL. In industry, robotic welding, gluing, and light finishing can be considered as non-contact edge or surface following applications. Prior to the experiments, the effect of GPC's tuning parameters on its theoretical performance will be examined.

This theoretical analysis is based on the non-contact CARIMA model given in section 6.2.2. Of GPC's set of tuning parameters $N1$, λ, and p_l will not be considered, since the process deadtime is unchanged and GPCL is concerned with regulation. This leaves the parameters $N2$, NU, and t_l. The effect of these parameters on GPCL's variance gains is given in Table 6.1. From equations 6.28-6.31 it can be seen that the gains ($K_{y\varepsilon}$, $K_{u\varepsilon}$) determine the rate of convergence of GPCL, while (K_{yv}, K_{uv}) indicate the contribution of GPC's feedback loop, and (K_{ym}, K_{um}) determine GPCL's steady state performance (as $k \to \infty$). It is desirable to have the ability to detune GPC's feedback loop for improved robustness without affecting GPCL's

feedforward loop (which has no effect on stability). From case's 1 and 2 it can be seen that increasing $N2$ has a greater detuning effect on GPCL than on GPC and is therefore undesirable. It was found that as $N2 \rightarrow \infty$, H becomes a D.C. pass filter, and since $\hat{\xi}$ has a zero mean, GPCL's feedforward term has no effect. From case's 2 and 3 it can be seen that increasing NU increased the aggressiveness of GPCL more than GPC. The desired detuning of GPC with minimal effect on GPCL was achieved using the design polynomial T. Comparing case 4 to case 1 it can be seen that with $t_1 = 0.3$ GPC's input variance gain (K_{uv}) was reduced 51%. At the same time GPCL's output variance gains were virtually unaffected. K_{ym} was unchanged, and $K_{y\epsilon}$ was increased by just 4%. Case 4's tuning, along with $N1 = 2$ and $p_1 = 0.8$, were used for the edge following experiments.

The experiments were performed with the new AEE mounted on a PUMA-762 robot. The robot was used to repeatedly move the tool along a straight part edge. The position measurement and tool motion were performed by the AEE, controlled by the 80486 microcomputer at a rate of 105 Hz. The length of each trial was 640 samples, or 6.1 s. The experimental values of the input and output variances measured over ten 11 trial experiments are compared to computed values in Figure 6.3. The computed values were obtained by first using equations 6.28-6.31 and the experimental input and output variances to estimate σ_m^2 and σ_v^2. The mean values of these estimates were then substituted back into equations 6.28-6.31 to obtain the computed values. With k=0, which is equivalent to GPC, the average σ_y^2 value was 225 μm^2. After just 3 trials (k=3) this was reduced 32% to 154 μm^2. After 10 trials the reduction was 43% (129 μm^2). Given that, based on the σ_w^2 and σ_v^2 values

(estimated as 53 μm^2 and 60 μm^2 respectively), the disturbance was only 47% repeatable this result is quite impressive. A sample result showing both the servoing and regulation performance of GPCL is shown in Figure 6.4. Here it can be seen that GPCL greatly reduced the following error during both servoing and regulation.

Case No.	Tuning	Variance Gains					
	$(N2, NU, t_l)$	K_{yv}	K_{ym}	$K_{y\epsilon}$	K_{uv}	K_{um}	$K_{u\epsilon}$
1	(3, 1, 0)	1.85	0.10	1.72	1.15	1.15	2.04
2	(4, 1, 0)	1.88	0.38	1.87	0.78	0.40	1.11
3	(4, 2, 0)	1.83	0.03	1.77	2.70	4.05	6.76
4	(3, 1, 0.3)	1.93	0.10	1.79	0.56	1.15	1.53

Table 6.1 Effect of the tuning parameters $(N2, NU, t_l)$ on GPCL's variance gains for the edge following application.

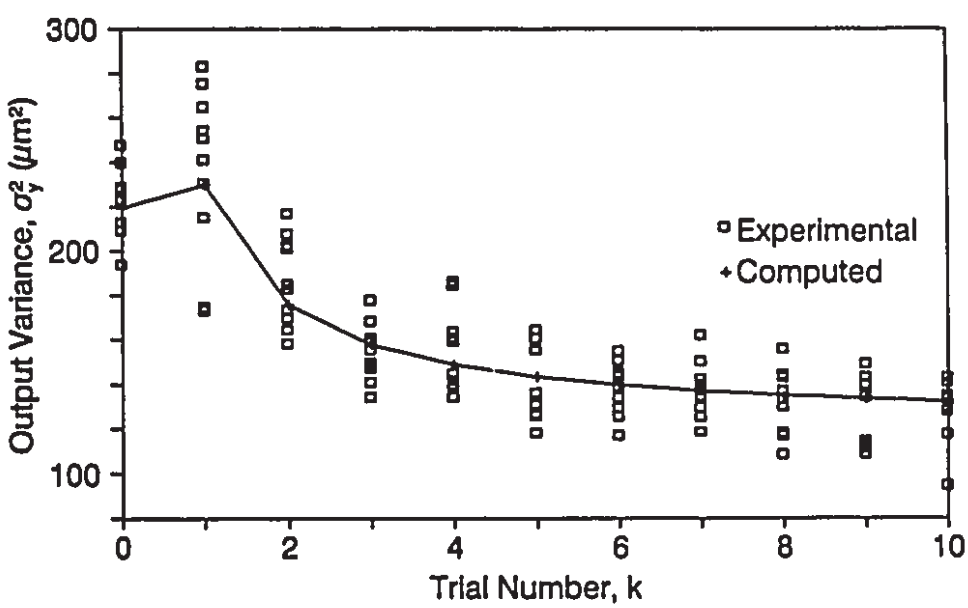

Figure 6.3a Experimental and computed output variances over 11 trials for the edge following application under GPCL.

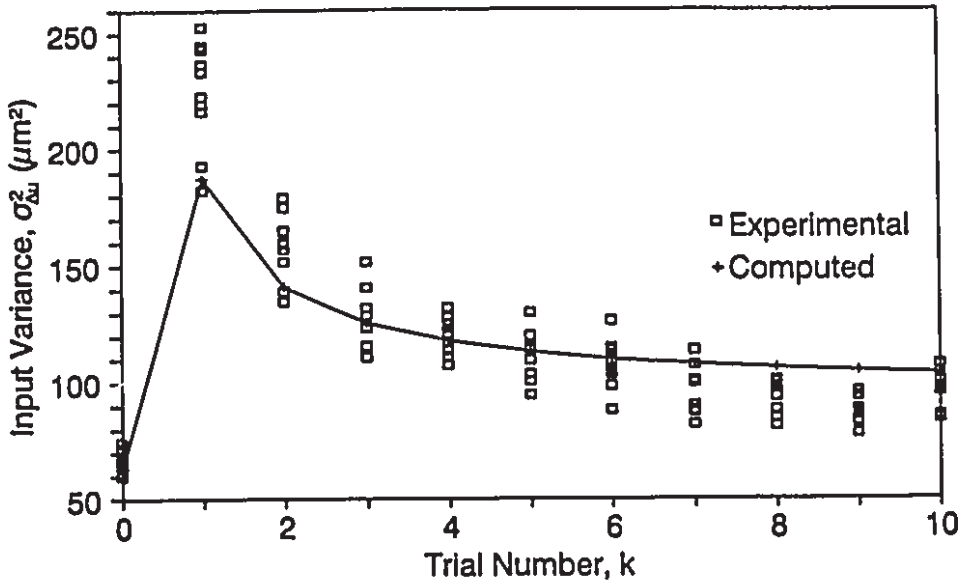

Figure 6.3b Experimental and computed input variances over 11 trials for the edge following application under GPCL.

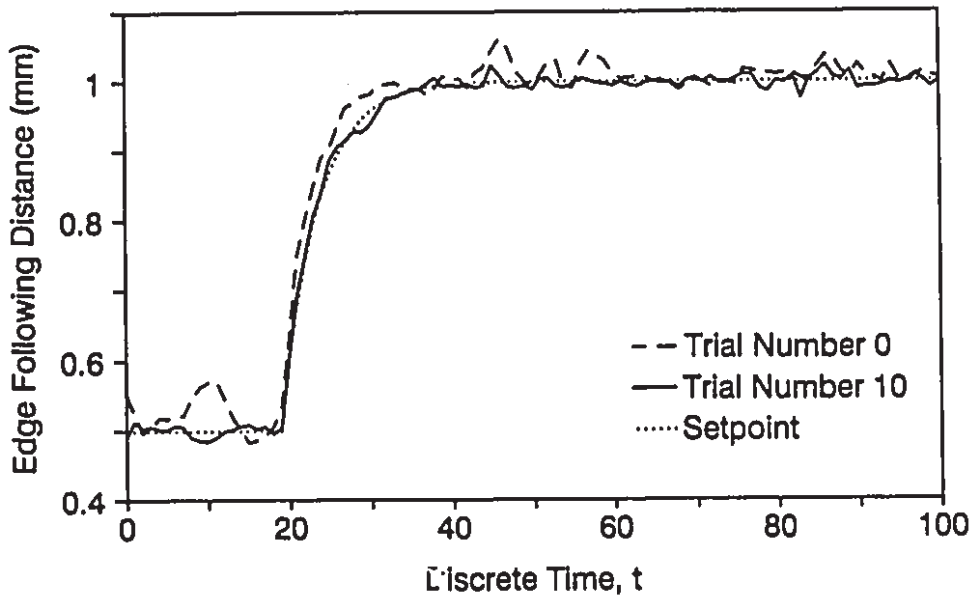

Figure 6.4 Sample edge following response under GPCL.

6.3.4 Learning Algorithm for Robotic Deburring

As just shown, depending on the repeatability of the disturbance, GPCL requires several trials before it outperforms GPC. When deburring under tight

tolerance specifications the parts produced in the initial trials could be unacceptable. An alternate form of GPCL was developed for deburring to avoid this problem. With the alternate form the learning takes place during several non-contact learning passes, rather than while the deburring is being performed. The learning passes are performed with the tool 1-3 mm away from the part edge. Since there is no control being performed, the variations in the tool position are the result of robot and part positioning errors only. When deburring is performed these variations plus the AEE's position correction give the tool's undeflected position. The new free response predictions are therefore obtained by replacing equation 6.7 in GPC with:

$$\bar{x}(t+j) = [\Delta x(t+j) + \Delta d^{*}(t+j+t_s)/G_x(q^{-1})]/T(q^{-1}) \qquad (6.33)$$

where $d^{*}(t)$ is the tool position averaged over NK learning passes, t_s is the sensor delay, and $G_x(q^{-1})$ is the transfer function of the end effector's position servo. The difference between this form and standard GPCL is that here the disturbance acts at the process input, whereas in standard GPCL the disturbance acts at the process output. Since the bandwidth of the AEE is 65 Hz and the frequency range of $d^{*}(t)$ was determined to be 0-15 Hz, $G_x(q^{-1})$ will be modelled as a unity gain. The sensor delay from the vision sensor is equal to 1 sample period.

A simulated response for adaptive GPCL, using the same settings as used for GPC, with $t_s=1$, $NK=\infty$, and a 2/3 repeatable disturbance ($\sigma_v^2=50$ μm^2, and $\sigma_m^2=100$ μm^2), is shown in Figure 6.5. The depth's standard deviation of 9 μm is 72% of GPC's value. With a 100% repeatable disturbance this value is reduced to 2 μm (15%).

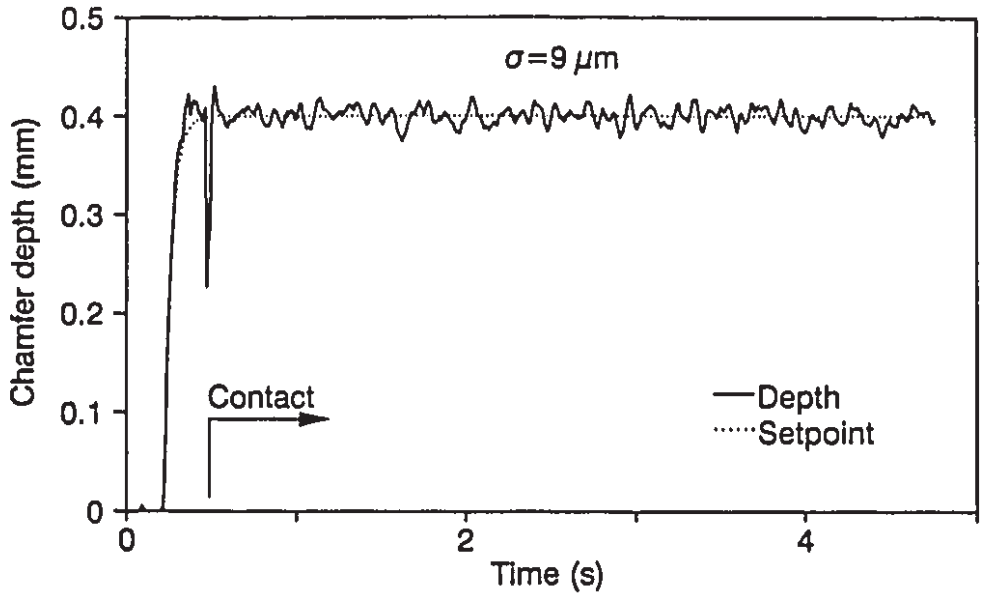

Figure 6.5 Simulated chamfer depth response for adaptive GPCL.

6.4 CONCLUSIONS

6.4.1 Adaptive Predictive Control

GPC was chosen as the control algorithm for the chamfer depth. GPC is an extension of the GMV and EH control algorithms successfully applied to the force control problem in Chapter 4. The GPC design is based on a CARIMA type process model. To control the deburring operation three process models are used alternately. One non-contact model for use during the initial approach, and two contact models (for use with $d_v(t)$ and $d_f(t)$). To adapt to changes in dynamics the parameters of both contact models are estimated on-line using RLS. A comparison of the RLS prediction error, mean error, and mean absolute error concluded that the mean absolute error was the most suitable index for monitoring the estimation. The estimator is shut-off and reset by monitoring the mean absolute error with two thresholds, to provide hysteresis and a deadband. This scheme reduces the possibility of frequent resetting, which can occur with a single threshold.

Computer simulations including a stochastic disturbance were performed to test GPC's adaptive performance. The model gain was initially set equal to 70% of the process gain. Within 0.5 s the estimator was shut-off and the gain error was just 3%. The standard deviation of the depth was 15 μm.

6.4.2 Learning Control

A new iterative learning control algorithm, GPCL, was developed as an addition to GPC's feedback control. GPCL was first developed in a form suitable for any process which can be modelled with a CARIMA model, and is performed repeatedly. It improves the regulation performance of GPC if any portion of the disturbance is repeatable over the series of trials. Because GPCL only adds a feedforward term to GPC, GPC's stability properties are unaffected. GPCL was shown theoretically to converge asymptotically as the number of trials approaches infinity. It was then verified experimentally in a non-contact edge following application. After just 3 trials the average output variance was reduced 32% in comparison to GPC. After 10 trials the reduction was 43%. Considering that the disturbance was only 47% repeatable this result is quite impressive.

Because the relatively poor performance of GPCL during the initial trials could produce unacceptable parts when deburring, an alternate form of GPCL was developed for the deburring application. With this alternate form the learning takes place during several non-contact learning passes, rather than during the deburring operation. In a simulation using the same settings as GPC and 2/3 repeatable disturbance the depth's standard deviation was 9 μm, 72% of GPC's value. With a 100% repeatable disturbance the standard deviation was 2 μm.

CHAPTER 7

DEPTH CONTROL EXPERIMENTS

7.1 INTRODUCTION

In this chapter, depth controlled deburring experiments are performed on straight edged, and planar parts. The experimental setup is first described, followed by discussions on the results of deburring and inspection system tests, and conclusions [67, 68].

7.2 EXPERIMENTAL SETUP

7.2.1 System Structure

The system structure is shown in Figure 7.1. The user first communicates with the system supervisor to initiate a deburring and/or inspection operation. The user may then enter the AEE controller parameters, or use a set of default values. The supervisor then coordinates the robot and AEE controllers. The results of the deburring/inspection operation(s) are reported to the user, and may be stored in a log file for further analysis. The operation of the system supervisor is further detailed in section 7.2.3. The robot program employs a trajectory generator, described in section 7.2.4, to generate the robot's motion.

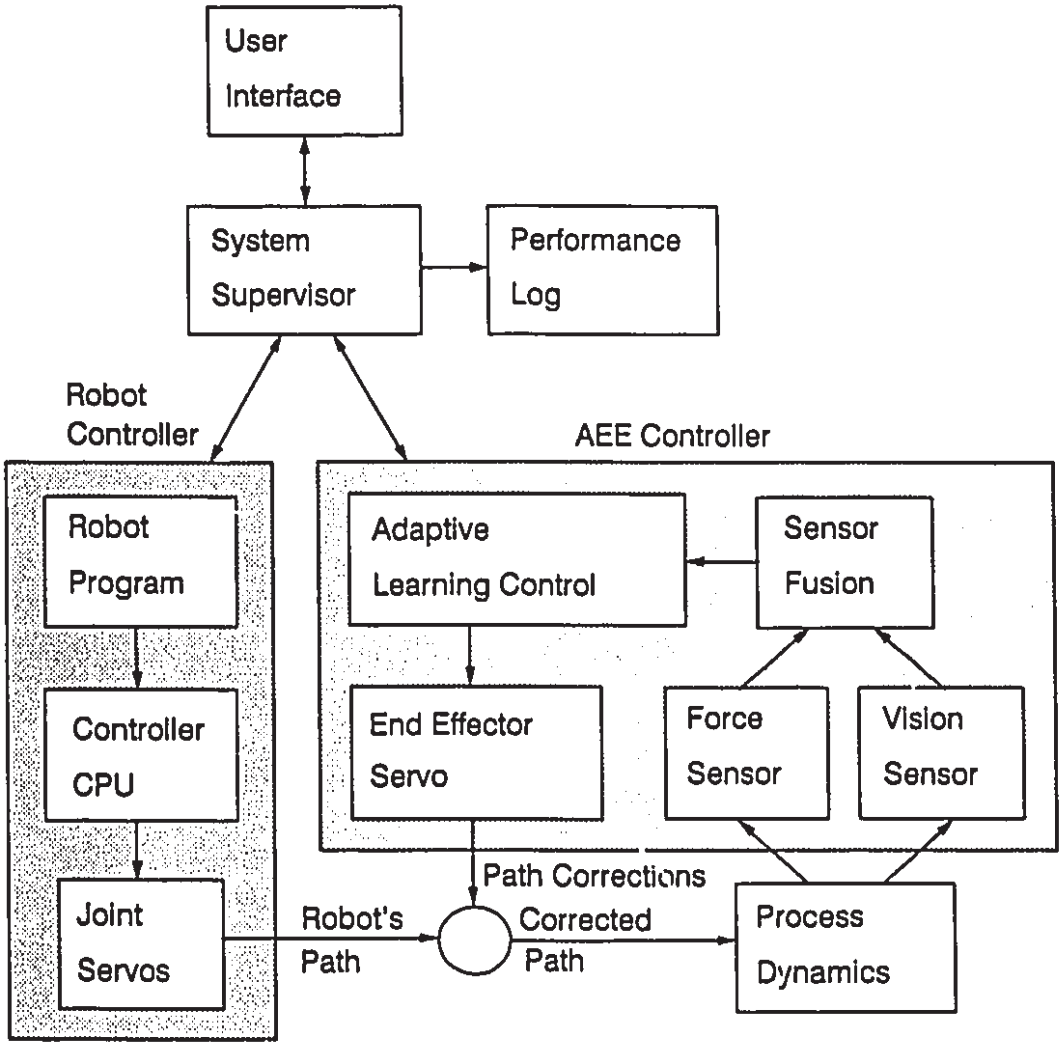

Figure 7.1 Structure of the robotic deburring system.

7.2.2 Hardware Description

The hardware consists of the AEE and its associated hardware (its motion controller, force sensor hardware, and vision sensor hardware), a PUMA-762, six-axis, industrial robot, and a 33 MHz 80486 microcomputer. The PUMA-762 was chosen over the PUMA-560 (used for the force control experiments in Chapter 4) because its higher stiffness and payload capacity allow it to move the AEE faster, and more accurately. The user interface, system supervisor, and AEE controller functions are

performed by the 80486 microcomputer, programmed in C. Of these functions, the controller is the most computationally demanding. The controller samples the force signal; receives the depth measurement, and sensor status from the vision SBC; and computes, and sends the position command to the AEE servo; all at a rate of 105 Hz.

7.2.3 System Supervisor

The system supervisor is responsible for communicating with the user, coordinating the robot and AEE controllers, logging the system's performance, and error handling.

The supervisor has a menu-driven interface for user I/O. Communication to the robot controller is performed using the PUMA's SUPERVISORY interface. This allows commands to be sent from the supervisor and executed as if they had been entered at the robot's keyboard. Communication from the robot controller is done using one of the robot's external output relays to provide a digital signal. To begin a deburring/inspection operation the supervisor commands the robot to execute the deburring/inspection program. When the robot has moved to the starting point of the tool path a ready signal is sent to the supervisor. The AEE controller is then activated, and operates until the ready signal is turned off, or an error is detected. If there was no error the results are displayed to the user, who can then log them in a datafile, and/or choose to continue with a further operation. If any errors are detected the AEE controller is deactivated, and the tool is immediately backed out 5 mm from it's current position. This action is designed to prevent any collisions from taking place between the tool and part as the robot completes it's motion. This is of

particular importance if the error resulted from an excessive force being applied to the tool (from too large a depth of cut or a tool/part collision). The error detected and appropriate troubleshooting action are then reported to the user. It is then up to the user to carry out the action and restart the deburring system. In Table 7.1 the errors detected, method of detection, and troubleshooting advice, are listed.

7.2.4 Test Part Design and Manufacture

The deburring system will be tested on straight edged and planar parts. The planar parts will be made up of combinations of linear and circular edge segments, as are most industrial parts. It should be noted here that the deburring system is capable of deburring more complex parts, however the facilities required to manufacture such parts were unavailable.

The test parts were machined on a 2½-axis CNC milling machine. The majority of the parts were made out of 1018 steel. A few parts were made of 304 stainless steel to evaluate the system's performance with a harder to machine material. Burrs with an average height of 0.2 mm were created on the part edges by finish milling with a dull cutter. The planar part designs are shown in Figure 7.2. Designs 1 and 2 test the systems ability to follow 90° corners with fairly small radii. With design 3, the edge includes several sharp corners, and a semi-circular segment.

Error Detected	Method of Detection	Troubleshooting Advice
Excessive Tool Force	Force measurement exceeds a threshold value (15 N).	Check tool and part for damage and replace damaged item(s). Check the robot's motion program, and force sensor operation, prior to restarting.
Force Sampling Timeout	A timeout occurs waiting for a trigger from the vision sensor (used to initiate sampling).	Check that the vision sensor's power supply is on. Check the physical connection between the external trigger input and the vision sensor. Restart.
Vision/Inspection Failure	A timeout occurs waiting to receive data from the vision SBC, or an invalid sensor status value has been read.	Check the physical connections between the vision SBC and the microcomputer. Re-load the vision/inspection software onto the SBC, and restart.
SUPERVISORY Interface Open Failure	Interface device driver is not found resident in the microcomputers memory.	Load the SUPERVISORY interface device driver and restart.
SUPERVISORY Interface Timeout	A timeout occurs waiting to send a command via the interface.	Check the SUPERVISORY interface's physical connection. Ensure that the interface software has been enabled on the PUMA. Restart.

Table 7.1 List of errors detected, method of detection, and troubleshooting advice provided by the system supervisor.

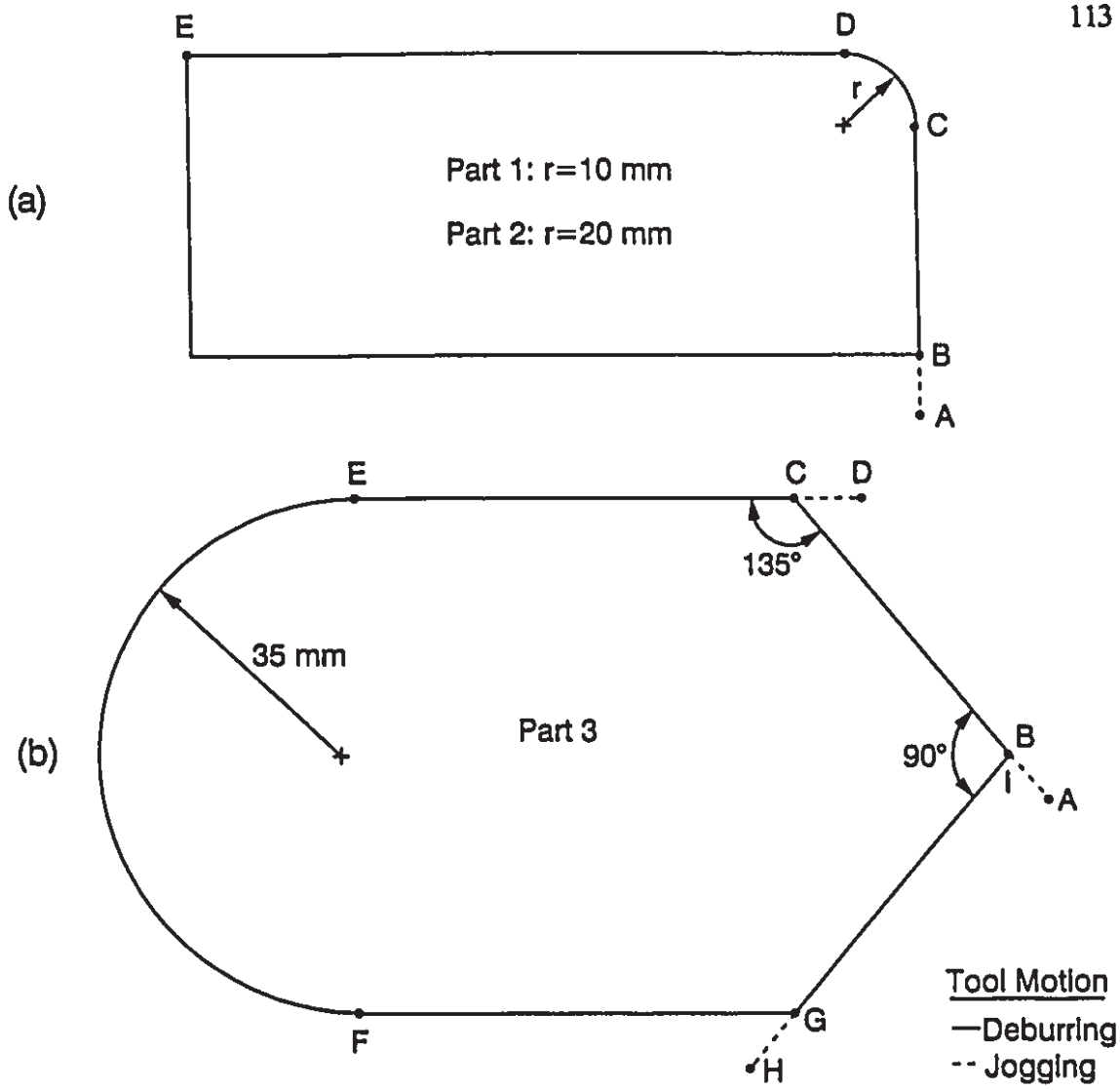

Figure 7.2 Planar test part designs and their associated tool paths for deburring. (a) Designs 1 and 2. (b) Design 3.

7.2.5 Robot Trajectory Generator

The PUMA-762's internal trajectory generator is limited to linear motion over which the user has no precise control of the speed. To deburr the planar parts a constant speed (feedrate) and circular motion are required. It was therefore necessary to develop a trajectory generator for the PUMA robot. The generator was programmed in the PUMA's native language, Unimation's VAL-II. Due to VAL-II's

limited execution speed, the planning was performed off-line, and the results stored. The stored trajectory was then executed using the internal form of the VAL-II ALTER command, which allows full control of the robot's motion.

The deburring tool paths for the planar parts are shown in Figure 7.2. The tool motion proceeds from points A-E (designs 1 and 2), and points A-I (design 3). For the linear segments the tool will be oriented such that its motion axis is perpendicular to the edge, and produces a 45° chamfer. The sharp corners of design 3 (points C and G) require the AEE to be rotated instantaneously. This is impossible in practice, so the cut will instead be exited and re-entered. Because these jogging motions (C-D-C and G-H-G) are short they have little effect on the total cycle time. The rotation will take place during the motions C-D and G-H. To limit the angular acceleration, which was found experimentally to excite the robot's structural dynamics, the rotation angle was low-pass filtered using a 1 Hz FIR filter (20th order, Hamming window). While it is less computationally efficient than an IIR filter, the FIR filter was used because it allowed the filtering to be performed without adding delay to the rotation.

If the vision sensor is used with the standard orientation during a circular segment it will produce an incorrect measurement, because the sensor measures the position a distance D ahead of the tool. This is the main reason why this distance was minimized when designing the vision sensor. As shown in Figure 7.3 the offset error, ϵ, can be eliminated by leaning the tool into the curve by an angle δ. This angle can be obtained from simple trigonometry as:

$$\delta = sin^{-1}(D/2r) \tag{7.1}$$

Given $D = 12$ mm from Chapter 5, for designs 1-3 δ equals 37°, 18°, and 10°

respectively. Because this rotation must be performed quickly at the start and end of each circular segment, large rotations are difficult. Given this fact, and the relatively short length of the curved segments for designs 1 and 2, it was decided that this rotation will only be performed with design 3. The angle will be FIR filtered as before to both reduce the angular acceleration, and to smooth the transition between the linear and circular segments. Because the vision sensor's angle of incidence (α in Chapter 5) is altered by δ, a new set of calibration constants had to be obtained and used during the circular segment. On designs 1 and 2 the force sensor and the standard orientation will be used during the circular segments.

For the inspection operation the tool will be programmed to follow the part approximately 1 mm from the edge. Again, because of the lead distance D, a special trajectory must be used with the circular segments. This is illustrated in Figure 7.4. The tool moves from points A-B. To obtain the depth measurement during the corner the tool is positioned and oriented so that it is perpendicular to the edge a distance D ahead.

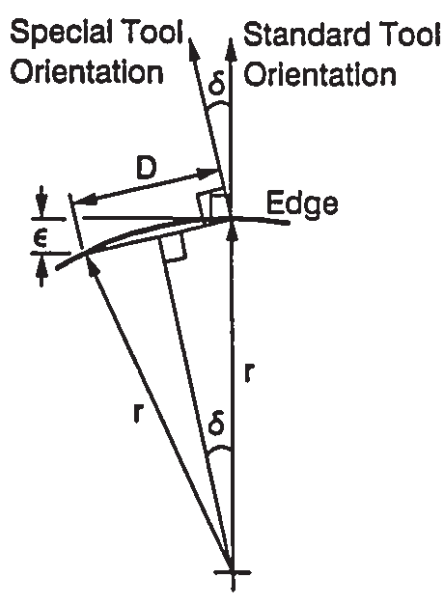

Figure 7.3 Special tool orientation for circular edge segments.

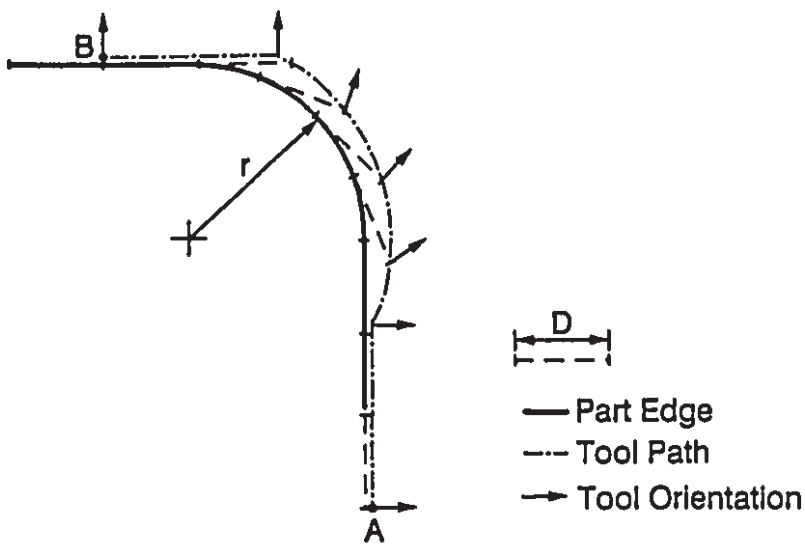

Figure 7.4 Tool path and orientation for inspection of an edge with linear and circular segments.

7.3 DEBURRING TEST RESULTS AND DISCUSSION

The deburring tests were performed using the same control parameters as used in the simulations in Chapter 6, except for the number of learning passes, *NK*. Since time was not critical, in the simulations *NK* was set to a very large value to get maximum benefit from the learning passes. In practice *NK* should be set to a fairly small value to minimize the time required for learning. In the non-contact edge following results in section 7.3.3 , there was significant improvement in regulation after just 3 learning passes, so *NK*=3 will be used in these tests. The depth setpoint=0.4 mm, feedrate=25 mm/s, and the parts are 1018 steel unless otherwise noted.

The depth response for a straight edged part deburred under non-adaptive GPC is shown in Figure 7.5. Note that at initial contact the tool was pushed away from the edge much less than predicted by the simulation results. In practice, as the tool entered the cut the change in dynamics was gradual (unlike the simulation) so

the control was less adversely affected. The standard deviation of the depth measurement, σ, was 15 μm. The pattern of sensor fusion for this result, and the remainder of the results, is the same as in the scenario described in Chapter 5, section 5.3, except that here vision failure occurred sporadically during each pass. With adaptive GPC, as shown in Figure 7.6, the regulation performance just after contact is worse than non-adaptive's, but after a delay of about 0.4 s the performance is clearly superior. σ was 9 μm, 60% of the non-adaptive value. The poor initial performance is a result of the initial transient behaviour of the parameter estimation. As illustrated for adaptive GPCL in Figure 7.7(c), during this period the mean absolute prediction error is reduced from an initially large value, which would account for the poor performance. With adaptive GPCL σ was 6 μm, 67% of adaptive GPC's value. This improvement in performance is comparable to the simulation results. As it did in the simulations, the supervision scheme for the estimator successfully avoided the problem of frequent resetting (i.e. frequent stoping and restarting of the estimation). The model gain varied from about 0.65-0.58 (Figure 7.7(b)). For the gain k_f (used to obtain a depth estimate from the force in the sensor fusion scheme) the estimation was less active than for the process model, and the gain was 0.087 mm/N for most of the cut (Figure 7.7 (d)). The average tool position from the learning passes, d^*, provides a measurement of the robot and part positioning errors. Here the standard deviation of d^* was 0.041 mm (Figure 7.7(e)).

The depth and model gain results for deburring a 304 stainless steel straight edged part under adaptive GPCL are given in Figure 7.8. The depth regulation was somewhat worse (σ=9 μm) than with 1018 steel, probably because of the lower

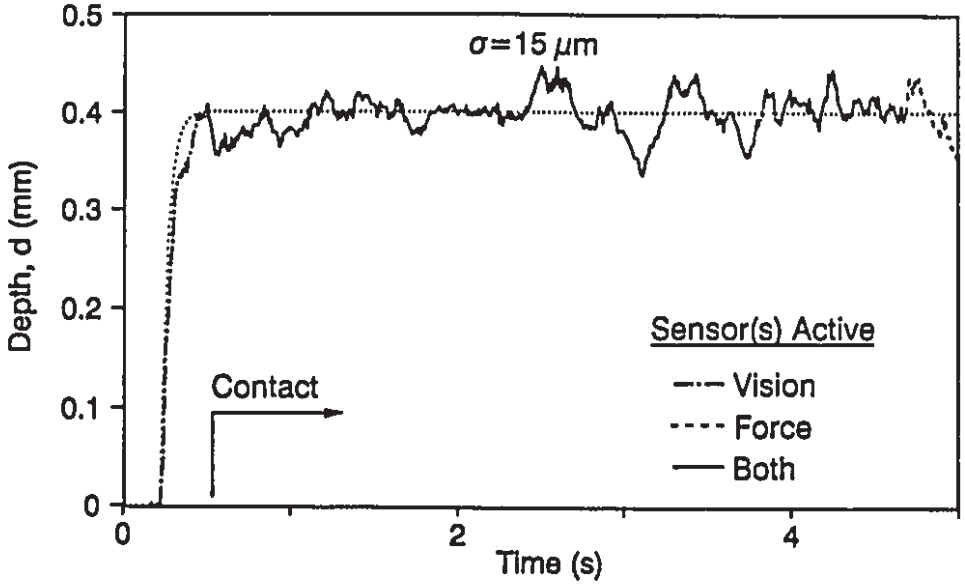

Figure 7.5 Depth response for a straight edged part deburred under non-adaptive GPC.

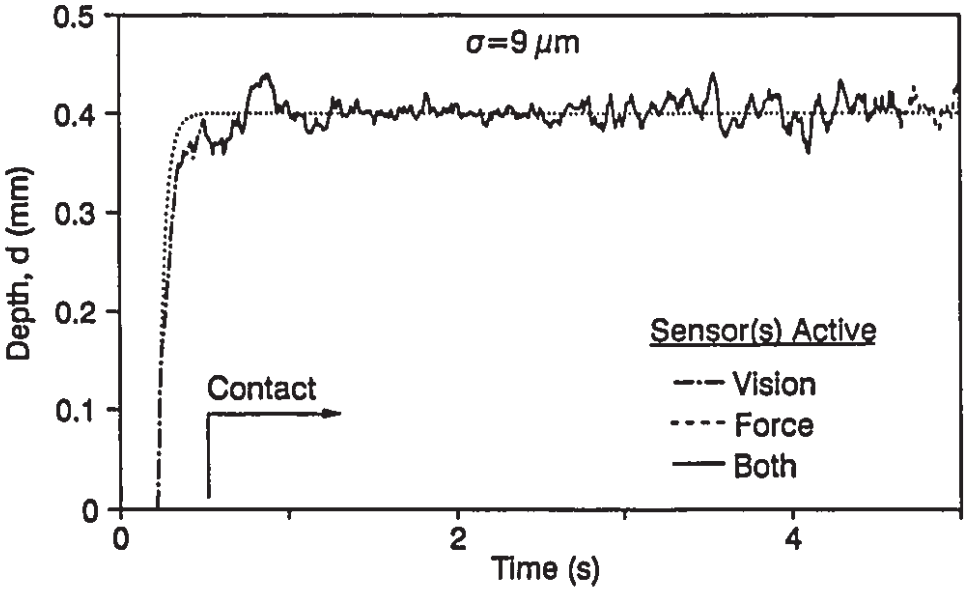

Figure 7.6 Depth response for a straight edged part deburred under adaptive GPC.

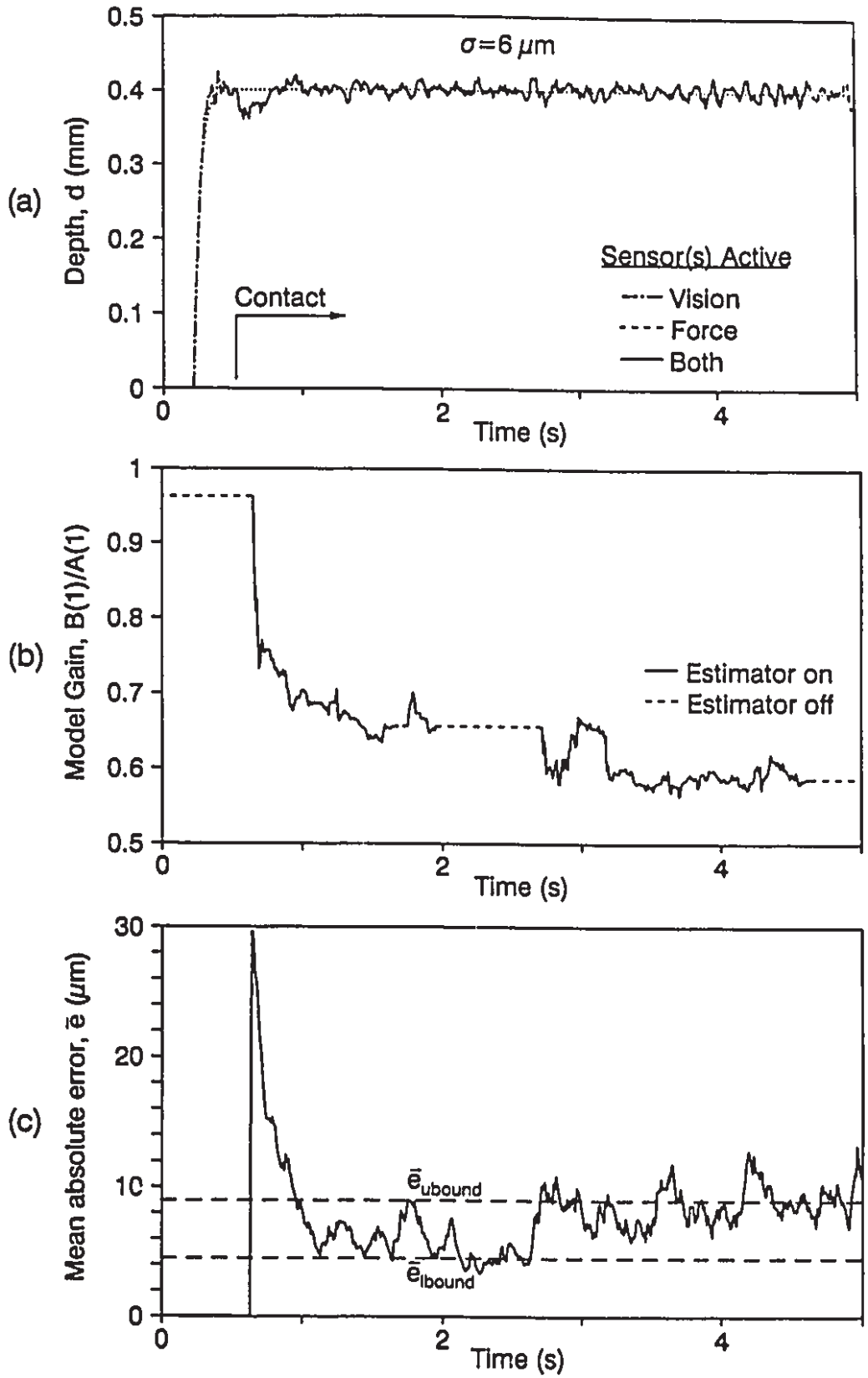

Figure 7.7a Test results for a straight edged part deburred under adaptive GPCL.

(a) Depth, *d*. (b) Model gain, *B(1)/A(1)*. (c) Mean absolute prediction error, $\bar{e}$.

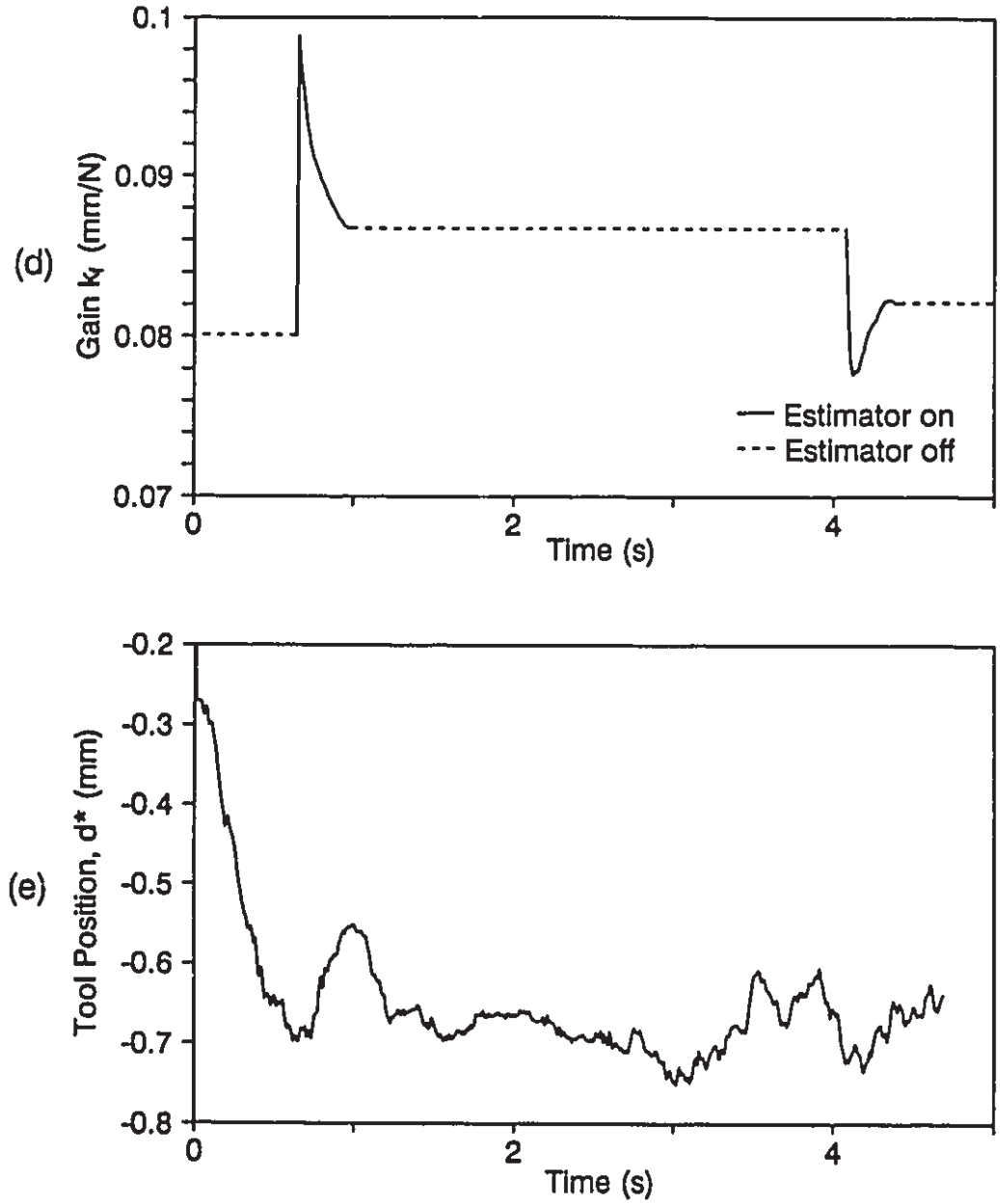

Figure 7.7b Test results for a straight edged part deburred under adaptive GPCL. (d) Gain k_f. (e) Average tool position from learning passes, $d^*(t)$.

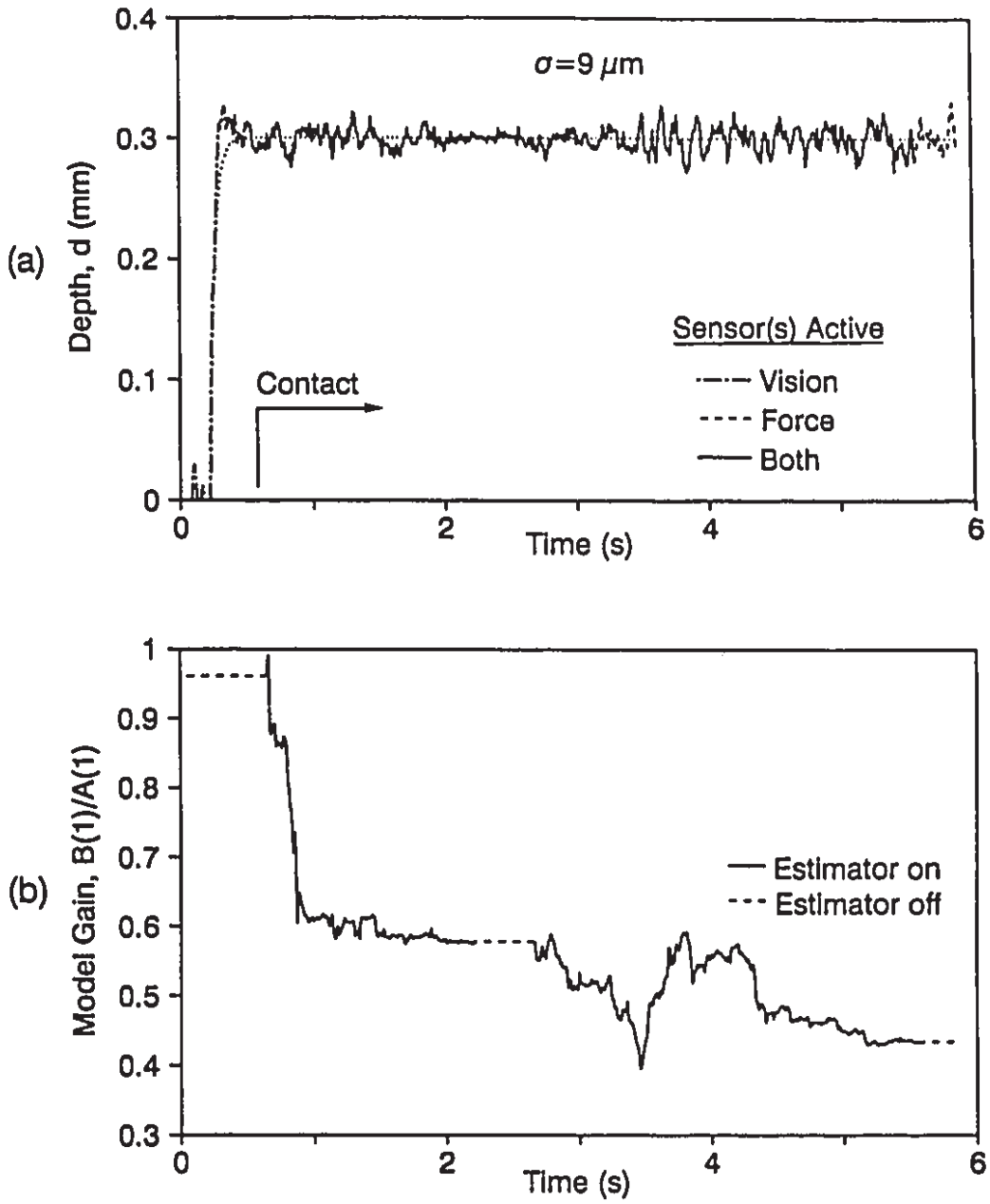

Figure 7.8 Test results for a 304 stainless steel straight edged part deburred under adaptive GPCL. (a) Depth, *d*. (b) Model gain, *B(1)/A(1)*.

machinability of the stainless steel. This lower machinability means that the cutting process has increased stiffness, which should in turn reduce the model gain (since the AEE will have to move the tool farther to change the depth of cut). As shown in Figure 7.8(b) this was indeed the case, the average model gain of 0.52 is 16% less than with the 1018 steel result (Figure 7.7(b)).

It is logical to expect that the robot's positioning errors will increase with the complexity of its motion. Because the planar parts require more complex motions than the straight edged parts these errors should be greater, in turn making the depth more difficult to control. Any changes in the motion of the robot which require rapid acceleration or deceleration may excite the robot's structural dynamics and create such errors. This is the case when the robot enters and exits the curved segments in the planar parts. During the corner the robot undergoes a centripetal acceleration. On entry this acceleration is suddenly applied, and at exit it is just as suddenly removed.

The depth response for a design 1 part deburred under non-adaptive GPC is shown in Figure 7.9. As expected, the depth variation was much larger during the corner segment C-D. The response under adaptive GPCL is shown in Figure 7.10. Note that the improvement in performance over non-adaptive GPC of just 16% is much less than for the straight edged case. One reason for this is that the vision sensor is inactive during the corner so no learning takes place there. Two other reasons, which will be discussed in greater detail with the results for the design 3 part, are that the changes in process dynamics, and the size of the positioning errors are both greater than for the straight edged case.

The corner radius for the design 2 part is twice as large as for design 1. The

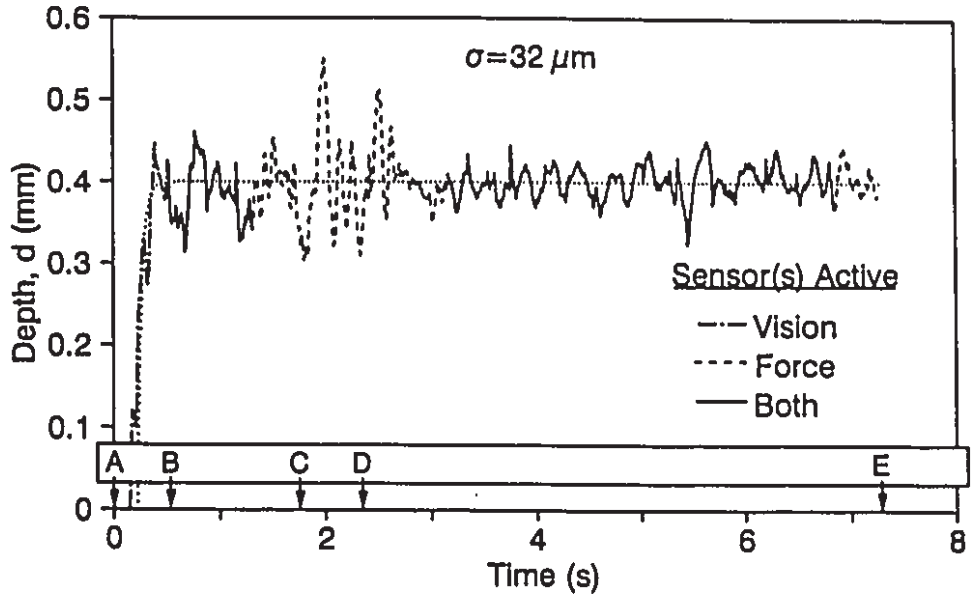

Figure 7.9 Depth response for a design 1 part deburred under non-adaptive GPC.

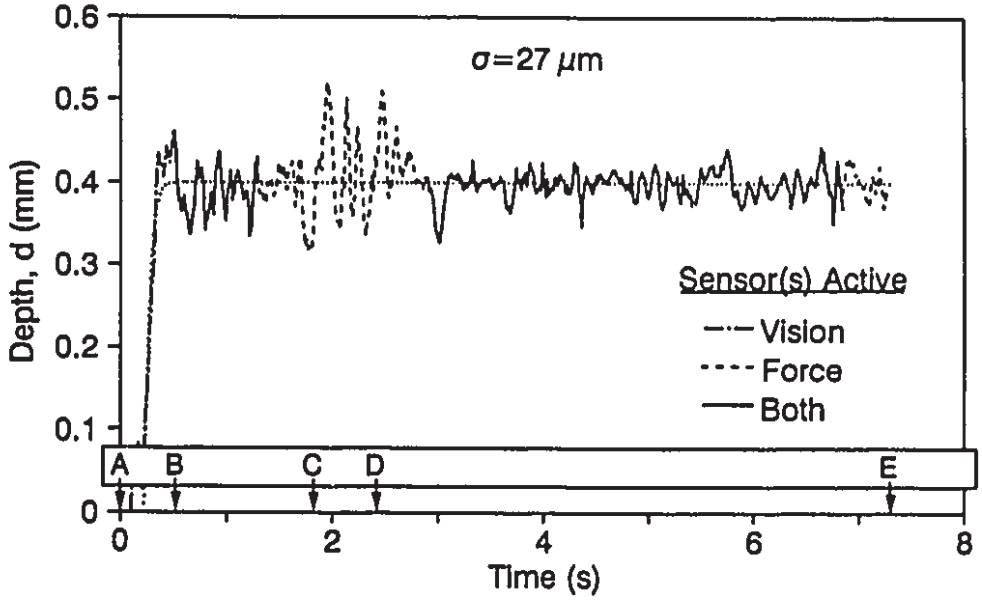

Figure 7.10 Depth response for a design 1 part deburred under adaptive GPCL.

centripetal acceleration and its subsequent effect should therefore decrease, since for a point mass this acceleration is equal to the speed squared divided by the radius of motion. In fact, the depth variations for the design 2 part (Figure 7.11) during the corner (segment C-D) were only slightly less than for the design 1 part. If the feedrate is doubled to 50 mm/s these variations should substantially increase. As illustrated by the result in Figure 7.12, this was not the case, and in fact the variations during cornering were reduced. Clearly the positioning errors, and resultant depth variations, cannot be attributed solely to the effect of the centripetal acceleration. Since the overall depth response at 50 mm/s was only slightly worse than at 25 mm/s (based on their σ values), a 50 mm/s feedrate could be used to achieve a higher production rate. Note that this feedrate could not be used with the design 1 part because it required the robot's acceleration limit to be exceeded.

The depth response for a 304 stainless steel design 2 part is given in Figure 7.13. The regulation, with $\sigma = 22$ μm, was slightly better than for the 1018 steel part. Earlier, for a straight edged part, the regulation was slightly worse with stainless steel. It seems that these small differences (3 and 5 μm) were due to experimental variability, and the deburring performance was basically unaffected by the part material.

The design 3 part has the most complex edge geometry of the parts tested, and as such was the most difficult to deburr. Test results for a design 3 part deburred under adaptive GPCL are shown in Figure 7.14. For this result σ was 17 μm. This substantial increase in comparison to the straight edged parts was due to greater changes in process dynamics, and larger positioning errors. The changes in dynamics were mainly caused by the changes in robot arm's stiffness with configuration as the

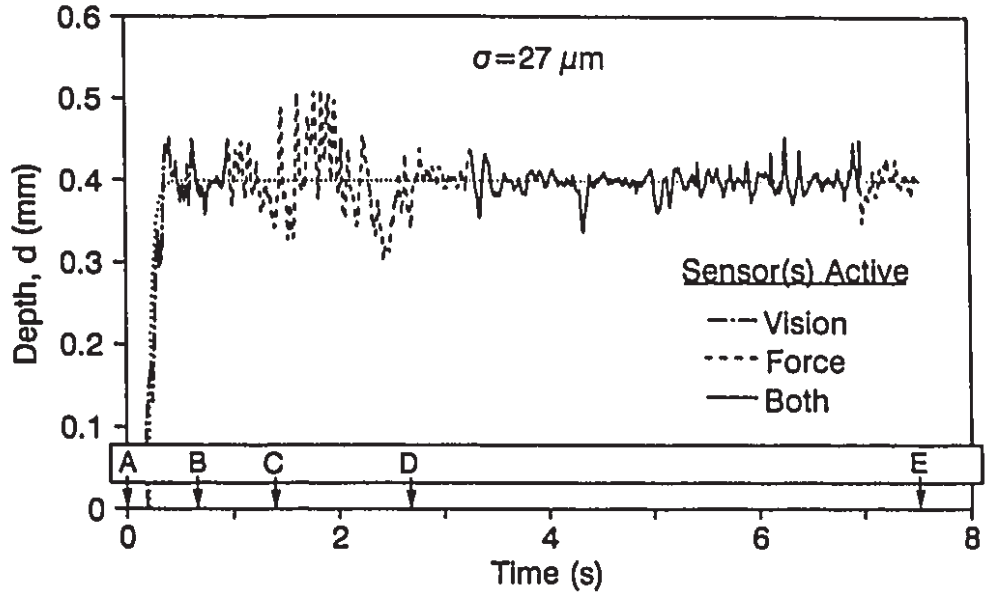

Figure 7.11 Depth response for a design 2 part deburred under adaptive GPCL.

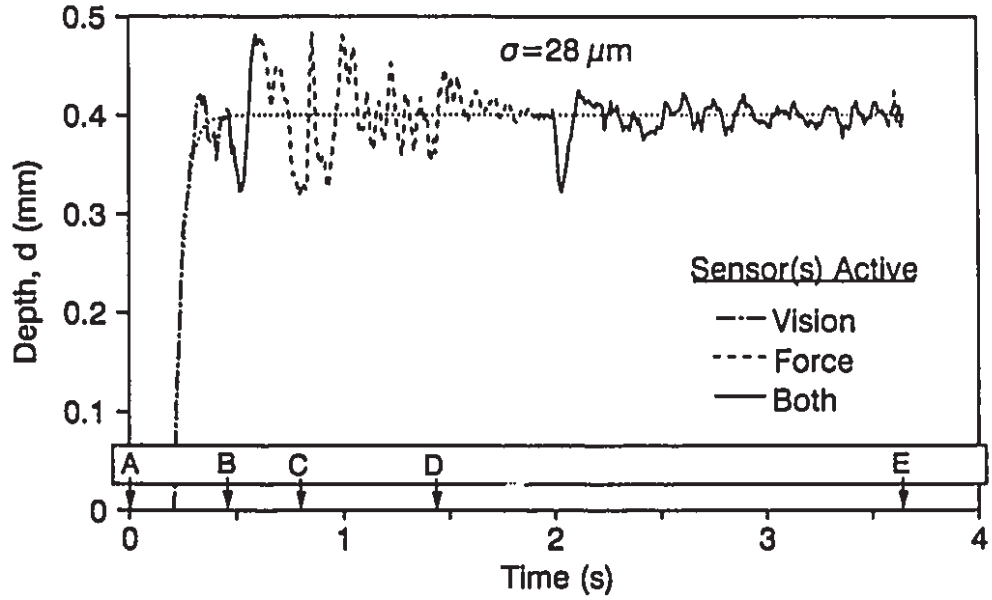

Figure 7.12 Depth response for a design 2 part deburred under adaptive GPCL with a feedrate of 50 mm/s.

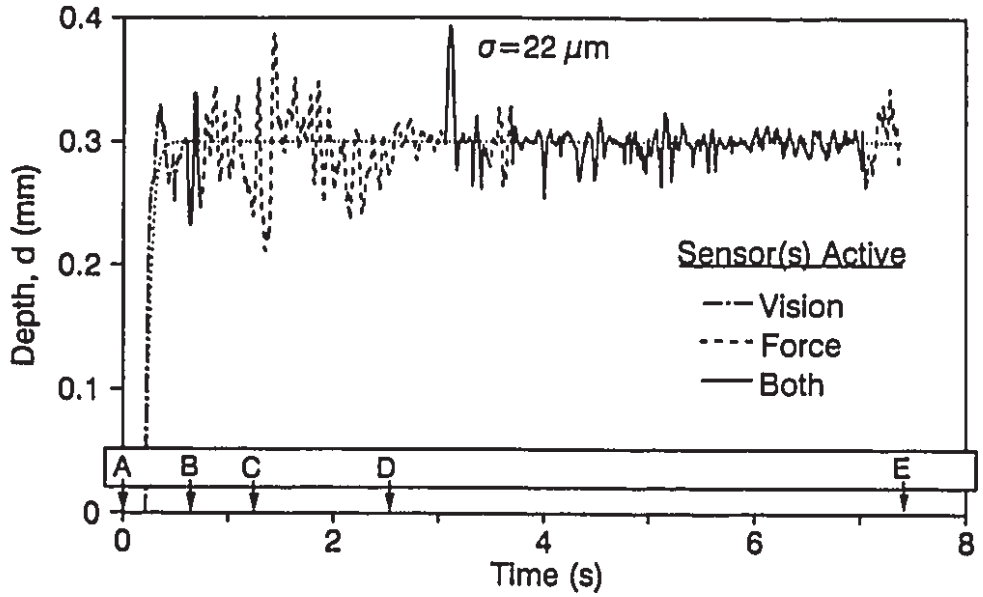

Figure 7.13 Depth response for a 304 stainless steel design 2 part deburred under adaptive GPCL.

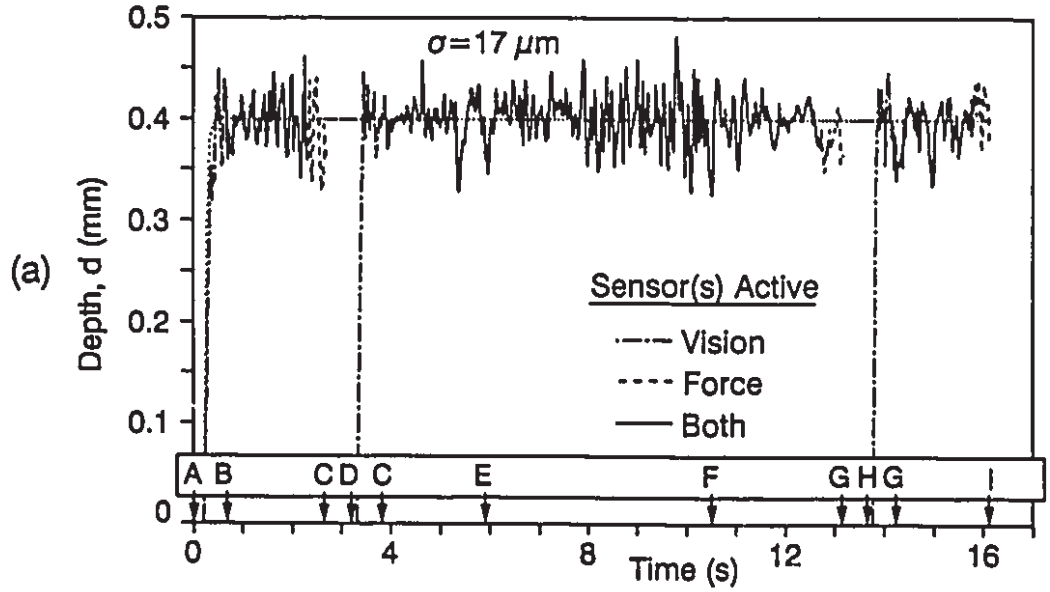

Figure 7.14a Test results for a design 3 part deburred under adaptive GPCL. (a) Depth, *d*.

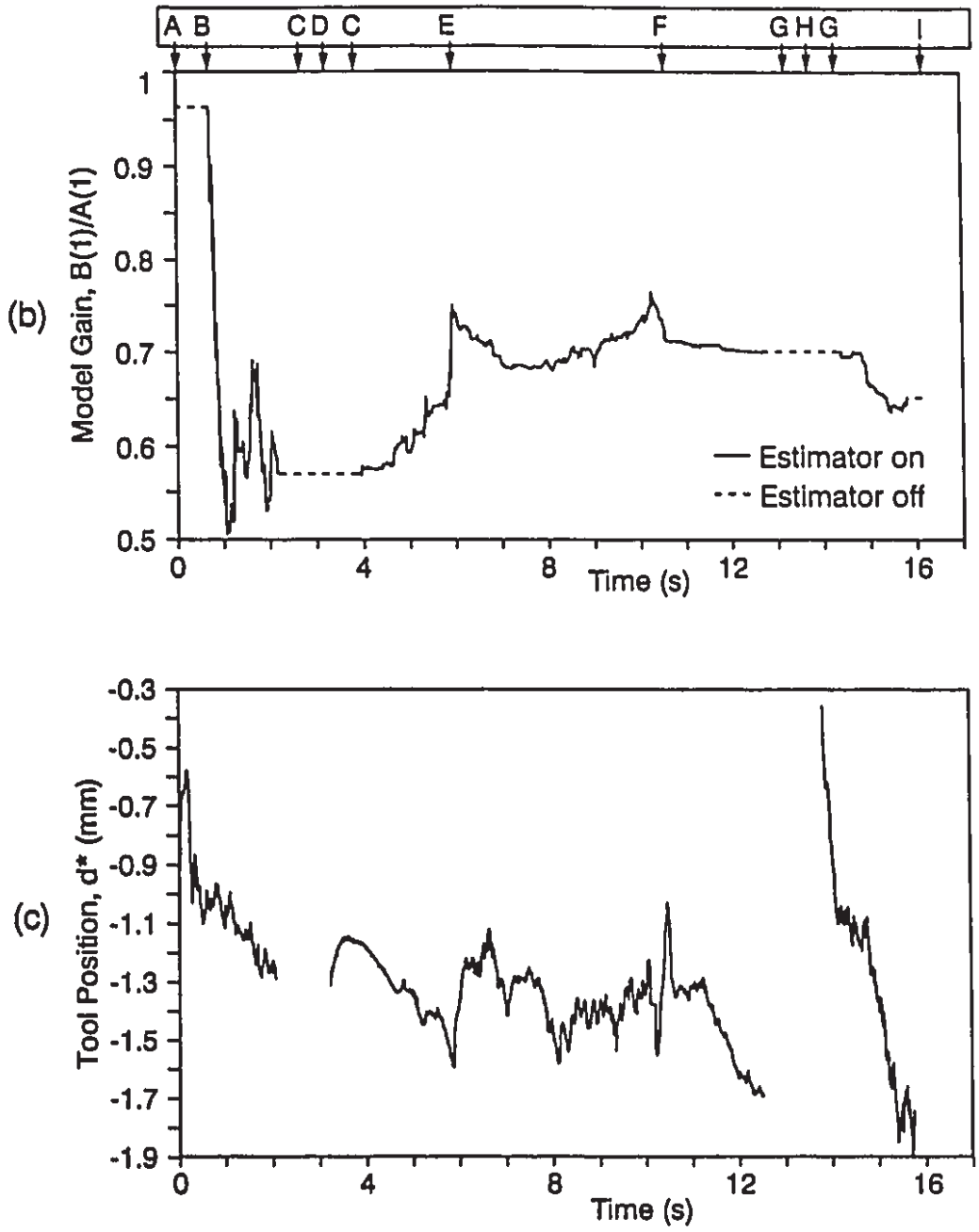

Figure 7.14b Test results for a design 3 part deburred under adaptive GPCL. (b) Model gain, $B(1)/A(1)$. (c) Average tool position from learning passes, d^*.

edge was followed. These changes are reflected by the model gain, where a lower gain corresponds to a lower stiffness. As shown in Figure 7.14(b), during segment B-C the gain was at its lowest level. This was followed by a general increase during segments C-E, and E-F; and a reduction during segments F-H, and G-I. This pattern is distinct from the straight edged result (Figure 7.7(b)), where the change in arm configuration was small, and (after the initial transient) the gain was fairly constant. As mentioned earlier, d^* provides a measurement of the robot and part positioning errors. Note that because d^* is measured by the vision sensor there are gaps in the graph when the vision sensor in inactive. For this result (Figure 7.14(c)) the standard deviation of d^* is 0.17 mm, which is over 4 times larger than for the straight edged test.

The effects of a smaller depth setpoint and a higher feedrate were also investigated. With a desired depth of 0.3 mm the response (Figure 7.15) was virtually identical to the previous response, and also has a σ value of 17 μm. When the feedrate was increased to 50 mm/s the depth variation increased slightly, with $\sigma = 20$ μm. This increase corresponds to the increase in the variation of d^* (Figure 7.16(c)), which has a standard deviation of 0.24 mm. The d^* graph is very similar in shape to the 25 mm/s result with its time axis halved due to the feedrate increase. This suggests that the positioning errors are mainly a result of the robot's kinematic errors, and not structural vibrations. This supports the earlier conclusion regarding the effect of the centripetal acceleration when cornering. Increasing the feedrate also increases the stiffness of the cutting process. This should decrease the model gain, as it did when cutting stainless steel. As shown in Figure 7.16(b), this was the case.

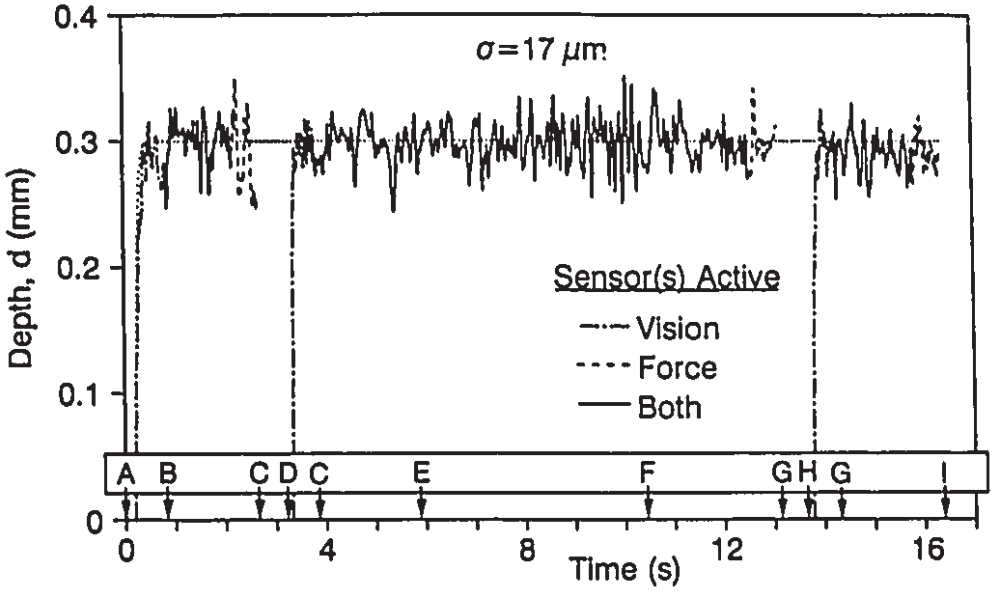

Figure 7.15 Depth response for a design 3 part deburred under adaptive GPCL with a depth setpoint of 0.3 mm.

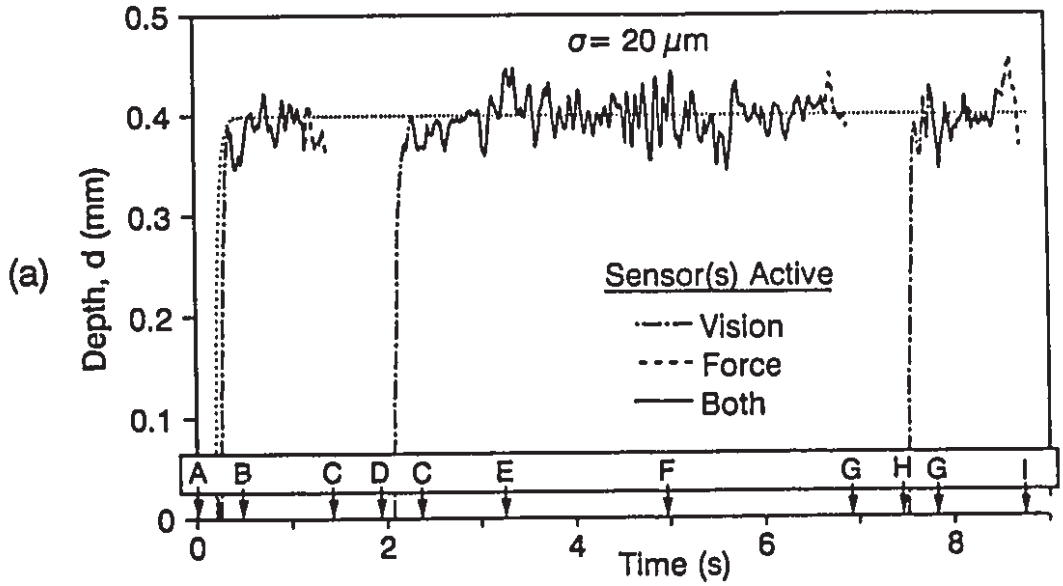

Figure 7.16a Test results for a design 3 part deburred under adaptive GPCL at a feedrate of 50 mm/s. (a) Depth, *d*.

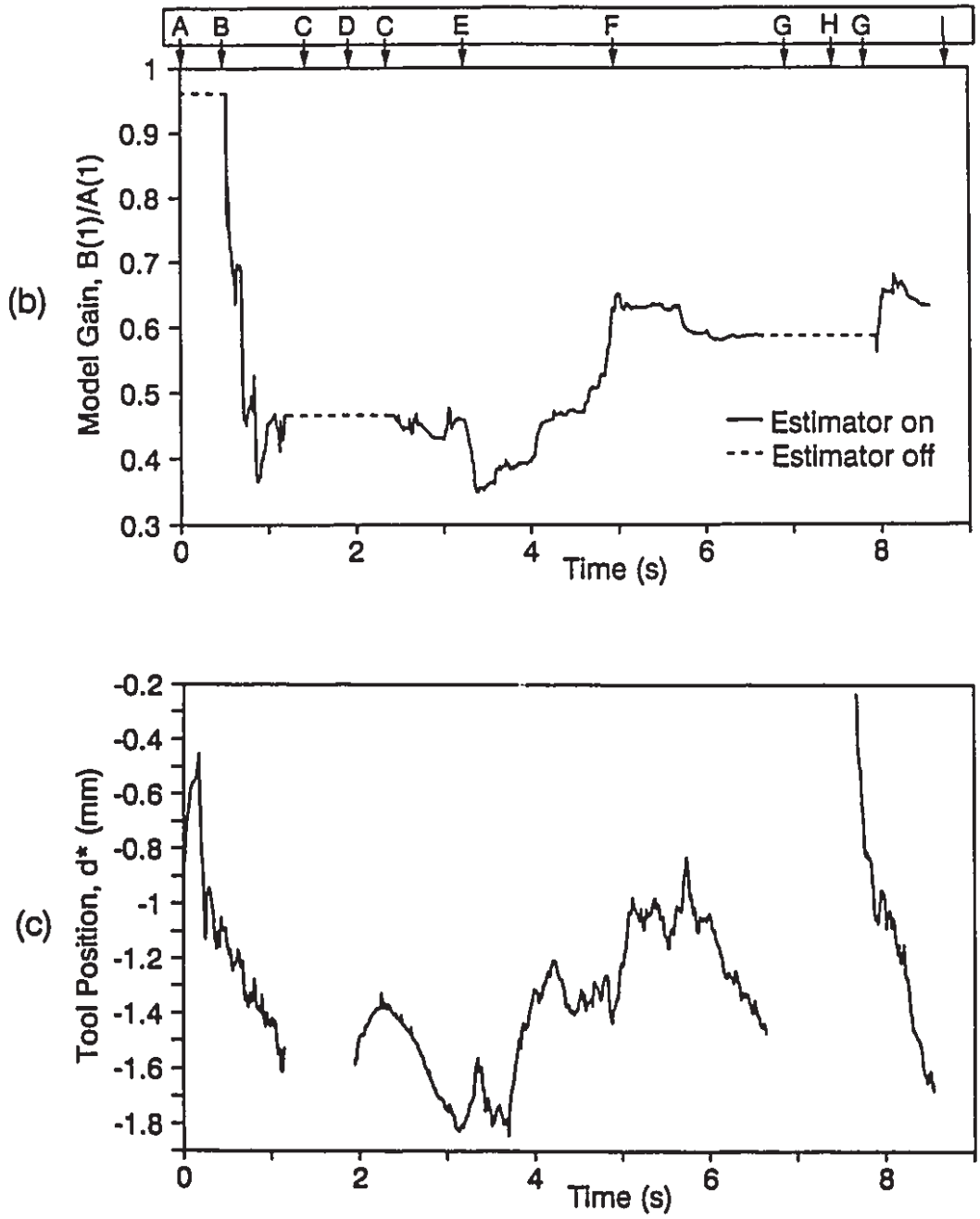

Figure 7.16b Test results for a design 3 part deburred under adaptive GPCL at a feedrate of 50 mm/s. (b) Model gain, *B(1)/A(1)*. (c) Average tool position from learning passes, d^*.

While the gain follows about the same pattern as it did in Figure 7.14(b), the average gain was decreased from 0.68 to 0.53.

7.4 INSPECTION TEST RESULTS AND DISCUSSION

The inspection tests were performed at a speed of 25 mm/s. Given that the system's sampling rate is 52.5 Hz, the chamfer depth measurements were taken at 0.5 mm intervals along the edge. To obtain a reference measurement the edges were also inspected manually using a Nikon Measurescope microscope, which is accurate to 1 μm. The automated inspection system's accuracy can then be confirmed by a statistical comparison between the two sets of measurements. The overall accuracy of the deburring system can be obtained by comparing the microscope measurements with the depth setpoint. The measurement rate for the microscope approach was found to be approximately 1/30 Hz. According to Selleck and Loucks [25], in industry the edges are typically inspected by measuring sections of a silicone casting of the edge using an optical comparator. Clearly this method, like the microscope approach, is very time consuming when compared to the automated inspection system.

The measurement comparison was performed on representatives of the simplest (straight edged) and most complex (design 3) parts deburred. For the straight edged part whose control results were shown in Figure 7.7, a comparison of the frequency distributions of the microscope and inspection system measurements is shown in Figure 7.17. The microscope measurements have a mean, $\bar{d}=0.383$ mm, and a standard deviation, $\sigma=5$ μm. For the inspection system $\bar{d}=0.38$ mm, and $\sigma=8$ μm. For the design 3 part whose control results were shown in Figure 7.14 the

measurement comparison is shown in Figure 7.18. For the microscope measurements $\bar{d}=0.387$ mm, and $\sigma=15$ μm; and for the inspection system $\bar{d}=0.39$ mm, and $\sigma=19$ μm. For both parts the $\bar{d}$ values from the two systems agree within the accuracy of ± 24 μm, specified in Chapter 5 for the inspection system. In both cases the inspection system over-estimated the σ value due to the additive effect of measurement noise.

Note that for both parts the σ values from the microscope measurements are slightly less than the values measured during the deburring tests (6 and 17 μm). This is because the σ values obtained during the deburring tests are based on the tool position and do not take into account the smoothing effect the tool geometry has when generating the chamfer.

To obtain the accuracy of the deburring system the microscope measurements will be compared to the desired chamfer depth. For both of these parts $d_{ref}=0.4$ mm. The accuracy of a measurement is equal to the sum of the signed values of the difference between the mean of the measurements and the actual value, and the dispersion, which gives the largest absolute sum [69]. Here the mean of the microscope measurements will be taken as the actual value. With a dispersion of 3σ the measurements should fall within the accuracy band 99.7% of the time. For the straight edged part the accuracy is then $\pm(17+3\cdot 5)=\pm 32$ μm. For the design 3 part the accuracy is $\pm(13+3\cdot 15)=\pm 58$ μm. Therefore if the system is used on purely straight edged parts the accuracy is ± 0.03 mm. If it is used on parts whose geometry is comparable to design 3 the accuracy is ± 0.06 mm.

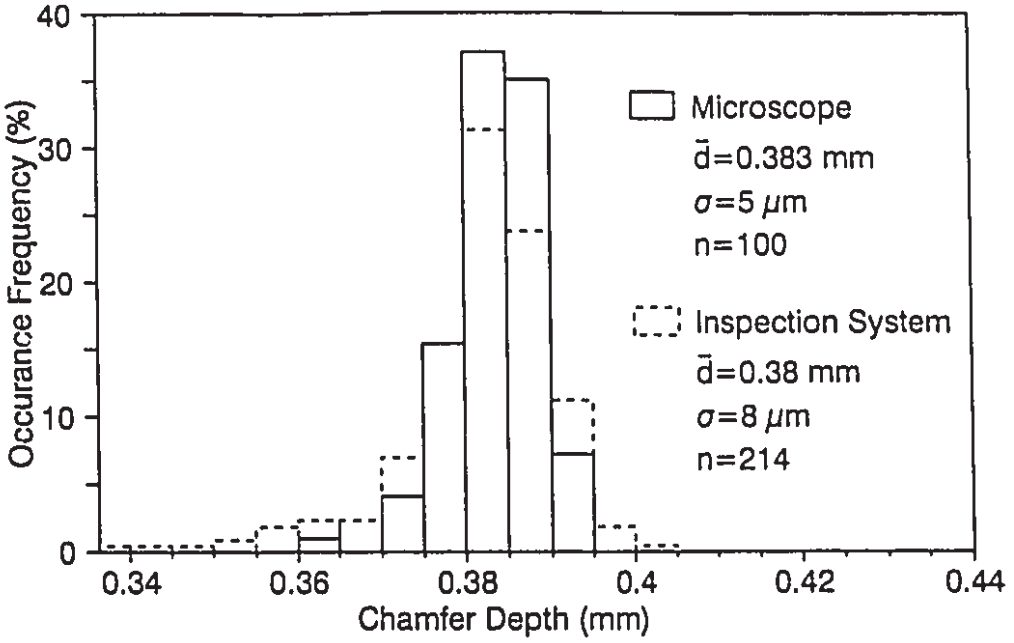

Figure 7.17 Comparison of the frequency distributions of the depth measurements obtained by the inspection system and by microscope for a straight edged part (whose control results were shown in Figure 7.7).

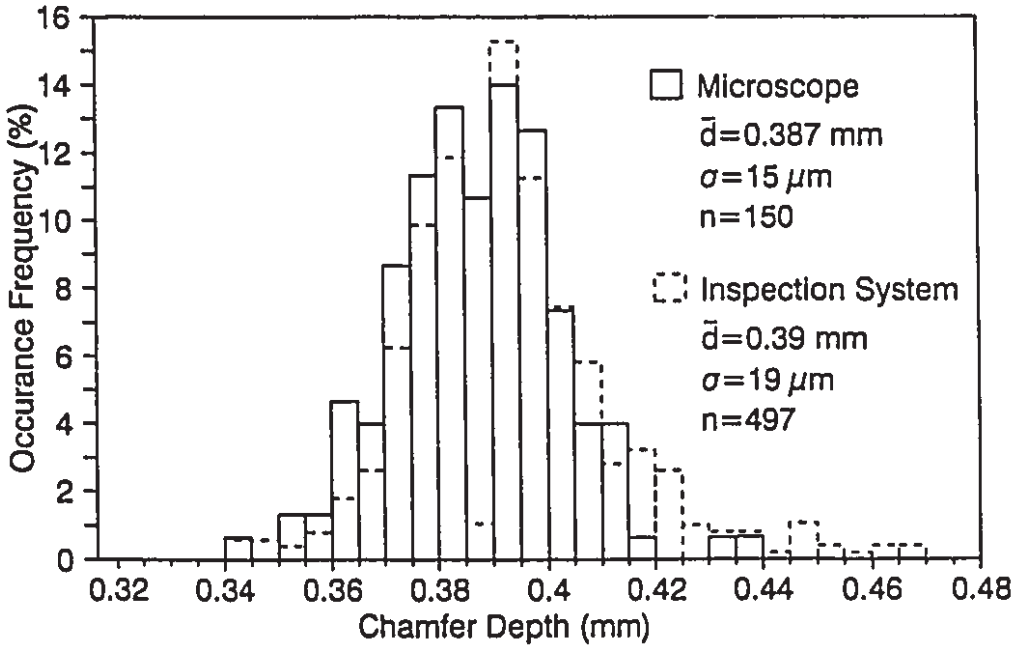

Figure 7.18 Comparison of the frequency distributions of the depth measurements obtained by the inspection system and by microscope for a design 3 part (whose control results were shown in Figure 7.14).

7.5 CONCLUSIONS

7.5.1 Deburring Tests

Depth controlled deburring tests were performed on straight edged and planar parts made of 1018 steel and 304 stainless steel. The planar parts were made up of combinations of linear and circular edge segments. Feedrates of 25 and 50 mm/s, and depth setpoints of 0.3 and 0.4 mm were used. The hardware consisted of the AEE mounted to a PUMA-762 robot, and a 33 MHz, 80486 microcomputer. User interface, system supervisor, and AEE control functions were performed by the microcomputer.

As predicted by the simulations in Chapter 6, in comparison with non-adaptive GPC, the regulation performance was improved with adaptive GPC, and further improved with adaptive GPCL. For straight edged parts the standard deviations of the depth measurements were 15, 9, and 6 μm, respectively.

The depth variations increased with the planar parts. With a design 3 part under adaptive GPCL, for example, the standard deviation was 17 μm. This increase was due to the greater changes in process dynamics and larger positioning errors encountered when deburring the planar parts. The changes in dynamics were mainly caused by the changes in the robot arm's stiffness with configuration as the edge was followed. These were reflected by greater changes of the model gain, where a lower gain corresponded to a lower stiffness. The robot and part positioning errors were indicated by the average tool position from the learning passes. These errors increased in size over 400% relative to the straight edged case. The similarity in shape of the positioning error graphs at 25 and 50 mm/s suggested that the errors

were mainly a result of the robot's kinematic errors, and not structural vibrations.

Based on the results of both the straight edged and planar part tests, the performance was found to be basically unaffected by the part material, and the depth setpoint. The lower machinability of the stainless increased the cutting stiffness, as did increasing the feedrate to 50 mm/s. This increased stiffness was reflected by a decrease in the model gain. The 50 mm/s feedrate could be used to increase the production rate, since the performance was only slightly worse than at 25 mm/s (for a design 3 part, σ increased from 17 to 20 μm). However it can not be used with parts with small radii, such as a design 1 part, because the acceleration required exceeds the robot's capabilities.

7.5.2 Inspection Tests

Manual microscope measurements were used to verify the accuracy of both the automated inspection system, and the deburring system. Representatives of the simplest (straight edged) and most complex (design 3) parts were measured. The inspection system's measurement errors were within its accuracy band. The inspection system obtains measurements at a rate of 52.5 Hz, which is 1500 times faster than the manual approach.

The deburring system's accuracy was found to be dependant on the part geometry. If the system is used on straight edged parts the accuracy is ±0.03 mm. If it is used on parts whose geometry is comparable to design 3 the accuracy is ±0.06 mm.

CHAPTER 8

CONCLUSIONS AND RECOMMENDATIONS

8.1 INTRODUCTION

This thesis described the development of a system for automated robotic edge deburring. The main emphasis was on accurate sensing and control of the chamfer depth during the deburring pass. The system was based on a PUMA-762 industrial robot equipped with a custom built, high performance, AEE. The control was performed through the AEE to overcome the limited accuracy and bandwidth of the robot's position control system. A number of algorithms for controlling the normal deburring force (the most common method used to indirectly control the depth) were compared based on computer simulations and deburring experiments. A new vision sensor was then developed to obtain a more direct measurement of the depth. The information from both sensors is combined using a sensor fusion scheme. Based on the force control results, and the time varying nature of robotic deburring, adaptive GPC, was chosen as the control algorithm. This algorithm was then modified to include learning control. The performance of this new algorithm, termed GPC with Learning or GPCL, was examined both theoretically, and experimentally. Depth controlled deburring experiments were then performed on a variety of straight edged and planar parts. An automated inspection system was also developed to verify the deburring performance.

8.2 CONCLUSIONS

1) The design for the new AEE was obtained by modifying a previous design, based on the conclusions drawn from a dynamic analysis of the robotic deburring system. The dynamic model included the robot arm, AEE, and deburring process dynamics. The analysis concluded that minimizing the AEE's tool mass had the most beneficial effect, followed by minimizing the AEE's base mass, maximizing the actuator bandwidth, and maximizing the AEE's stiffness. The new design incorporates a lighter tool, a single (rather than double) motion axis to reduce the base mass, and a stiffer ball slide. The actuator bandwidth was increased from 20 to 65 Hz by modifying the servo amplifier. Based on dial gauge measurements the AEE's positioning accuracy and repeatability are within 0.01 mm. Based on transfer function measurements, the stiffness to mass ratio for the new design was 8.6 times greater than the old design.

2) Several non-adaptive force control algorithms based on a CARIMA time series process model were investigated. The objective was to control the chamfer depth by minimizing the variance of the normal force. The algorithms were evaluated through computer simulation prior to experimental verification using a PUMA-560 robot with the old AEE. 1018 steel, straight edged parts and a feedrate of 25 mm/s were used. Based on the experimental force variances, and chamfer surface finish produced, the controllers ranked (from best to worst): EH, EPID, GMV, and LQG. The poor performance of the LQG design was attributed to the excitation of process nonlinearities as a result of its large position command variance. The EH design

achieved an experimental force variance of 0.11 N^2 at a 5 N setpoint. This produced a chamfer with a depth of 0.68 mm, and a roughness of 9.5 μm (ISO Ra). In the open-loop the depth varied from 0.23-0.57 mm along the length of the cut.

3) Simulations were performed to access the potential benefits of parameter adaptive force control for deburring with time varying process dynamics. The time varying dynamics were simulated by switching the process model instantaneously switched between three different CARIMA models. An adaptive version of the Smith predictor achieved a smooth stable response with a risetime of 0.07 s. To achieve a comparably smooth response the non-adaptive Smith predictor had to be detuned, which increased the risetime to 0.36 s. A MRAC algorithm was also investigated which achieved a risetime of 0.16 s.

4) A vision sensor was developed to obtain a more direct measurement of the chamfer depth. The measurement is obtained using active triangulation with a video camera and a laser line structured light source. The image analysis is performed mainly on an Intel EV80C196KC SBC programmed in assembly language. The sensor measures the position of the tool relative to the edge at a rate of 105 Hz, with an accuracy of ± 13 μm over a 1 mm range. The maximum range is -6 to 3 mm.

5) A sensor fusion scheme was developed to combine the information from the force and vision sensors. The resulting depth measurement is more accurate and reliable than possible using each sensor alone.

6) Based on the success of the predictive algorithms with force control, and its flexibility, adaptive GPC was chosen to control the depth. Three CARIMA process models are used alternately. One non-contact model used during the initial approach, and two contact models used during deburring (depending on whether the force or vision measurement is used). To adapt to changes in dynamics, the contact model parameters were estimated on-line using RLS. In a computer simulation, with the model gain initially set to 70% of the process gain, the estimator reduced the gain error to 3% after 0.5 s. The standard deviation of the depth was 15 μm.

7) The new GPCL algorithm is applicable to any process which can be modelled by a CARIMA model, and is performed repeatedly. GPCL improves the regulation performance of GPC by learning and compensating for the repeatable portion of the disturbance. Because GPCL only adds a feedforward term to GPC, the stability properties of GPC are unaffected. In a theoretical analysis GPCL is shown to converge asymptotically (subject to certain constraints). In a non-contact edge following application, after just 3 trials the output variance was reduced 32% relative to GPC, after 10 trials the reduction was 43%.

8) Depth controlled deburring experiments were performed on straight edged and planar parts made of 1018 steel, and 304 stainless steel. Feedrates of 25 and 50 mm/s, and depth setpoints of 0.3 and 0.4 mm were used. The hardware consisted of the AEE mounted to a PUMA-762 robot, and controlled by a 33 MHz Intel 80486-based microcomputer.

In comparison to non-adaptive GPC, the regulation was improved with

adaptive GPC, and further improved with adaptive GPCL. For straight edged parts the standard deviations of the depth measurements were 15, 9, and 6 μm, respectively. The depth variations inc sed with the planar parts. With a design 3 part under adaptive GPCL, for example, the standard deviation was 17 μm. This was due to the greater changes in process dynamics and larger positioning errors encountered when deburring the planar parts. These were reflected by greater changes in the model gain, and larger deviations measured during the learning passes. The deburring performance was found to be unaffected by the part material and depth setpoint. The 50 mm/s feedrate resulted in only slightly worse performance than at 25 mm/s, and could be used to increase the production rate.

9) Manual microscope measurements were used to verify the accuracy of both the automated inspection system, and the deburring system. The inspection system measurement errors were within its accuracy band of ±24 μm. The system obtains measurements at a rate of 52.5 Hz (using the same hardware as the vision sensor with modified software), which is 1500 times faster than the manual approach.

The deburring system's accuracy was found to be dependant on the part geometry. If the system is used on straight edged parts the accuracy is ±0.03 mm. If it is used on parts whose geometry is comparable to the design 3 part the accuracy is ±0.06 mm.

8.3 RECOMMENDATIONS FOR FUTURE WORK

1) The system should be expanded to deburr a wider variety of part designs and materials using a variety of tools. An automated task planning system is currently being developed by Ph.D. candidate P. W. Tam to help provide this capability. When this system is completed it should be incorporated into the automated deburring system.

2) Potential future applications of the theoretical ideas and technology developed in this research are listed in Table 8.1.

Theoretical/ Technological Development	Potential Applications:				
	Robotics				Machine Tools
	Die Polishing	Grinding	Seam Welding	Precision Assembly	Geometric Adaptive Control
High Performance AEE	✓	✓	✓	✓	
High Speed Vision Sensor	✓	✓	✓	✓	✓
Sensor Fusion of Force and Vision	✓	✓		✓	
GPCL Control Algorithm	✓	✓	✓	✓	✓
Automated Inspection System		✓	✓		

Table 8.1 Potential applications for the theoretical and technological developments.

REFERENCES

1. Gillespie, L. K., and King, R. E. (Ed.), *Robotic Deburring Handbook*, SME, 1987.
2. Kramer, B. M., Bausch, J. J., Gott, R. L., and Dombrowski, D. M., "Robotic Deburring", *Robotics & Computer-Integrated Manufacturing*, Vol. 1, No. 3/4, 1984, pp. 365-374.
3. Gillespie, L. K., "Surface and Edge Improvement", *Tool and Manufacturing Engineers Handbook*, Vol.3, Chapt. 15, SME, 1985.
4. Gillespie, L. K., "The Formation and Properties of Machining Burrs", *ASME Journal of Engineering for Industry*, Feb. 1976, pp. 66-74.
5. Gillespie, L. K., *Advances in Deburring*, SME, 1978.
6. Gillespie, L. K., "The Academic Challenge of Burr Technology", *Deburring and Surface Conditioning '85*, SME, 1985.
7. Iwata, K., Ueda, K., and Okuda, K., "Study of Mechanism of Burrs Formation in Cutting Based on Direct SEM Observation", Journal of the Japan Society for Precision Engineering, Vol. 48, No. 4, 1982, pp. 94-99.
8. Ko, S.-L. and Dornfeld, "Analysis and Modelling of Burr Formation and Breakout in Metal", *Mechanics of Deburring and Surface Finishing Processes*, PED-Vol.38, ASME, 1989, pp. 79-91.
9. Bausch, J. J., *Compliant Tools for Robotic Deburring*, MSc Thesis, MIT, Aug. 1985.

10. Kazerooni, H., Bausch, J. J., and Kramer, B. M., "An Approach to Automated Deburring by Robot Manipulators", *ASME Journal of Dynamic Systems, Measurement, and Control*, Vol. 108, 1986, pp. 354-359.

11. Bone, G. M., *Robotic Force Control for Deburring Using an Active End Effector*, M. Eng. Thesis, McMaster U., Hamilton, Ont. Canada, 1988.

12. M. A. Elbestawi, and R. Sagherian, "Parameter Adaptive Control in Peripheral Milling", *Internation Journal of Machine Tools and Manufacturing*, Vol. 27, No. 3, 1987, pp. 399-414.

13. Roberts, R., and Engel, T., "Process Models for Deburring and Chamfering Aerospace Alloys", *4th World Conference on Robotics Research*, Pittsburg, PA, 1991.

14. Loucks, C. S., Selleck, C. B., and Thunborg, S., "Cad-Directed Robotic Edge Finishing", *SME Technical Paper*, No. MR89-114, 1989.

15. Duelen, G., Münch, H., and Surdilovic, D., "Advanced Robot Control Systems", *International Conference on Manufacturing Systems and Environments*, Tokyo, 1990, pp. 123-128.

16. Guvenc, L., and Paul, F. W., "Active End-Effector Force and Impedance Control in Robot Assisted Material Removal", *Symposium on Robotics*, ASME, 1988, pp. 283-298.

17. Dornfeld, D. A., and Masaki, T., "Acoustic Emission Feedback for Deburring Automation", *Modeling and Control of Robotic Manipulators and Manufacturing Processes*, DSC-Vol.6, ASME, 1987, pp. 81-89.

18. Dornfeld, D. A., and Erickson, E., "Robotic Deburring with Real Time

Acoustic Feedback Control", *Mechanics of Deburring and Surface Finishing Processes*, PED-Vol.38, ASME, 1989, pp. 13-26.

19. Dornfeld, D. A., "Intelligent Deburring of Precision Components", *IEEE/SICE International Conference on Industrial Electronics, Control, Instrumention, and Automation*, San Diego, CA, Nov. 1992, pp. 953-960.

20. Hollowell, R., and Guile, R., "An Analysis of Robotic Chamfering and Deburring", *Modeling and Control of Robotic Manipulators and Manufacturing Processes*, DSC-Vol.6, ASME, 1987, pp. 73-79.

21. Starr, G. P., and Loucks, C. S., "Edge Finishing Using Hybrid Position/Force Control of an XY Table", *IEEE/SICE International Conference on Industrial Electronics, Control, Instrumention, and Automation*, San Diego, CA, Nov. 1992, pp. 934-939.

22. Whitney, D. E., Edsall, A. C., Todtenkopf, A. B., Kurfess, T. R., and Tate, A. R., "Development and Control of an Automated Robotic Weld Bead Grinding System," *ASME Journal of Dynamic Systems, Measurement, and Control*, Vol. 112, 1990, pp. 166-176.

23. Todtenkopf, A. B., *Vision and Force Controlled Weld Bead Grinding System*, MSc Thesis, MIT, Jan. 1988.

24. Seliger, G., and Hsieh, L. -H., "Sensor-Aided Programming and Movement Adaptation for Robot-Guided Deburring of Castings," *Annals of the CIRP*, Vol. 40/1, 1991, pp. 487-490.

25. Selleck, C. B., and Loucks, C. S., "A System for Automated Edge Finishing", *IEEE Conference on Systems Engineering*, Pittsburgh, PA, Aug. 1990, pp. 423-

429.

26. Kazerooni, H., "Hybrid Force/Position Control in Robotic Deburring", *Modeling and Control of Robotic Manipulators and Manufacturing Processes*, DSC-Vol. 6, ASME, 1987, pp. 55-63

27. Paul, F. W., Getty, T. K., and Thomas, J. D., "Definning of Iron Castings Using a Robot Positioned Chipper", *Robotics Research and Advanced Applications*, ASME, 1982, pp. 269-278.

28. Zalucky, A., and Hardt, D. E., "Active Control of Robot Structure Deflections", *Robotics Research and Advanced Applications*, ASME, 1982, pp. 83-100.

29. Hollis, R. L., "A Fine Positioning Device for Enhancing Robot Precision", *Proceedings of the Robots 9 Conference*, Detroit, Jun. 1985, pp. 6.28-6.36.

30. Tlusty, J., and Wegerif, D., "Compensating for Deflections of a Robot in Light Machining Operations", *Robotics: Theory and Applications*, DSC-Vol. 3, ASME, 1986, pp. 91-100.

31. Hollowell, R., "Hybrid Force/Position Control for Robotic Light Machining", *Proceedings of the ANS Third Topical Meeting on Robotics and Remote Systems*, Charleston, S. C., Mar. 1989, pp. 1-6.

32. Roberts, R. K., Engel, T. W., and Proctor, F., "Specification of an Active Force Control Tool for Performing Deburring and Chamfering on a Robot Platform", *IEEE/SICE International Conference on Industrial Electronics, Control, Instrumention, and Automation*, San Diego, CA, Nov. 1992, pp. 918-926.

33. Kazerooni, H., "Direct-Drive Active Compliant End Effector (Active RCC)", *IEEE Journal of Robotics and Automation*, Vol. 4, No. 3, June 1988, pp. 324-333.

34. Raibert, M. H., and Craig, J. J., "Hybrid Position/Force Control of Manipulators", *ASME Journal of Dynamic Systems, Measurement, and Control*, Vol. 102, 1981, pp. 126-133.

35. Stepien, T. M., Sweet, L. M., Good, M. C., and Tomizuka, M. , "Control of Tool/Workpiece Contact Force with Application to Robotic Deburring," *IEEE Journal of Robotics and Automation*, Vol. RA-3, No. 1, 1987, pp. 7-18.

36. Haefner, K. B., Houpt, P. K., Baker, T. E., and Dausch, M. E., "Real Time Robotic Position/Force Control for Deburring," *Robotics: Theory and Applications*, DSC-Vol.3, ASME, 1986, pp. 73-78.

37. Kramer, B. M., and Shim, S. S., "Development of a System for Robotic Deburring", *Robotics & Computer-Integrated Manufacturing*, Vol. 7, No. 3/4, 1990, pp. 291-295.

38. Hogan, N., "Impedance Control: An Approach to Manipulation, Part 1: Theory, Part 2: Implementation, Part 3: Applications", *ASME Journal of Dynamic Systems, Measurement, and Control*, Vol. 107, 1985, pp. 1-24.

39. Kazerooni, H., "Automated Robotic Deburring Using Impedance Control", *IEEE Control Systems Magazine*, Feb. 1987, pp. 21-25.

40. Her, M. G., and Zazerooni, H., "Automated Robotic Deburring of Parts Using Compliance Control", *ASME Journal of Dynamic Systems, Measurement, and Control*, Vol. 113, 1991, pp. 60-66.

41. Bone, G. M., Elbestawi, M. A., Liu, L., Sinha, N. K., "Adaptive Robotic Deburring," *IFAC Conference on Adaptive Systems in Control and Signal Processing*, Glasgow, UK, April 1989, pp. 311-316.

42. Duelen, G., Münch, H., Surdilovic, D., and Timm, J., "Automated Force Control Schemes for Robotic Deburring: Development and Experimental Evaluation", *IEEE/SICE International Conference on Industrial Electronics, Control, Instrumention, and Automation*, San Diego, CA, Nov. 1992, pp. 912-917.

43. S. Liu, and H. Asada, "A Skill-Based Adaptive Controller for Deburring Robots", *Control of Manufacturing Processes*, DSC-Vol. 28, ASME, 1991, pp. 107-113.

44. Arimoto, S., Kawamura, S., and Miyazaki, F., "Bettering Operation of Robots by Learning", *Journal of Robotic Systems*, Vol. 1, No. 2, 1984.

45. Craig, J. J., "Adaptive Control of Manipulators Through Repeated Trials", *American Control Conference*, San Diego, CA, 1984, pp. 1566-1573.

46. Kobayashi, F., and Kimura, Y., "A Deburring Robot with Variable Path Speed Using the Repetitive Control", *JAPAN/USA Symposium on Flexible Automation*, Vol. 2, 1992, pp. 865-870.

47. Bone , G. M., and Elbestawi, M. A., "Active End Effector Control of a Low Precision Robot in Deburring", *Robotics and Computer-Integrated Manufacturing*, Vol. 8. No. 1., 1991, pp. 87-96.

48. Plank, G., and Hirtzinger, G., "Controlling a Robot's Motion Speed by a Force-Torque Sensor for Deburring Problems", *4th IPAC/IFIP Symposium on*

Information and Control Problems in Manufacturing Technology, Oct. 1982, pp. 97-102.

49. Bone, G. M., Elbestawi, M. A., Lingarkar, R., and Liu, L., "Force Control for Robotic Deburring", *ASME Journal of Dynamic Systems, Measurement and Control*, Vol. 113, 1991, pp. 395-400.

50. Åström, K. J., and Wittenmark, B., *Adaptive Control*, Addison-Wesley, New York, 1989.

51. Ydstie, B. E., Kershenbaum, L. S., and Sargent, R. W. H. , "Theory and Application of an Extended Horizon Self-Tuning Controller," *AIChE Journal*, Vol. 31, No. 11, 1985, pp. 1771-1780.

52. Kuo, B. C., *Automatic Control Systems*, 5th edition, Prentice-Hall, 1984.

53. Isermann, R., *Digital Control Systems*, Springer-Verlag, 1977.

54. Marshall, J. E., *Control of Time Delay Systems*, Peter Peregrinus Ltd. for IEEE, London, 1979.

55. Isermann, R., "Parameter Adaptive Control Algorithms -A Tutorial", *Automatica*, Vol. 18, No. 5, 1982, pp. 513-528

56. Landau, I. D., "Model Reference Adaptive Controllers and Stochastic Self-Tuning regulators -A Unified Approach", *ASME Journal of Dynamic Systems, Measurement, and Control*, Vol. 103, 1981, pp. 404-416.

57. Besl, P. J., "Active, Optical Range Imaging Sensors", *Advances in Machine Vision*, 1989, pp. 1-53.

58. Ballard, D. H., and Brown, C. M., *Computer Vision*, Prentice-Hall, Englewood Cliffs, NJ, 1982.

59. Shirai, Y., "A Context Sensitive Line Finder for Recognition of Polyhedra", *Artificial Intelligence*, Vol. 4, 1973, pp. 95-119.

60. Elbestawi, M. A., Yuen, K. M., Srivastava, A. K., and Dai, H., "Adaptive Force Control for Robotic Disk Grinding", *Annals of the CIRP*, Vol. 40/1/1991, pp. 391-394.

61. Isermann, R., and Lachmann, K.-H., "Parameter-adaptive Control with Configuration Aids and Supervision Functions", *Automatica*, Vol. 21, No. 6, 1985, pp. 625-638.

62. Clarke, D. W., Mohtadi, C., and Tuffs, P. S., "Generalized Predictive Control - Part I. The Basic Algorithm", *Automatica*, Vol. 23, No. 2, 1987, pp. 137-148.

63. Clarke, D. W., Mohtadi, C., and Tuffs, P. S., "Generalized Predictive Control - Part II. Extensions and Interpretations", *Automatica*, Vol. 23, No. 2, 1987, pp. 149-160.

64. Clarke, D. W., and Mohtadi, C., "Properties of Generalized Predictive Control", *Automatica*, Vol. 25, No. 6, 1989, pp. 859-875.

65. McIntosh, A. R., Shah, S. L., and Fisher, D. G., "Analysis and Tuning of Adaptive Generalized Predictive Control", *The Canadian Journal Chemical of Engineering*, Vol. 69, Feb. 1991, pp. 97-110.

66. Åström, K. J., and Wittenmark, B., *Computer-Controlled Systems -Theory and Design*, Prentice-Hall, Englewood Cliffs, N.J., 1984.

67. Elbestawi, M. A., Bone, G. M., and Tam, P. W., "An Automated Planning, Control, and Inspection System for Robotic Deburring", *Annals of the CIRP*, Vol. 41/1/1992, pp. 397-401.

68. Bone, G. M., and Elbestawi, M. A., "Sensing and Control for Automated Robotic Edge Deburring", *IEEE/SICE International Conference on Industrial Electronics, Control, Instrumention, and Automation*, San Diego, CA, Nov. 1992, pp. 927-933.

69. National Machine Tool Builders' Association, *Definition and Evaluation of Accuracy and Repeatability for Numerically-controlled Machines*, Second Ed., 1972.

APPENDIX A

FORCE SENSOR CALIBRATION

The force sensor is a Kistler model 9251A, 3-axis, piezoelectric sensor. The sensor's X axis is aligned with the AEE's motion axis. Since this axis is oriented normal to the chamfer when deburring this force corresponds to the normal component of the deburring force. The Y axis measures the tangential force (tangential to the part edge). The X and Y outputs are amplified by two Kistler model 5004 charge amplifiers. The signals are then low pass filtered at 40 Hz to reduce high frequency noise and prevent aliasing, and then sampled at 105 Hz by the microcomputer. While measuring the tangential force was not necessary for control purposes, it was necessary for decoupling the normal force measurement.

Prior to calibration, the force sensor was preloaded to the recommended value of 25 kN by tightening the preload bolt while monitoring the amplifier output. The sensor was then calibrated by aligning each axis vertically in turn with a precision bubble level, and applying loads with a set of precision masses. The amplifiers were set to match the sensor's sensitivity specification of 8.1 pC/N. The gains were set to 2 N/V, which, given the amplifier's maximum output of ±10 V, provides a range of ±20 N. Since deburring forces are typically around 5 N this range gives a safety factor of 4 before amplifier overload will occur. The results from loading in the normal direction were least squares fit to the linear relations:

$$N_{volts} = c_{NN} N_{load} \tag{A.1}$$

$$T_{volts} = c_{TN} N_{load} \tag{A.2}$$

where N_{volts} is the output of the normal direction amplifier in V, T_{volts} is the output of the tangential direction amplifier in V, N_{load} is the load applied in the normal direction in N, and c_{NN}, c_{TN} are the calibration constants. For the tangential loading case the relations are:

$$N_{volts} = c_{NT} T_{load} \tag{A.3}$$

$$T_{volts} = c_{TT} T_{load} \tag{A.4}$$

where T_{load} is the load applied in the tangential direction in N, and c_{NT}, c_{TT} are calibration constants. The calibration data and calibration lines are shown in Figure A.1. The calibration constants in V/N, and their associated R^2 (coefficient of determination) values are: $c_{NN}=0.399$, $R^2=0.99995$; $c_{TN}=-0.00443$, $R^2=0.81$; $c_{NT}=-0.0829$, $R^2=0.9991$; and $c_{TT}=0.405$, $R^2=0.99997$. By superposition, with combined loads the output will be:

$$\begin{bmatrix} N_{volts} \\ T_{volts} \end{bmatrix} = \mathbf{C} \begin{bmatrix} N_{load} \\ T_{load} \end{bmatrix} \text{, where } \mathbf{C} = \begin{bmatrix} c_{NN} & c_{NT} \\ c_{TN} & c_{TT} \end{bmatrix} \tag{A.5}$$

The force measurements are then obtained from:

$$\begin{bmatrix} N_{load} \\ T_{load} \end{bmatrix} = \mathbf{C}^{-1} \begin{bmatrix} N_{volts} \\ T_{volts} \end{bmatrix} \tag{A.6}$$

where the normal force measurement $F(t) = N_{load}$, and in N/V:

$$\mathbf{C}^{-1} = \begin{bmatrix} 2.509 & 0.514 \\ 0.027 & 2.477 \end{bmatrix}.$$

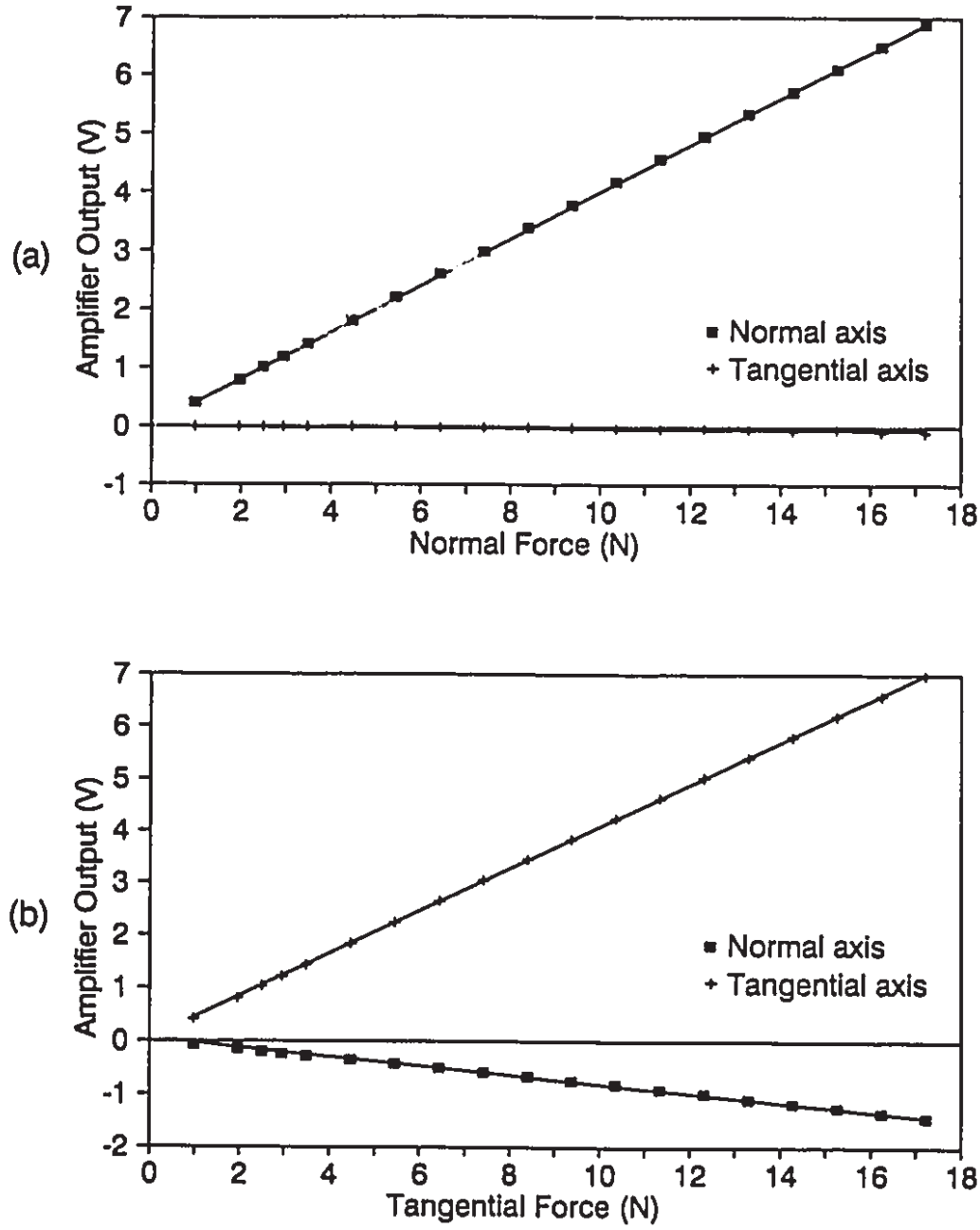

Figure A.1 Calibration data and calibration lines for the force sensor. (a) Normal direction. (b) Tangential direction.

APPENDIX B

VISION SENSOR CALIBRATION

The vision sensor measures the position of the tool relative to the part edge. During deburring this position corresponds to the chamfer depth. The sensor was calibrated by moving the tool with the AEE, and measuring the part corner location with the sensor. Based on dial gauge measurements the AEE's accuracy is as least as good as 10 μm (the accuracy of the dial gauge) [11]. Assuming that any errors caused by the AEE are random they will have no effect on the calibration except to cause the sensor's accuracy to be underestimated. This calibration method has the advantage that it doesn't require hardware outside of the AEE and the sensor, and can therefore be easily repeated for verification.

To obtain the origin for the tool position the AEE was commanded to move slowly towards the edge of a burr free part with the tool rotating. The instant contact was sensed (by electrical continuity between the tool and part) the motion was stopped and the origin was set. The tool was then backed away 1 mm from the edge in 0.05 mm increments. At each increment 100 measurements of the part corner location were obtained. The tool was moved back from the edge, rather than forward, to allow the part to be reused. Assuming the sensor is linear, the calibration results will be equally valid for positive tool motions. The data was then fit using least squares to the linear relation:

$$x_t = c_1 \bar{p}_{12} + c_2 \tag{B.1}$$

where x_t is the commanded tool position in mm, $\bar{p}_{12}$ is the mean part corner location in pixels, and $c_{1,2}$ are calibration constants. The calibration data and calibration line are shown in Figure B.1. The calibration constants are: c_1=0.0317 mm/pixel, and c_2=-6.98 mm. These constants are used with equation 5.10 to obtain the depth measurement. The R^2 value was 0.9994. Clearly, based on this value the sensor is very linear.

The calibration data and constants can be used to estimate the accuracy of the sensor. The accuracy of a measurement is equal to the sum of the signed values of the difference between the mean of the measurements and the actual value, and the dispersion, which gives the largest absolute sum [69]. With a dispersion of 3σ the measurements should fall within the accuracy band 99.7% of the time. Here the actual value is taken to be x_t and the output of equation B.1, with the data as input, is the measurement. This produced a set of accuracy values, one for each value of x_t. The accuracy for the sensor will be taken as the largest value, which was $\pm(11.8+3\cdot 0.4) = \pm 13\ \mu$m.

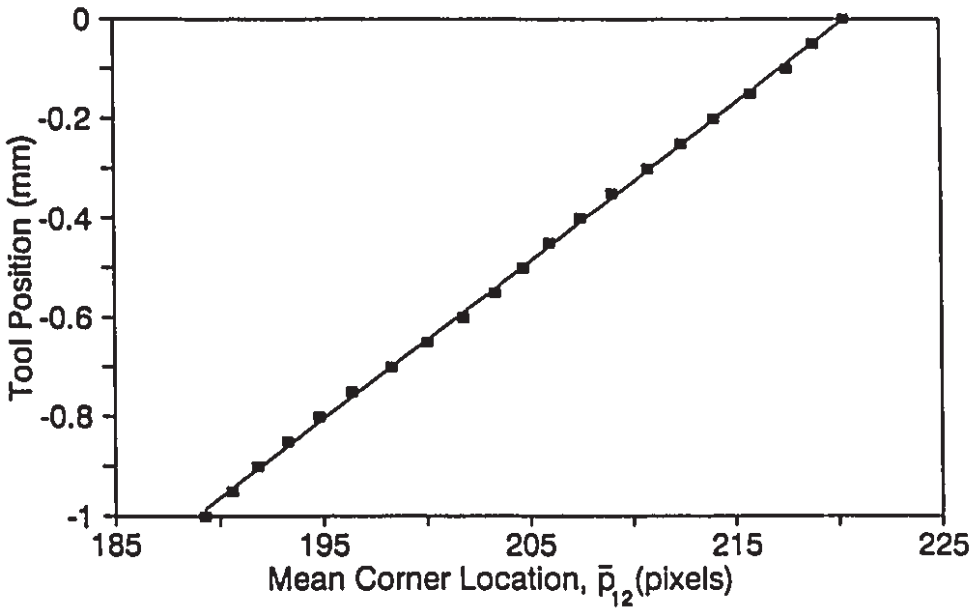

Figure B.1 Calibration data and calibration line for the vision sensor.

APPENDIX C

INSPECTION SYSTEM CALIBRATION

The inspection system measures the chamfer depth, top angle, and side angle. These dimensions are shown in Figure C.1 as c, β_t, and β_s respectively. The system was calibrated using a set of test pieces with depths of 0.2-0.8 mm, and angles from 40-50°, machined on a milling machine. For each sample the distances a and b were measured using a Nikon Measurescope microscope (accurate to 1 μm). For all of the test pieces $\beta = 90°$, so that:

$$\beta_t = tan^{-1}(b/a) \tag{C.1}$$

$$\beta_s = 90° - \beta_t \quad \text{and} \tag{C.2}$$

$$c = a \cdot sin\beta_t \tag{C.3}$$

One hundred inspection measurements were then taken for each part. The line segment slopes and intersection points were solved for as described in Chapter 5, sections 5.24 and 5.4. These results were then fit to the linear relations:

$$c = c_3\bar{d}_p + c_4 \tag{C.4}$$

$$\beta_t = c_5\bar{\theta}_1 + c_6 \tag{C.5}$$

$$\beta_s = c_7\bar{\theta}_2 + c_8 \tag{C.6}$$

where $d_p = sin(tan^{-1}(m_1) - tan^{-1}(m_2))[(l_{13}-l_{12})^2 + (p_{13}-p_{12})^2]^{1/2}$ is the depth in pixels, $\theta_1 = tan^{-1}(m_1) - tan^{-1}(m_2)$ is the sensed top angle, and $\theta_2 = tan^{-1}(m_2) - tan^{-1}(m_3)$ is the sensed side angle. The calibration results are shown in Figure C.2. The constants and

their associated R^2 are: $c_3 = 0.0319$ mm/pixel, $c_4 = -0.002$ mm, and $R^2 = 0.993$; $c_5 = 22.0$, $c_6 = 18.4°$, and $R^2 = 0.978$; $c_7 = 20.7$, $c_8 = 22.3°$, and $R^2 = 0.977$. These constants are used with equations 5.12-5.14 to obtain the depth and angle measurements.

The system's accuracy was estimated from the calibration data in the same manner as in Appendix B. For the depth the accuracy is $\pm(19.9 + 3 \cdot 1.2) = \pm 24\ \mu m$, for the top angle it is $\pm(1.2 + 3 \cdot 0.2) = \pm 1.8°$, and for the side angle it is $\pm(1.8 + 3 \cdot 0.2) = \pm 2.4°$.

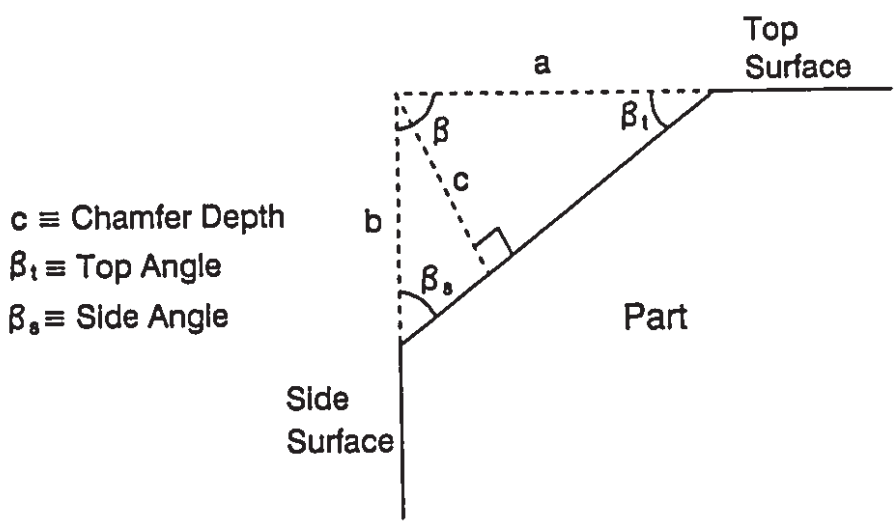

Figure C.1 Sectional view of a chamfered edge, showing definitions of depth, and angles.

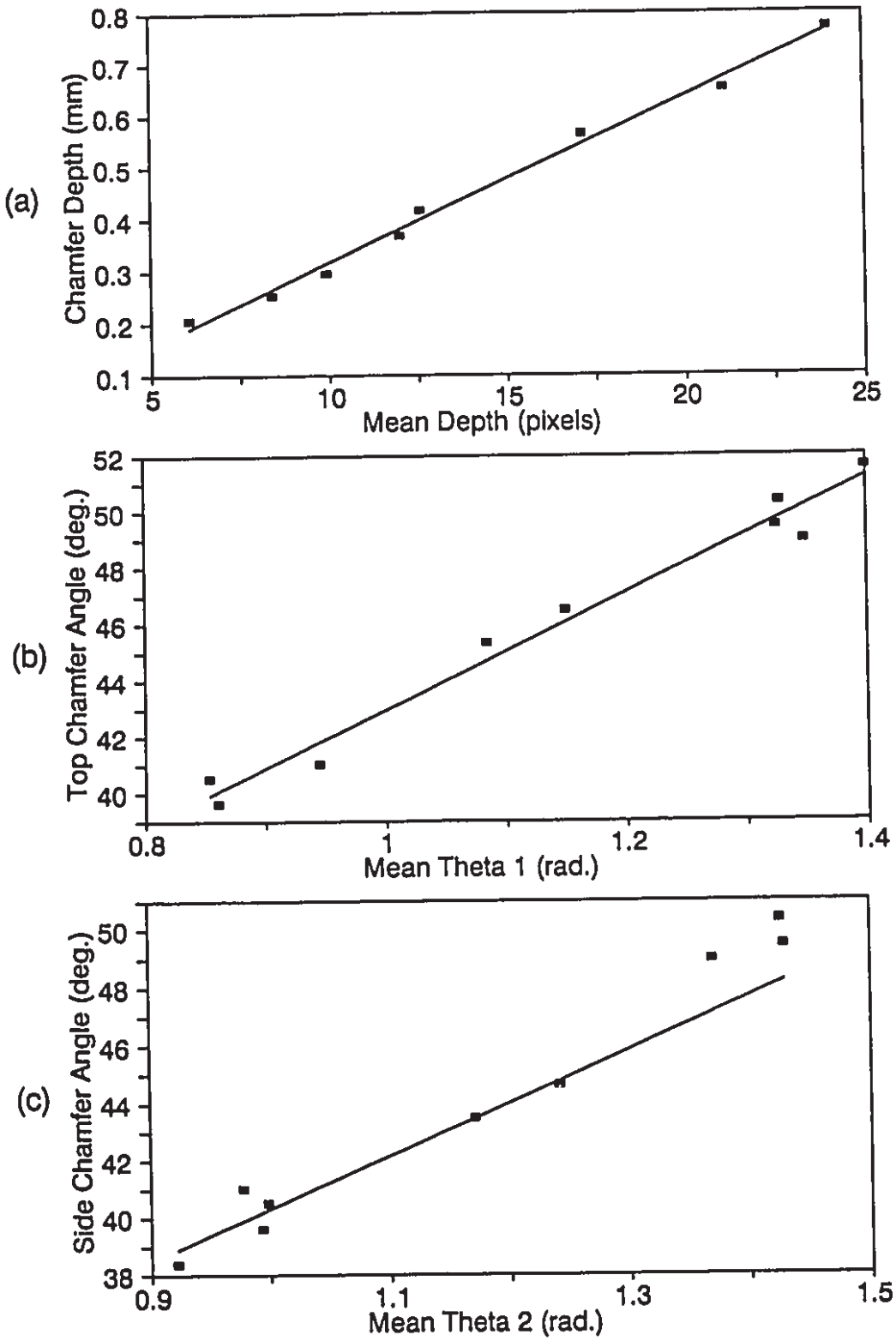

Figure C.2 Calibration data and lines for the inspection system. (a) Depth. (b) Top Angle. (c) Side Angle.

APPENDIX D

DERIVATION OF GPCL IN TRANSFER FUNCTION FORM

This derivation is an extension for GPCL of McIntosh *et al.*'s [65] derivation of GPC in transfer form. Here the arguments q^{-1} and t will be omitted for clarity. The derivation begins with a modified version of the CARIMA model:

$$A\Delta y = q^{-1}B\Delta u + T\xi \tag{D.1}$$

T is used as a design polynomial to improve robustness by low-pass filtering the future predictions. To obtain the j-step ahead prediction, $\hat{y}(t+j\,|\,t)$, from equation D.1 consider the identity:

$$T = E_jA\Delta + q^{-j}F_j \tag{D.2}$$

Multiplying (D.1) by E_jq^j gives:

$$E_jA\Delta y(t+j) = E_jB\Delta u(t+j-1) + E_jT\xi(t+j) \tag{D.3}$$

Now substituting $E_jA\Delta$ from (D.2) gives:

$$\hat{y}(t+j\,|\,t) = G_j'\Delta u^f(t+j-1) + F_jy^f + E_j\tilde{\xi}(t+j) \tag{D.4}$$

where $G_j'=E_jB$, and "f" denotes a quantity filtered by $1/T$. Because Δu and not Δu^f is used in the cost function, (D.4) must be modified. The identity:

$$G_j' = GT + q^{-j}\tilde{G} \tag{D.5}$$

is substituted into (D.4) to give:

$$\hat{y}(t+j\,|\,t) = G\Delta u(t+j-1) + \tilde{G}_j\Delta u^f(t-1) + F_jy^f + E_j\tilde{\xi}(t+j) \tag{D.6}$$

This can be rewritten as:

$$\hat{y}(t+j\,|\,t) = G\Delta u(t+j-1) + f \tag{D.7}$$

where $f = \tilde{G}_j \Delta u^f(t-1) + F_j y^f + E_j \hat{\xi}(t+j)$ is the free response prediction. However because $T=1$ in the original CARIMA model of the process (equation 6.11) this prediction incorrectly models the dynamics between y, u, and ξ. This is overcome by additionally filtering ξ by $1/T$ to give the correct free response prediction:

$$f = \tilde{G}_j \Delta u^f(t-1) + F_j y^f + E_j \tilde{\xi}^f(t+j) \tag{D.8}$$

Combining the outputs of (D.7) from $j = N1 \ldots N2$ gives the key vector form:

$$\hat{\mathbf{y}} = \mathbf{G}\tilde{\mathbf{u}} + \mathbf{f} \tag{D.9}$$

where $\hat{\mathbf{y}} = [\hat{y}(t+N1), \hat{y}(t+N1), \ldots \hat{y}(t+N1)]^T$, $\tilde{\mathbf{u}} = [\Delta u(t), \Delta u(t+1), \ldots, \Delta(t+NU-1)]^T$, $\mathbf{f} = [f(t+N1), f(t+N1+1), \ldots, f(t+N2)]^T$, and $\mathbf{G}$ is a matrix of dimension (N2−N1+1) × NU. Minimization of GPC's cost function results in the projected control-increment vector:

$$\tilde{\mathbf{u}} = (\mathbf{G}^T\mathbf{G} + \lambda\mathbf{I})^{-1}\mathbf{G}^T(\mathbf{w} - \mathbf{f}) \tag{D.10}$$

The current control-increment is then:

$$\Delta u(t) = \bar{\mathbf{g}}^T(\mathbf{w} - \mathbf{f}) \tag{D.11}$$

where $\bar{\mathbf{g}}^T = [\bar{g}_{N1}, \ldots, \bar{g}_{N2}]$ is the first row of $(\mathbf{G}^T\mathbf{G} + \lambda\mathbf{I})^{-1}\mathbf{G}^T$, and $\mathbf{w}$ is the vector of future setpoints. Because the concern here is regulation rather than servoing, a constant setpoint of w is assumed. Substituting f values from equation D.8 into D.10 gives:

$$\Delta u(t) = -\sum_{j=N1}^{N2} \bar{g}_j [\tilde{G}_j \Delta u^f(t-1) + F_j y^f + E_j \tilde{\xi}^f(t+j)] \tag{D.12}$$

Simplifying and rewriting gives:

$$Tw = R\Delta u + Sy + H\hat{\xi} \tag{D.13}$$

where:

$$R = \left(T + q^{-1} \sum_{j=N1}^{N2} \bar{g}_j \bar{G}_j \right) \Big/ \sum_{j=N1}^{N2} \bar{g}_j \tag{D.14}$$

$$S = \left(\sum_{j=N1}^{N2} \bar{g}_j F_j \right) \Big/ \sum_{j=N1}^{N2} \bar{g}_j \tag{D.15}$$

$$H = \left(\sum_{j=N1}^{N2} \bar{g}_j q^j E_j \right) \Big/ \sum_{j=N1}^{N2} \bar{g}_j \tag{D.16}$$